2021

Modeling and Numerical Simulations Of The Michigan Tech Convection Cloud Chamber

Subin Thomas
Michigan Technological University, subint@mtu.edu

MODELING AND NUMERICAL SIMULATIONS OF THE MICHIGAN TECH CONVECTION CLOUD CHAMBER

By

Subin Thomas

A DISSERTATION

Submitted in partial fulfillment of the requirements for the degree of

DOCTOR OF PHILOSOPHY

In Atmospheric Science

MICHIGAN TECHNOLOGICAL UNIVERSITY

2021

This dissertation has been approved in partial fulfillment of the requirements for the Degree of DOCTOR OF PHILOSOPHY in Atmospheric Science.

Department of Physics

Dissertation Advisor:	*Dr. Raymond A. Shaw*
Committee Member:	*Dr. Will H Cantrell*
Committee Member:	*Dr. Claudio Mazzoleni*
Committee Member:	*Dr. Mikhail Ovchinnikov*
Department Chair:	*Dr. Ravindra Pandey*

Contents

List of Figures

List of Tables

Preface

Popular Jewish folklore about the fifteenth century Rabbi Loew is of the *Golem of Prague*. The Rabbi created *Golem* out of clay, like modern computers with Silicon, at its core and gave life to it by writing *emet* (meaning Truth) on the forehead of the clay being. To the amazement of the Rabbi, the *Golem* was extremely powerful but could only distinguish between *Truth* and *False* statements like the modern-day computers. According to folklore, the apathetic creature turned malevolent due to the ambiguity in its orders.

This dissertation is about a few *Golems* (read Models) to explore atmospheric processes in the context of the cloud chamber. The Michigan Tech cloud chamber is a unique experimental facility to produce and sustain clouds for extended periods. This facility can study the behavior of cloud particles in a moist turbulent environment. The scaling and modification of System for Atmospheric Modeling (SAM) to simulate the cloud chamber, discussed in Chapter 3, occurred first chronologically. With an experimentally validated model, we looked into the processes in the cloud chamber, which yielded two significant results discussed in Chapter 4 and Chapter 5.

We created a second *Golem* to answer the question, Can we predict the behavior of the cloud system in the cloud chamber if we knew the boundary conditions? The

isolation provided by COVID 19 during the Summer of 2020 provided an excellent opportunity to answer this question. A simple mean-field model for the cloud chamber was developed jointly with my advisor Dr. Raymond Shaw. The analytical model and a coupled ODE solver provided a perfect sandbox to play with and understand the effect of various parameters of the cloud system. Currently, the model accounts only for the condensation effects but can be non-trivially expanded to include collision coalescence effects.

In the final chapter, we acknowledge the limitations and envision the future directions to create new and better *Golems*.

Abstract

Understanding atmospheric clouds is essential for human progress, ranging from short-term effects such as when and how much it rains to long-term effects such as how much temperatures would rise due to global climate change. Clouds vary globally and seasonally; also they have length scales ranging from a few nanometers to a few kilometers and timescales from a few nanoseconds to a few weeks. Knowledge gaps in aerosol-cloud-turbulence interactions and a lack of sufficient resolution in observations pose a challenge in understanding cloud systems. Experimental facilities like the Michigan Tech Cloud Chamber can provide a suitable platform for studying aerosol-cloud interactions in the presence of turbulence without any feedback processes, within a steady state environment. In the current thesis, we modify an atmospheric model to simulate the Michigan Tech Cloud Chamber and validate against the turbulence measured from the experiments. The modified atmospheric model is used to gain insights into the cloud chamber processes, and to predict and interpret the experimental results. This model is used to validate theoretical results, such as the presence of a constant microphysics independent heat flux. Further, the model results helps us to identify the non-Gaussian nature of supersaturation during isobaric mixing processes. Finally, this model serves as the first-order approximation for insights into the physics governing the cloud-turbulence interactions for a larger cloud chamber.

Chapter 1

Introduction

"A journey of a thousand miles begins with a single step"

- Lao Tzu

The story of human civilization is intertwined with the story of water[4, 5]. Civilizations have risen and fallen owing to changes in rain patterns[6, 7]. Droughts and floods have been sources of disputes between nation - states, internal conflicts, human migration, affecting both the economy and internal stability of the nations[8, 9, 10, 11]. Attempts to avert such crises by pleasing the rain gods across human history have panned from dances[12], songs[13] to cloud seeding[14]. Hence understanding when, where, and how much it would rain requires an understanding of the cloud systems and why it rains.

Clouds and the associated microphysical phenomena range from a few nanometers to a few tens of kilometers and spatially from a few microseconds to a few weeks[15, 16]. The number, type, origin, and history of the nanoscale aerosol affect the macroscopic cloud properties[17, 18]. Therefore, clouds form a complex system with multiple interacting scales. Hence the studies of atmospheric clouds without proper characterization of both small-scale and large-scale processes leaves significant gaps in the understanding of weather[16, 19]. The field campaigns, ground observations, satellite observations, and numerical simulations constitute independent efforts to observe, analyze and synergistically improve the understanding of the weather system[20].

Decoupling the individual processes - in the context of this thesis, the cloud microphysical processes - poses significant challenges because of the complexities mentioned above. Thus laboratory experiments prove to be of importance in decoupling the feedbacks and identifying the primary interactions. These experiments can serve as a testbed to evaluate the reliability and fidelity of the numerical simulations. The current thesis describes a rigorous attempt to understand the physical phenomena occurring in an experimental setup using numerical simulations.

1.1 Michigan Tech Cloud Chamber

The Michigan Tech cloud chamber is a modern–day experimental setup to study turbulence - aerosol - cloud interactions in a controlled environment[21]. The fluid flow in the chamber is initialized and sustained by an unstable temperature gradient between the cold top and warm bottom surface. The supersaturation is thus produced by mixing process as discussed in Chapter 3. To the turbulent supersaturated environment, the aerosols are injected to form cloud particles.

The experimental studies in the Pi cloud chamber were instrumental in identifying the role of turbulence in the activation of aerosols [22], associated activation regimes [23], growth of activated droplets in warm cloud conditions[24], cloud collapse[25] and glaciation in mixed phase clouds[26]. Further, it has provided valuable insights into the effect of cloud processing of aerosols[18], effect of variability of cloud droplet number[27], secondary ice particle production [28], cloud optical processes[29] and light scattering due to spatial correlations [30, 31].

The studies mentioned above represent the first–order experiments possible with the cloud chamber. In order to conduct higher–order experiments using the cloud chamber, we need to develop a deeper understanding of the processes in the chamber. A deeper understanding would require a three-dimensional picture of the processes

in the cloud chamber. The numerical simulations can provide a more refined description of the cloud chamber without any intrusive measurements. A finely tuned numerical simulation can provide details of the local processes leading to large–scale self-organization. Further, a model can provide insights, predictions, and directions and narrow the parameter space for experiments.

In this thesis, Chapter 2 discusses the understanding of the fundamental physical processes in the cloud chamber. Modification of an atmospheric model to simulate the fluid dynamics and microphysics inside the cloud chamber and validation with experiments are illustrated in Chapter 3. The non–dimensional numbers relevant for the RBC processes and microphysics of the cloud droplets formed in the cloud chamber are identified, and existence of a constant flux is demonstrated in Chapter 4. In Chapter 5, we demonstrate the non–Gaussian nature of supersaturation as a result of mixing processes. The preliminary results based on the dynamics and microphysics comparing the current chamber to a hypothetical chamber of larger size is presented in Chapter 6. Finally, the thesis concludes in Chapter 7 by acknowledging the limitations of the model and envisioning the path forward.

Chapter 2

Cloud Chamber Processes

"Standing on the shoulders of giants."

- Issac Newton

The Michigan Tech cloud chamber is an experimental setup sitting at the juncture of two well developed branches of physics - Rayleigh–Bénard Convection and Cloud Microphysics, with long histories and their own unique challenges. The cumulative research spanning a few centuries in each of the fields has produced massive literature from experiments, observations and simulations. Hence we use the widely accepted results from each of these fields to generate a first picture of the cloud chamber.

2.1 Dynamics : Rayleigh–Bénard Convection (RBC)

Rayleigh-Bénard system is an extensively studied fluid dynamics problem, with a rich history and exciting developments[32, 33]. We can gain a first understanding of the flow dynamics and thermodynamics from the well-known results in Rayleigh-Bénard convection systems. A dry Rayleigh-Bénard convection system consists of a warm bottom surface (at T_b) and a cold top surface (at T_t), with convection ensuing due to the unstable density gradient along the direction of gravity. In the Pi Chamber, we have both top and bottom surface wetted, and hence at steady-state conditions, these surfaces remain saturated. For Rayleigh–Bénard Convection (RBC) in a box identical to the MTU Pi Chamber, the characteristic length scale is the height of the chamber (H).

For a dry RBC system with temperature difference of ΔT between top and bottom is characterized by four non–dimensional numbers :

1. Aspect Ratio ($\Gamma = L/H$)
2. Prandtl Number ($Pr = \nu/\nu_T$)
3. Rayleigh Number ($Ra = g\beta\Delta T H^3/\nu\nu_T$)

4. Nusselt Number (Nu)

Here ν is the momentum diffusivity, ν_T is the thermal diffusivity, g is the acceleration due to gravity and β is the thermal expansion coefficient. The aspect ratio is the non–dimensionalized horizontal length scale,L. Prandtl number compares the dissipation of the momentum to that of thermal energy. Rayleigh number quantifies the competition of the motion ($\sqrt{gH\beta\Delta T}$) of fluid parcel due to buoyancy against drag and diffusion. Finally, Nusselt number is a measure of the efficiency of heat transfer by convection compared to the conductive heat transfer.

2.1.1 Convection Velocity

For a dry Rayleigh–Bénard convection system, the air-parcel free fall velocity scale is accepted as the characteristic velocity scale [33]. This free fall velocity scale is given by

$$\begin{aligned} w &= \sqrt{g\,H\,\beta\Delta T} \\ w &\propto \sqrt{H\,\Delta T}. \end{aligned} \tag{2.1}$$

Another candidate for a characteristic velocity is the convective velocity scale introduced by Deardorff [34] given by

$$w^* = \left(\frac{g}{T} z_i \overline{wT_0}\right)^{1/3}. \tag{2.2}$$

For the scenario of RBC, $z_i = H$ and $\overline{wT_0}$ is the kinematic heat flux near the surface. It should be noted that $\overline{wT_0}$ is independent of H, therefore the convective velocity scale has H dependence as,

$$w^* \propto H^{1/3}. \tag{2.3}$$

2.1.2 Time Scales

The characteristic timescale depends on the choice of velocity scale. For free fall velocity scale,

$$t \propto H^{1/2} \Delta T^{-1/2}. \tag{2.4}$$

For the Deardorff/convective velocity scale,

$$t \propto H^{2/3}. \tag{2.5}$$

Unlike the Deardorff velocity scale depending on the heat flux, free–fall velocity scale depends on the imposed boundary conditions and the height of the chamber.

2.1.3 Mean Temperature and Water Vapor

In the *bulk* (volume far away from the boundaries) of the chamber, the mean temperature and mean water vapor mixing ratio are given by

$$\bar{T} \;=\; \frac{\rho_b\, T_b + \rho_t\, T_t}{\rho_b + \rho_t}. \tag{2.6}$$

Similarly,

$$\bar{Q} \;=\; \frac{\rho_b\, Q_{sat}(T_b) + \rho_t\, Q_{sat}(T_t)}{\rho_b + \rho_t}. \tag{2.7}$$

Here ρ_t is the density of the fluid at the top of the chamber and ρ_b is the density of the fluid at the bottom of the chamber. In equations 2.6 and 2.7, we ignore the effects of the sidewalls. The effect of sidewalls is discussed in detail in Chapter 3. Thus the mean for any passive scalar can be written as,

$$\bar{\Psi} \;=\; \frac{\rho_b\, \Psi_b + \rho_t\, \Psi_t}{\rho_b + \rho_t}. \tag{2.8}$$

2.1.4 Temperature and Water Vapor Fluctuation

According to the experimental observations by Niemela et al.[35] temperature fluctuations for a single phase Rayleigh-Bénard convection system is given by

$$\frac{T'}{\Delta T} \propto Ra^{-1/7}. \tag{2.9}$$

Thus temperature fluctuations would scale as,

$$T' \propto H^{-3/7} \times \Delta T. \tag{2.10}$$

The temperature and water-vapor mixing ratio transport differ only by differential diffusivity, and these effects are significant compared to the advection transport only close to the boundary. Hence, in bulk, we assume a similar behavior for the water vapor mixing ratio.

$$\frac{Q_v'}{\Delta Q_v} \propto Ra^{-1/7}. \tag{2.11}$$

Identical to Eq. 2.10, we have

$$Q_v' \propto H^{-3/7} \times \Delta Q_v. \tag{2.12}$$

In Niemela et al.[35], the proportionality constant which fits the experimental data is 0.37. The proportionality constant for temperature and water vapor mixing ratio might be different.

An implication of Eq.s 2.10 and 2.12 is that as the height of the chamber increases, both temperature and water vapor fluctuations decrease. Similarly, as the temperature difference and water vapor difference between the top and bottom surface decrease, the corresponding fluctuations decrease. For identical gradients the fluctuations scale as $H^{4/7}$. For Rayleigh-Bénard systems, it has been shown by Niemela et al. [33, 35], that the scalar fluctuations are Gaussian in nature, therefore the the temperature variance is of the form

$$\overline{T'^2} \propto H^{-6/7} \times \Delta T^2 \tag{2.13}$$

and consequent water vapor variance is given by,

$$\overline{Q_v'^2} \propto H^{-6/7} \times \Delta Q_v^2. \tag{2.14}$$

Kulmala [36] derived an expression for supersaturation variance given by

$$\overline{S'^2} \propto \overline{S}^2 \left(\frac{\overline{Q_v'^2}}{\overline{Q_v}^2} - \frac{2L_w}{R_v \overline{T}} \frac{\overline{Q_v' T'}}{\overline{Q_v}\,\overline{T}} + \left(\frac{L}{R_v \overline{T}} \right)^2 \frac{\overline{T'^2}}{\overline{T}^2} \right). \tag{2.15}$$

Assuming the co-variance of water vapor and temperature, $\overline{Q_v' T'}$, scales identical to the variance of temperature. From Eq. 2.13 and 2.14, the supersaturation fluctuation variance can be shown to have a height dependence as

$$\overline{S'^2} \propto H^{-6/7}. \tag{2.16}$$

Therefore as the height increases, for the same temperature and water vapor difference, the supersaturation fluctuations decrease with height.

2.1.5 Rayleigh Number

Rayleigh number scales with H and ΔT as [33]

$$\begin{aligned} Ra &= \frac{g\,\beta\,H^3\,\Delta T}{\nu\,\alpha} \\ Ra &\propto H^3 \Delta T. \end{aligned} \tag{2.17}$$

2.1.6 Nusselt Number

Nusselt number is the ratio of the heat transferred non–dimensionalized by the heat transfer in the absence of any flow. For a moist convection system, the Nusselt number

is given by

$$\mathrm{Nu}_{\mu} = \frac{\overline{w'T'} + \frac{L}{C_p}\overline{w'Q_v'} - \alpha\nabla_z\overline{T} - \frac{L}{C_p}\nu_v\nabla_z\overline{Q_v}}{\alpha\frac{\Delta T}{H} + \nu_v\frac{L}{C_p}\frac{\Delta Q_v}{H}}. \tag{2.18}$$

In a dry convective system for Rayleigh number ranges of our interest, it has been experimentally and numerically demonstrated that [35, 37]

$$\begin{aligned} Nu &\propto Ra^{1/3}\text{ ,therefore} \\ Nu &\propto H\Delta T^{1/3}. \end{aligned} \tag{2.19}$$

From Eq. 2.19, it can be demonstrated that the heat flux is independent of the height of the chamber, but dictated by the temperature and water vapor boundary conditions at the top and bottom boundary conditions. The derivation of Eq. 2.18 and the physical implications are discussed in detail in Chapter 4.

2.2 Microphysics

The cloud microphysics problem of finding the number of cloud droplets and their mean droplet sizes can be studied in idealized conditions, of a constant mean supersaturation. We can establish the following steady-state microphysics balances for the cloud chamber :

1. Assuming all the injected aerosols are activated, in every time step the number

of droplets activated should be equal to the number of droplets removed via precipitation.

2. The mass of total water vapor condensed should be equal to the total liquid water mass removed via precipitation.

Assuming the cloud droplets settle via Stokes' settling velocity, these balances would establish the number concentration of the cloud droplets, n and the mean radius $\overline{r}$. The equations are

$$\frac{\partial n}{\partial t} = \dot{n}_{in} - \frac{n}{\tau_{res}} \tag{2.20}$$

$$\frac{\partial q_l}{\partial t} = \dot{q}_l - \frac{q_l}{\tau_{res}}. \tag{2.21}$$

Here, n is the number of cloud droplets, $\dot{n}_{in}$ is the injected cloud droplets, $\tau_{res} = H/V_t$ is the droplet residence time, $V_t = k_1\overline{r}^2$ is the terminal velocity, k_1 is the Stokes' velocity constant and q_l is the liquid water mixing ratio. Finally

$$\dot{q}_l = n\,\rho_l\,2\,\pi r dr^2/dt$$

and the droplet growth equation[38] is

$$dr^2/dt = 2\,G\,s.$$

Here r is any droplet radius, and G is the parameter accounting for diffusion of water vapor and the effect of latent heat due to condensation. To determine the in-cloud supersaturation s,

$$\frac{ds}{dt} = \frac{s_0 - s}{\tau_t} - \frac{s}{\tau_c}.$$

Here s_0 is the steady state supersaturation produced by mixing processes in the absence of the cloud droplet, τ_t is the supersaturation replenishment time-scale, $\tau_c (= (4\pi n r D')^{-1})$ is the phase relaxation time-scale and D' is the modified diffusivity for droplet growth[39].

For steady state, the number concentration of cloud droplets is

$$n = \dot{n}_{in} \frac{H}{k_1 \, r^2}. \tag{2.22}$$

and radius r is the positive real solution of the quartic equation given by,

$$r^4 + \left(\frac{4\pi D' H \dot{n}_{in} \tau_t}{k_1} \right) r^3 - \frac{3GHs_0}{k_1} = 0. \tag{2.23}$$

In this approach, the steady state mean supersaturation is

$$s = s_0 \left(1 + 4\pi \, n \, D' \, r \tau_t\right)^{-1}. \tag{2.24}$$

Figure 2.1, illustrates the solutions of equations 2.22,2.23 and 2.24 for a convection chamber of $H = 1$m, operating at a mean temperature before condensation of $T = 284.16$K and $\Delta T = 20$K. In panel 3, the maximum mean radius achieved by droplets plateaus when the cloud droplet lifetime is bounded by height of the chamber and the Stokes' settling velocity. We also notice the supersaturation also following an analogous behavior in the panel 1 of the figure. However as the number of activated cloud droplets increases, both supersaturation and the mean cloud droplet radius starts decreasing. Finally, we notice as the number of activated droplets increase, the liquid water content increases monotonically.

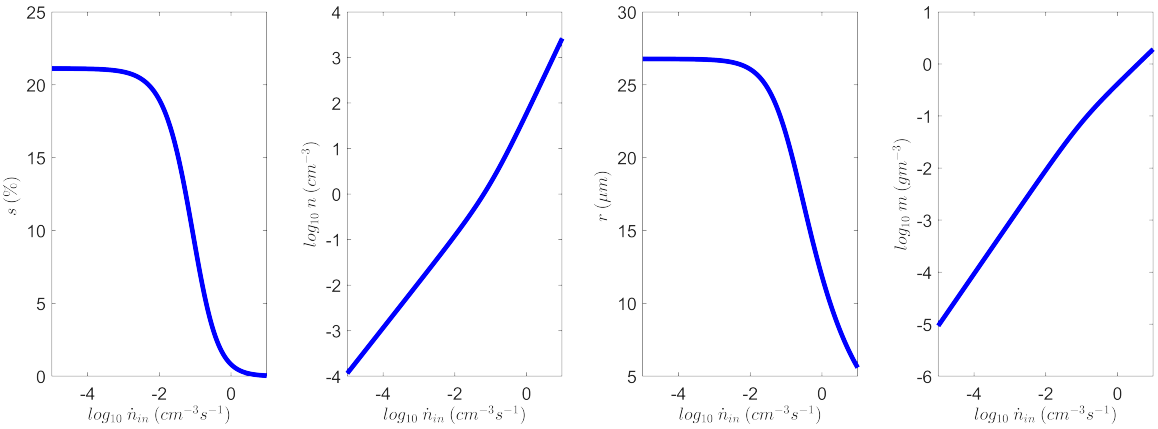

Figure 2.1: The steady state supersaturation, cloud droplet number concentration, mean droplet radius and liquid water content are plotted against aerosol injection rate $\dot{n}_{in}$. The parameters $\tau_t = 10$ s and $s_0 = 21.32\%$ are held constant. As the injection rate is increased, the cloud droplet number concentration increases, consequently, mean supersaturation and mean radius of cloud droplets decrease.

The same solution can be achieved by simultaneously solving,

$$\frac{\partial T}{\partial t} = \frac{T_0 - T}{\tau_t} + \frac{L}{c_p}\dot{q}_l \tag{2.25}$$

$$\frac{\partial q_v}{\partial t} = \frac{q_{v0} - q_v}{\tau_t} - \dot{q}_l. \tag{2.26}$$

$$\tag{2.27}$$

in addition to Eq. 2.20 and 2.21. Here T_0 and q_{v0} are the mean temperature and water vapor before droplets are injected. The latter method can be used to predict transient problems.

Figure 2.2 shows time series of supersaturation, liquid water content, droplet number concentration and droplet mean diameter. The system is initialized at the steady conditions that exist in the chamber when no aerosol particles are present, i.e., supersaturation of approximately 20%, corresponding to a mean temperature of 284.16K and $\Delta T = 20K$. Aerosol injection starts at $t = 0$ and the system is observed to reach steady state within approximately 10 s, and the observed values of s, q_l, n and d match to the values given by the analytical steady state model (shown as red dashed lines). At $t = 60$ s the aerosol injection is switched off and the liquid water content and droplet number concentration drop off, the supersaturation relaxes back to the no-cloud steady state, and the diameter of remaining cloud droplets grows to to the maximum size predicted by the steady state analytical theory described above (green dotted line).

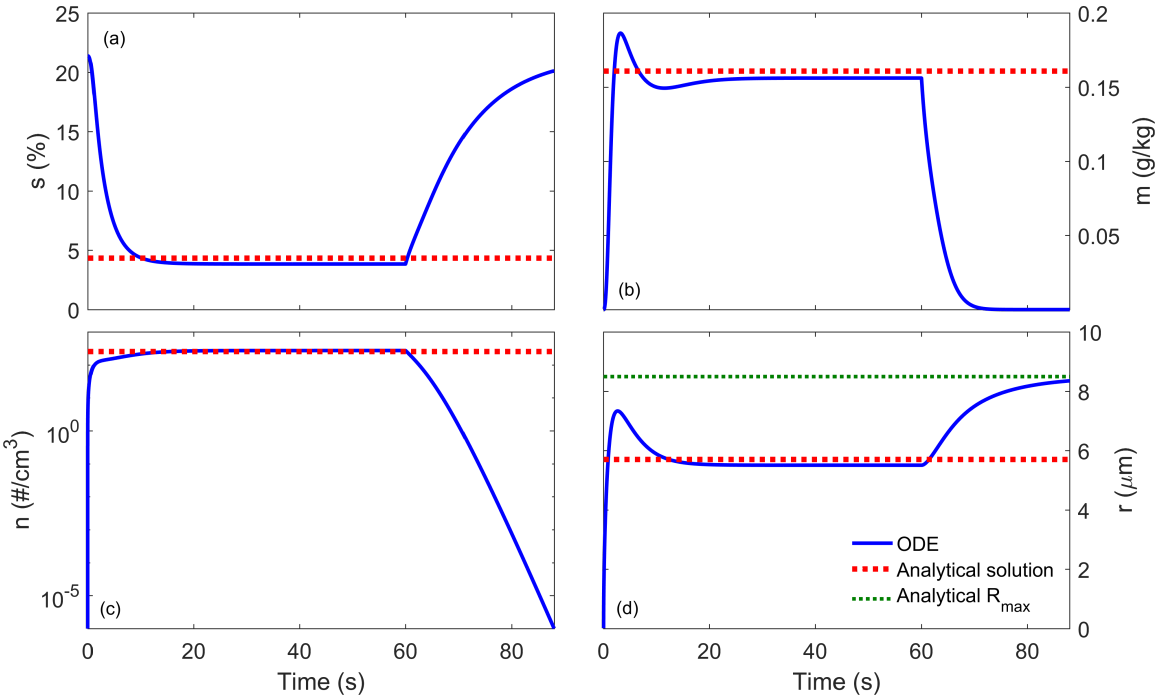

Figure 2.2: Comparison of the ODE solutions (blue) with analytical solution (red dashed line). a) Supersaturation , b) liquid water content, c) number concentration and d) radius are compared. The system is initialized at the steady-state conditions that exist in the chamber with no cloud droplets present and with aerosol injection starting at $t = 0$ s. At $t = 60$ s the injection is turned off and the cloud collapses. During the cloud collapse, the mean supersaturation increases and the droplet diameter increases consequently droplet removal flux increases. The maximum droplet size obtained analytically (green dotted line) is reached as the droplet concentration becomes very small.

2.3 Modeling of cloud chamber

Finally, in this section of the current chapter, we intend to examine the cloud chamber in the context of analytical models[40] and numerical models[2, 41, 42].

2.3.1 Analytical Models

The mechanisms leading to the steady-state cloud droplet size distribution experimental observations[43] in the cloud chamber are discussed in Chandrakar et al. [40]. Combinations of assumptions about the nature of supersaturation and the droplet life timescales are considered to be the necessary mechanisms. The different combinations discussed are

1. Constant mean supersaturation without turbulent fluctuations of supersaturation and Stokes' removal of droplets[44].

2. Zero mean supersaturation with turbulent fluctuations of supersaturation and Stokes' removal of droplets[29].

3. Zero mean supersaturation with turbulent fluctuations of supersaturation and constant droplet lifetime[2].

The authors also compare the observations against the droplet size distributions predicted by the maximum entropy principle[45]. Based on the hypothesis testing, the authors conclude that the model with *zero mean supersaturation with turbulent fluctuations of supersaturation and droplet removal by Stokes' settling* agrees the most with the experiments.

Assuming, *condensational droplet growth only due to constant mean supersaturation and droplet removal via Stokes' settling*, Krueger[44] derived an expression for the distribution of droplet lifetimes in the cloud chamber. The variation in the size of the droplets was a result of the different lifetimes of the droplet. This method can evaluate the in-cloud mean supersaturation in the experiments from the mean number concentration and the mean radius of the cloud droplet distribution. Thus, the model is an excellent diagnostic tool with limited predictive capability. The model also assumes the droplets to be well mixed in the chamber. However, the droplets tend to size-sort themselves in the larger sizes once they exceed the updraft velocities.

The models described above assumes droplet number concentration and droplet size distribution are driven by mean supersaturation. The mean and fluctuations of supersaturation are also affected by the cloud droplet number concentration and droplet sizes. The latter interaction are not accounted for in both Chandrakar et al. [40] and Krueger [44].

2.3.2 Numerical Models

The cloud chamber proved to be an excellent facility to test the reliability and fidelity of numerical simulations[46]. Hence, numerical modeling of the Pi Cloud Chamber is

included as one of the six workshop cases at the International Cloud Modeling Workshop (ICMW) 2020/2021 [41, 47]. Despite the wide attention, only three numerical studies based on the Pi cloud chamber have been published at the time of writing.

1. System for Atmospheric Modeling (SAM) with spectral bin microphysics [41].
2. Direct Numerical Simulations based on an idealized central region of the Pi Chamber [2].
3. Baby EULAG with bin and Lagrangian cloud microphysics [42].

The first attempt to model the cloud chamber in its entirety is discussed in Chapter 3 of the current thesis.

In the direct numerical simulation of the Pi chamber by Saito et al. [2], the central region of the cloud chamber was modeled, assuming it to be isotropic. The study intended to numerically simulate the experimental observations at the Pi cloud chamber[24]. The domain under consideration is 1.024 meters, with velocity and temperature fields forced independently. The droplets modeled as point particles are removed at a timescale of 580 seconds to match the Stokes' settling based interpretations of experimental observations from the cloud chamber. An analytical expression for the size distribution is derived, and the numerical solutions match Saito et al.. Chapter 3 demonstrates that the sidewall fluxes are significant and cannot be ignored. Secondly, the temperature and water vapor fluctuations need to be correlated

in RBC, and hence the supersaturation probability distribution need not be Gaussian. The importance of water vapor-temperature correlation on supersaturation PDF is discussed in great detail in Chapter 7.

The third study uses the cloud chamber[42] as a testbed to compare bin microphysics, and Lagrangian cloud microphysics. In that study, the droplet size distribution predicted by the bin and Lagrangian cloud model is similar. The author concludes that bin microphysics has less diffusion since the bins are finely spaced, and the absence of numerical diffusion is due to vertical advection. Though, Lagrangian model could have provided more information on activation and deactivation of aerosols, using Twomey activation negates any such advantages.

From the initial discussions of the Pi chamber case at ICMW [47] - it would be worth discussing some of the models under development. The two significant paths are Large Eddy Simulations (LES) combined with Lagrangian Cloud Models and Direct Numerical Simulations (DNS) with point particles. The models are

1. System for Atmospheric Modeling[48] with LCM [49].

2. CM1[50] with LCM [51].

3. DNS with point particles [52].

4. One dimensional turbulence with embedded microphysics.

In the DNS with point particles, the periodic boundary conditions are implemented at the lateral surfaces. The mean supersaturation is attained by adjusting the saturation ratio at the bottom surface instead of side walls as in [41]. As mentioned earlier, the sidewalls which have a more considerable influence are not modeled in the study.

Chapter 3

Scaling of an atmospheric model to simulate turbulence and cloud microphysics in the Pi Chamber

> "Thirty years ago, we used to ask: *Can a computer simulate all processes of logic?* The answer was *yes*, but the question was surely wrong. We should have asked: *Can logic simulate all sequences of cause and effect?* And the answer would have been *no*."
>
> - Gregory Bateson

This chapter is about the scaling of an atmospheric model to simulate the Michigan

Tech Pi Chamber. It is based on a collaborative research published in the Journal of Advances in Modeling of the Earth Systems[41][1].

Abstract

The Pi Cloud Chamber offers a unique opportunity to study aerosol–cloud microphysics interactions in a steady-state, turbulent environment. In this work, an atmospheric large eddy simulation (LES) model with spectral bin microphysics is scaled down to simulate these interactions, allowing comparison with experimental results. A simple scalar flux budget model is developed and used to explore the effect of sidewalls on the bulk mixing temperature, water vapor mixing ratio, and supersaturation. The scaled simulation and the simple scalar flux budget model produce comparable bulk mixing scalar values. The LES dynamics results are compared with particle image velocimetry measurements of turbulent kinetic energy, energy dissipation rates and large scale oscillation frequencies from the cloud chamber. These simulated results match quantitatively to experimental results. Finally, with the bin microphysics included the LES is able to simulate steady-state cloud conditions and broadening of the cloud droplet size distributions with decreasing droplet number concentration, as observed in the experiments. The results further suggest that collision-coalescence does not contribute significantly to this broadening. This study opens a path for

[1]An edited version of the paper is published by AGU

further detailed inter-comparison of laboratory and simulation results for model validation and exploration of specific physical processes.

3.1 Introduction

Large-eddy simulation (LES) has been used for studies of clouds since the 1970s and 80s [53, 54], with the sophistication of cloud microphysics representation progressing steadily [e.g., 55, 56, 57]. LES has since been used in studying a wide range of cloud problems: from aerosol indirect effects [58], to deep tropical convection [59], to Arctic mixed-phase clouds [60]. Validation has typically been accomplished through model intercomparisons [e.g., 60, 61] and carefully-designed field projects [e.g., 62, 63, 64]. For detailed cloud studies, aerosols and clouds represented through 'bin microphysics' [e.g., 65] are often considered the gold standard, but recently it has been recognized that numerical artifacts can become dominant [66]. This surprising result emphasizes yet again the critical importance of rigorous model evaluation against the best possible measurements [67].

The purpose of this paper is to explore the ability of a widely-used large-eddy simulation model with detailed (spectral bin) cloud microphysics, to capture the observed

behavior of convection and cloud properties in a laboratory convective-cloud chamber. The Pi Cloud Chamber [21] generates clouds through isobaric mixing in turbulent Rayleigh-Bénard convection. Because aerosol input and thermodynamic forcing are independently and externally controlled, Pi Cloud Chamber offers a unique opportunity to explore turbulence–microphysics interactions [24, 25, 27]. Besides the well-characterized boundary and input conditions, turbulence and microphysical properties can be sustained in a dynamic steady state, with aerosol injection and cloud droplet activation balanced by droplet growth and sedimentation. This facilitates comparison to the LES cloud model and provides an opportunity to evaluate its ability to simulate the observed dynamics and microphysical processes in the cloud chamber. The interaction is two-way, because the model can also be powerful in helping to interpret measurements and providing guidance for future experiments.

The idealized Rayleigh-Bénard theory does not include sidewalls; following convention in the fluid mechanics literature [33], however, we will continue to refer to turbulent convection in an enclosed chamber as Rayleigh-Bénard convection. The Pi cloud chamber, if constructed according to the typical confined Rayleigh Bénard model, would have unstable temperature gradient along the direction of gravity and adiabatic sidewalls. Construction of an insulated sidewall, that is adiabatic in nature for the scalars, temperature and water vapor, poses an insurmountable engineering challenge. Hence by having actively temperature controlled sidewalls, and maintaining the sidewalls at the mean temperature between top and bottom - the sidewalls are

approximately adiabatic for the temperature, assuming a well-mixed fluid. For the water vapor field, the well-mixed fluid value is greater than the saturated value at the wall temperature; therefore, the zero-flux condition for water vapor cannot be achieved. Hence, to model the cloud chamber using traditional DNS or LES, with periodic lateral boundaries, appropriate scalar fluxes have to be provided. An approach to the budgeting of scalar fluxes for the Pi chamber is provided in the Section 3.3.1.

The Pi Cloud Chamber, in its box configuration used in the studies of Chang et al., Chandrakar et al., and Desai et al., [21, 24, 27], has dimensions 2 m $\times$ 2 m $\times$ 1 m, and generates turbulence by maintaining an unstable temperature gradient along the direction of gravity. To generate supersaturation inside the cloud chamber, the cold top and hot bottom surfaces are maintained at water saturation. On reaching the turbulent steady state, aerosol particles are introduced into the chamber, and can act as cloud condensation nuclei (CCN) when exposed to sufficient supersaturation to form cloud droplets. A variety of instruments exist for measurement of temperature, water vapor mixing ratio, turbulence, aerosols, and cloud droplet size distributions [21, 27].

The cloud chamber conditions in a typical experiment are accessible to a variety of computational approaches. On the high-fidelity side is direct numerical simulation (DNS) of the turbulent convection, with Lagrangian treatment of cloud droplets [e.g., 68, 69]. While this approach is being explored by several groups, it results in large

computational overhead both in terms of machine resources and time. We take the more computationally efficient approach of LES for two reasons: 1) it is agile, in the sense that it allows us to explore a variety of experimental configurations with relative computational ease; 2) it is widely used in the cloud physics community, and therefore it is of value to make direct comparison to highly-constrained and well-characterized experiments. LES allows us to comprehensively explore the turbulence and microphysics throughout the volume of the cloud chamber, with relatively few assumptions or approximations imposed in obtaining boundary fluxes. In the cloud chamber, the Kolmogorov length scale is of the order of 1 mm and the droplet diameters are in the range $1 - 50$ μm. Here we explore the possibility of studying the cloud droplet condensation growth in a turbulent environment using LES with a spatial resolution of ≈ 3 cm, coupled with spectral bin microphysics.

The paper is organized as follows: In Sec. 3.2 we describe both the dynamics and microphysics of the LES model, including modifications to dynamics and boundary conditions made to emulate the cloud chamber. Section 3.3 presents the results of the study: first, we present a scalar flux budget model for calculating mean thermodynamic properties in the cloud chamber, and predicted supersaturations are explored for a range of chamber boundary conditions; second the supersaturations predicted by the flux budget model are compared to the simulated mean properties in the LES; third, LES turbulence and flow properties are compared to known properties of

Rayleigh-Bénard convection and to measurements made with particle image velocimetry; fourth, we explore the ability of LES and bin microphysics to capture various, previously-published observations from the cloud chamber. Finally, the paper concludes with a summary and suggestions for next steps.

3.2 Description of the large-eddy simulation and cloud microphysics model

For the LES model in this study, we use the System for Atmospheric Modeling [SAM] [70], which solves the equations of motion with the anelastic approximation and a 1.5 order closure based on turbulent kinetic energy for the subgrid-scales. These equations of motion are integrated using a third order Adams-Bashforth scheme, on a fully staggered Arakawa C-type grid with uniform horizontal and vertical grid sizes. The prognostic scalars are advected using a multidimensional positive definite advection transport algorithm [71]. Monin-Obukhov similarity theory is used to simulate surface fluxes. In standard atmospheric applications, SAM is configured to have periodic lateral boundaries and a rigid lid at the top of the domain, with Newtonian damping applied to all prognostic variables in the upper third of the model domain to reduce gravity wave reflection. For the Pi chamber, in addition to the bottom wall, which plays a role analogous to land surface, the top wall and lateral sides can also

impose momentum and scalar fluxes. Hence, in this study, the Monin-Obukhov similarity theory is also applied at these boundaries to compute appropriate fluxes. The magnitude of the momentum fluxes is adjusted to match observed dynamical conditions in the Pi-chamber by scaling a prescribed Monin-Obukhov roughness length parameter. The mean horizontal velocity close to the top and the bottom plates is zero, hence the application of constant flux Monin - Obukhov similarity theory would yield zero flux. Therefore, the Monin-Obukhov theory is applied to individual grid boxes. Fluxes from Monin - Obukhov similarity theory were compared to and found to match those from the temperature wall function model based on Rayleigh number scaling developed by Mcdermott et al. [72]. Furthermore, the turbulence properties thus obtained match the experimental measurements in Section 3.3.3. The top and bottom walls have saturated water-vapor conditions at their respective temperatures, and the sidewall boundary condition is chosen to mimic the condensation processes observed during the cloud chamber experiment (further details are given in Sections 3.3.1 and 3.3.2). Temperatures of the top, side, and bottom walls are all fixed.

Aerosol-cloud interactions in SAM are simulated by a spectral bin microphysics [SBM] model described in Khain et al.[73] and Fan et al.[74]. The SBM model involves aerosols and seven hydrometeors: water droplets, ice crystals (columnar, plate like and dendrites), snowflakes, graupel, and hail, with size distributions represented in 33 mass-doubling bins. The model accounts for relevant microphysical processes and interactions, such as activation of cloud droplets, diffusion growth or evaporation of

droplets, drop collisions, turbulence effects on collisions, and collisional breakup.The presented study focuses only on warm conditions and liquid clouds and, therefore, ice microphysics is not considered in the presented simulations.

The Pi chamber simulations presented here use a $64 \times 64 \times 32$ grid with grid spacing of 3.125 cm to simulate the 2 m $\times$ 2 m $\times$ 1 m box, for a physical time of 2 hours simulated with a 0.02 second time step. The grid spacing is at least 30 times the Kolmogorov length scale, hence the eddy cut off for current simulations lies in the inertial range according to Yaglom and Monin[75]. The time step is chosen to satisfy the CFL criteria. At these scales it is also possible to use under-resolved DNS with numerical diffusion playing the role of molecular diffusivity, without a subgrid scale model [76]. The energy of the system can also be dissipated via numerical dissipation instead of parameterized subgrid scale (SGS) dissipation, as in the implicit LES studies conducted by Pedersen et al.[77] and Pressel et al.[78]. However, we opted for traditional LES with SGS for scalability of the model in future. The system is initialized with a linear (unstable) temperature profile and a linear water vapor mixing ratio profile between the top and bottom walls. All velocity components are initialized to zero. The system is then allowed to spin-up to a steady state, characterized by a stable mean for turbulent kinetic energy, sub-grid scale dissipation, relative humidity, bulk mean temperature and bulk water vapor mixing ratio. Even though relative humidity exceeds 100% in part of the domain, no condensation occurs during the spin-up period, because initially no CCN are present. On reaching steady state,

after 20 minutes of physical time, a CCN source is turned on and aerosol particles begin to be continuously added to a single grid point inside the domain, mimicking aerosol injection in the real chamber. The CCN spectrum is assumed to be monodisperse, having a mean diameter of 62.5 nm, also a typical condition in Pi Chamber experiments. The CCN, on activation grow into cloud droplets and in the presence of supersaturation, the cloud droplets grow in size and are removed by settling process. Thus, the removal mechanism for CCN is activation and for the cloud droplets is gravitational settling.

3.3 Results

3.3.1 Scalar flux budget model for the Pi Chamber

We begin by introducing a flux budget model for estimating the mean supersaturation in the Pi Chamber. The model is first explored in order to understand the role of terms that are not typical in atmospheric modeling, such as the influence of sidewall heat and water vapor fluxes. Absolute measurement of supersaturation is challenging, and therefore we rely on these fundamental calculations to aid in the evaluation of LES results for supersaturation. The comparison of the flux budget model calculations to LES results is presented in Sec. 3.3.2.

The conservation law for a scalar Ψ in a volume V_0, is given by

$$\frac{\partial}{\partial t}\int_{V_0} \Psi dV \;=\; \oint_{S_0} F dS, \tag{3.1}$$

where F is the scalar flux through the bounding surface S_0. Introducing the volume-mean value $\bar{\Psi}$ and breaking S_0 into bottom, top, and side walls with areas A_b, A_t and A_s, respectively, we get

$$\frac{\partial}{\partial t}\bar{\Psi} V_0 \;=\; F_b A_b + F_t A_t + F_s A_s \tag{3.2}$$

Assuming the fluxes are driven by difference between the value of the scalar at the wall and the mean value inside the volume, i.e., $F_{b/t/s} \propto (\Psi_{b/t/s} - \bar{\Psi})$. Assuming the turbulent diffusivities for all walls to be identical Eq. 3.2 can be solved for the steady state condition, yielding

$$\bar{\Psi} \;=\; \frac{\Psi_b + \Psi_t + \hat{A}\Psi_s}{2 + \hat{A}}. \tag{3.3}$$

Here, we have exploited the fact that for a configuration with vertical side walls and parallel top and bottom planes, $A_t = A_b$, and introduced an area ratio, $\hat{A} = A_s/A_b$.

Equation 3.3 implies that the effect of the sidewall is scaled by the area ratio, which

in case of the Pi chamber is $\hat{A} = 2$. We also note that for a limiting case of infinite top and bottom plates, the sidewall effects disappears because $\hat{A} = 0$ and we have

$$\bar{\Psi} = \frac{\Psi_b + \Psi_t}{2}. \tag{3.4}$$

The same $\bar{\Psi}$ can be achieved by maintaining the sidewall value of the scalar at

$$\Psi_s = \frac{\Psi_b + \Psi_t}{2}. \tag{3.5}$$

The volume mean temperature and water vapor mixing ratio in the chamber calculated from Eq. 3.3 are given by

$$\bar{T} = \frac{T_b + T_t + \hat{A}\, T_s}{2 + \hat{A}} \tag{3.6}$$

and

$$\bar{Q} = \frac{Q_{sat}(T_b) + Q_{sat}(T_t) + \hat{A}\, Q_{sat}(T_s)}{2 + \hat{A}}, \tag{3.7}$$

with the assumption of water vapor being saturated at the walls at their corresponding temperatures. Because of the nonlinear dependency of Q_{sat} on T, we have $\bar{Q} > Q_{sat}(\bar{T})$ and supersaturated conditions are produced, as illustrated in

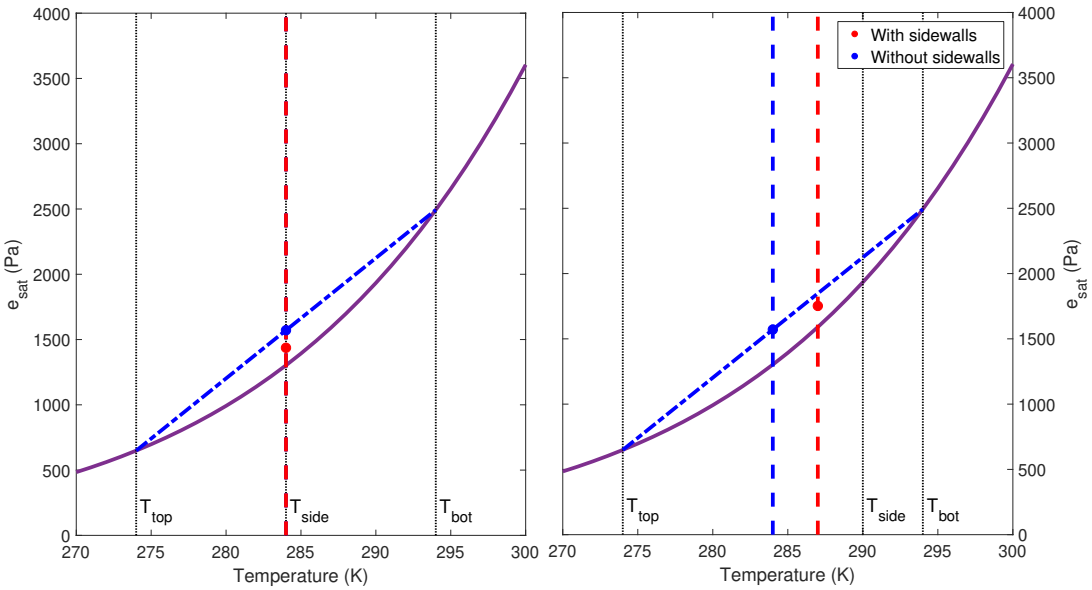

Figure 3.1: Water vapor pressure versus temperature, with the Clausius-Clapeyron-derived equilibrium curve (purple solid line), and line representing mixing between the bottom and top boundaries (blue dot-dashed line). The red and blue dashed line represent the mixing temperature with and without sidewalls respectively. [Left] The sidewalls are maintained at 284 K, the average of top wall and bottom wall temperatures of 274 K and 294 K, respectively. The blue dashed line and red dashed line coincide in this case. [Right] The sidewall temperature is 290 K, with the top and bottom temperatures at 274 K and 294 K, respectively. The red and blue markers indicate the resultant mixing saturation vapor pressure for the cases with and without saturated sidewalls.

temperature–vapor-pressure coordinates in Fig. 3.1. In this figure, $T_t = 274$ K and $T_b = 294$ K and two different sidewall conditions are shown. Without the side wall contribution, the mixture properties lie on a line segment connecting bottom an top conditions (blue dot-dashed line in Fig. 3.1). Vapor pressures on this mixing line are everywhere above the corresponding equilibrium (or saturation) vapor pressures given by the Clausius-Clapeyron equation, corresponding to the classic isobaric mixing cloud scenario [e.g., 79, Secs. 3.7 and 6.8]. Adding side walls at an intermediate temperature between T_b and T_t always reduces $\bar{Q}$ and, therefore, the supersaturation

of the mixture. For example, in the left panel of Fig. 3.1 the sidewall temperature is taken as the mean value, so that Eq. 3.5 applies. The vapor pressure and temperature that would be achieved in an ideal system with no sidewalls is shown by the blue dot, and that achieved in a system with saturated sidewalls is shown by the red dot, as calculated from Eqs. 3.6 and 3.7. The right panel of Fig. 3.1 shows the vapor pressure and temperatures for a sidewall temperature between the mean and bottom-wall temperatures.

The supersaturation is plotted as a function of sidewall temperature in Fig. 3.2. For this figure, the top wall is maintained at $T_t = 274$ K and bottom wall at $T_b = 294$ K, and the sidewall temperatures are varied from T_t to T_b. The black diamond markers show the supersaturation without any sidewall effects and the blue circular markers indicate the resulting supersaturation from Eq. 3.3. The supersaturation graph of sidewalls with supersaturation in Fig. 3.2 has two regimes dominated by heat flux and vapor flux respectively. The region to the left of the minimum, is dominated by heat flux. Roughly speaking, the sidewalls maintained at a lower temperature than the mean of top and bottom walls, act as heat sinks and result in a reduced bulk temperature compared to the case without any sidewalls. Simulations with periodic lateral boundaries, as is typical for atmospheric applications of traditional LES and DNS, without accounting for scalar diffusivities to or from sidewalls, yields a higher

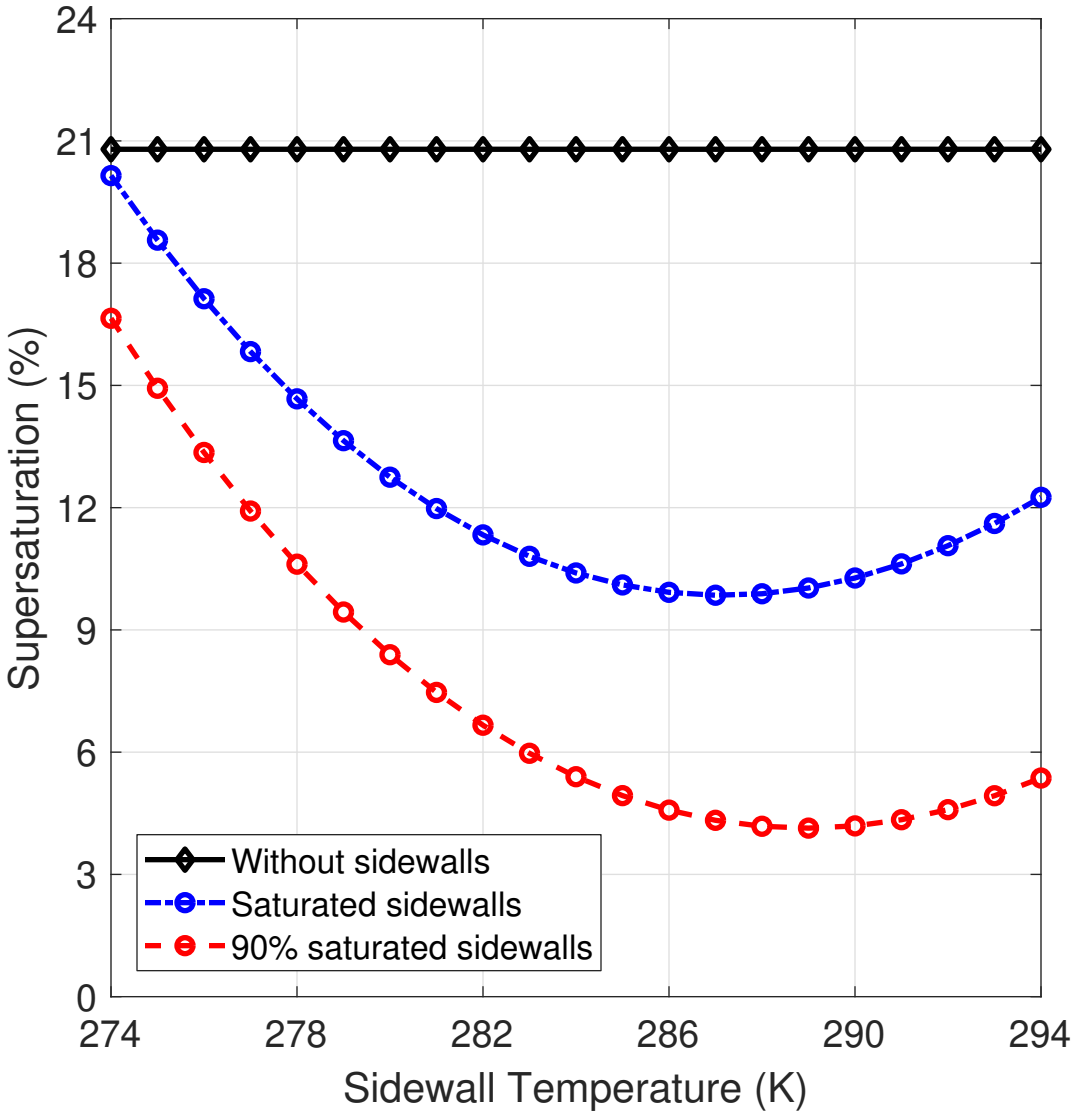

Figure 3.2: Supersaturation versus sidewall temperature, assuming no sidewalls (black diamonds), fully-saturated sidewalls (blue circles), and slightly subsaturated sidewalls (red circles). Here, it is assumed that the top and bottom wall temperatures are 274 K and 294 K, respectively.

supersaturation represented by the black diamond markers in Fig. 3.2. The right hand side of the minimum is dominated by vapor flux from the sidewalls maintained at a higher temperature than the mean of top and bottom walls. As the sidewall temperature increases, both the heat flux and vapor flux at the sidewall switches sign

from negative to positive direction. The overall supersaturation decreases as the heat flux switches sign, however it increases as the vapor flux switches sign, resulting in a minimum. A more careful derivation of the minimum point is provided in Supporting Information. The important point here is that the area weighted sidewalls leads to a depletion of supersaturation compared to an infinite parallel plate case.

All the preceding discussions assumed saturated sidewalls, however in the Pi Chamber the only source of saturation of sidewalls arises from the condensation of droplets on the sidewalls, and there are dry areas at the locations of windows. To account for this in the flux balance model, we can decrease the area of sidewalls covered with water droplets. The resulting supersaturation for a value of 90% is represented by the red line in Fig. 3.2, and as expected, it is lower compared to the saturated-sidewall conditions.

In practice, it is of interest to consider the conditions necessary to sustain cloud growth in the Pi Chamber, i.e., to achieve a supersaturation greater than zero. Sidewall conditions that are not fully saturated (or that experience some excess heat transfer, e.g., through windows) can be compensated for either by increasing the temperature difference$\Delta T = T_b - T_t$ or by adjusting the sidewall temperature T_s. The two effects are illustrated in Fig. 3.3, which shows the minimum sidewall saturation ratio necessary to attain relative humidity of 100 % (or zero supersaturation) in the Pi Chamber. The red axis and curve show the ratio as a function of ΔT, and

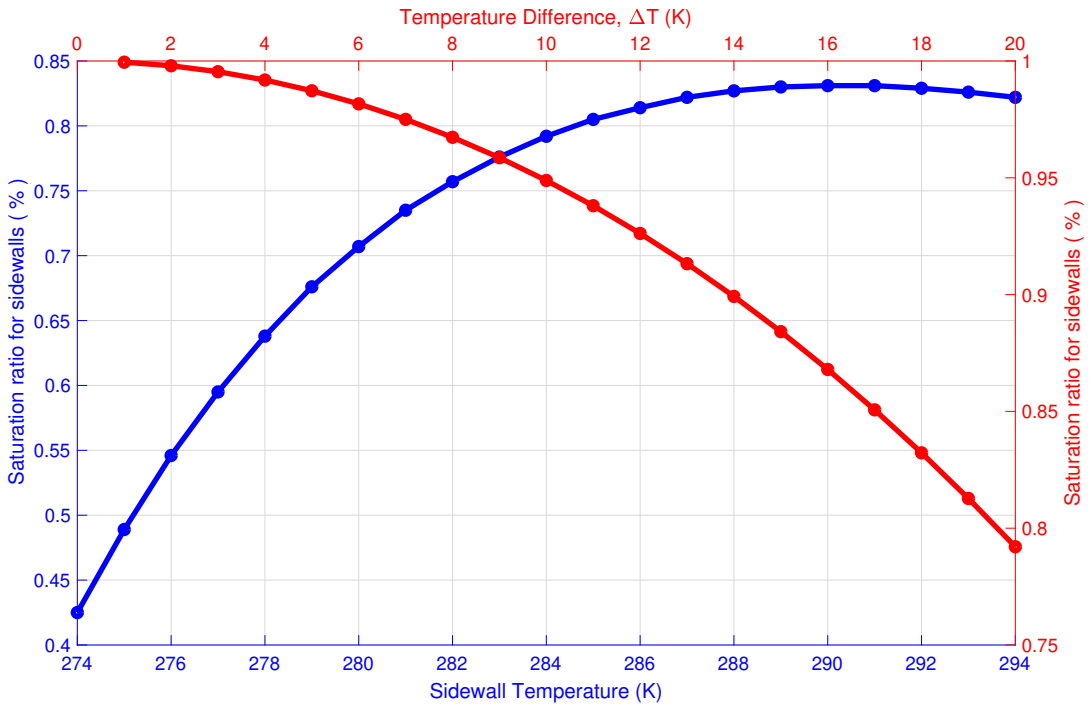

Figure 3.3: [Red] Minimum saturation ratio at the sidewall required for 100% relative humidity in the cloud chamber, versus temperature difference, ΔT. Here the sidewall temperature is kept at the mean bulk temperature of 284 K. Larger ΔT is required to compensate for drier sidewalls, in order to maintain cloud-sustaining conditions. [Blue] Minimum saturation ratio at the sidewall required for 100 % relative humidity in the cloud chamber, versus the sidewall temperature. Here the temperature difference, ΔT is kept constant at 20K and the sidewall temperatures are changed from 274 K to 294 K. A derivation describing these two curves is provided in the Supporting Information.

the blue axis and curve show the ratio as a function of T_s. At lower ΔT, we can see that a sidewall saturation ratio closer to 100%, implying a fully saturated sidewall is required to yield supersaturation. As the temperature difference increases to 20 K, a sidewall saturation ratio as low as 80% can yield supersaturation. Hence at higher temperature differences, it is easier to attain supersaturation, even if the sidewalls are not fully saturated. The blue curve shows that this can be further adjusted by varying the sidewall temperature, as was implied in the earlier discussion.

3.3.2 Scalar flux budget model compared with LES results

The flux budget model suggests that the mean supersaturation attained in the Pi Chamber depends on a combination of ΔT and T_s. This provides a reference for interpreting the mean state calculated with the LES. In this section, all LES results are for the thermodynamic state of the turbulent mixture of air and water vapor, with no cloud formation. Figure 3.4 is obtained by varying saturated sidewall temperature from T_t to T_b, for fixed ΔT. Panels showing the mean fluid temperature, water vapor mixing ratio, and relative humidity are shown. The blue circles are the results from the flux model and the red squares are from the LES, both for $\Delta T = 20$ K and with T_s increments of 2 K.

The results in Fig. 3.4 show reasonable consistency between the trends from the LES and the predictions of the relatively simple flux balance model. The mixing temperature and mixing ratio, for varying sidewalls are shown in the top two panels of Fig. 3.4. For temperature and water vapor, we can see the scalar flux model predicts slightly higher values than LES for higher sidewall temperatures and slightly lower values than LES for lower sidewall temperatures. Encouragingly, the crossover occurs at a temperature very close to the mean of T_b and T_t, $T_s = 284$ K. The offsets at smaller and larger T_s are likely due to the assumption of uniform turbulent diffusivities for top,

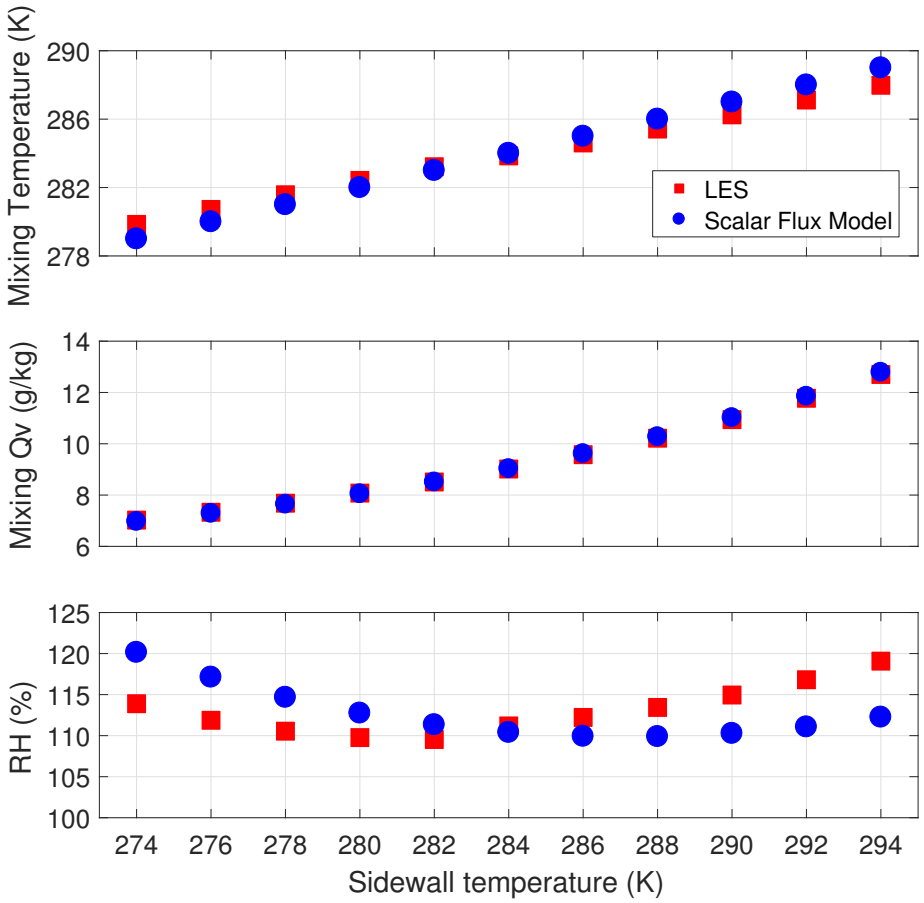

Figure 3.4: Comparison of mixing temperature, water vapor mixing ratio, and relative humidity versus sidewall temperature, as calculated from the scalar flux budget model (blue circles) and the large-eddy simulation (red squares). Results are shown for a temperature difference of $\Delta T = 20$ K with top and bottom boundaries at 274 K and 294 K respectively. LES values are obtained by averaging over the full volume, excluding grid points close to the sidewall boundaries, and averaging in time from 1800 s to 3600 s.

bottom and sidewalls in the simple scalar flux model. The relatively small discrepancies in temperature and water vapor mixing ratio result in lower supersaturation for the LES at lower T_s than predicted by the scalar flux model. Conversely, the lower mixing temperatures at higher sidewall temperatures result in a higher supersaturation for LES than the scalar flux model at larger T_s. These trends in supersaturation

are evident in the third panel of Fig. 3.4. Again, the scenario with sidewall temperature at the mean of the top and bottom boundary temperatures serves as a check (cf. Eqn. 3.5) and indeed, the supersaturation from the LES matches the prediction of the scalar flux model quite well.

Accurate experimental measurement of supersaturation and water vapor inside the cloud chamber is a matter of continuing effort, but based on the activated fraction of aerosols, and mean cloud droplet diameters, the supersaturation can be estimated as close to $1\% - 2\%$ for $\Delta T \approx 19K$ and the configuration used in several recent experiments [24, 25, 43]. In order to achieve these values of supersaturation in the LES, the sidewall saturation ratio is reduced for the simulations analyzed below. For chamber boundary temperatures of $T_t = 280$ K, $T_b = 299$ K and $T_s = 285$ K, i.e., $\Delta T = 19$ K, Eqs. 3.6 and 3.7 show that a sidewall saturated fraction of 0.74 is required to achieve 100% RH. The same set of equations predict a RH of 102.5% with a saturated fraction of 0.80. We then iterate to determine that this RH is achieved in the LES with a sidewall saturated fraction of 0.82, and this value is used in the subsequent work.

3.3.3 LES turbulence and flow properties

In this subsection we describe the flow and turbulence properties of the convection, as captured by the LES. Particle-image velocimetry measurements are also described and compared to the LES in order to evaluate the model performance.

Figure 3.5 shows the time-averaged temperature and water vapor mixing ratio profiles along the axis of gravity for the conditions before and after aerosol injection. As expected for turbulent Rayleigh-Bénard convection, the temperature and the mixing ratio remain relatively constant throughout the bulk of the chamber due to the efficient mixing of the turbulence. The strongest gradients in temperature and water vapor mixing ratio are found near the top and bottom boundaries. In Fig. 3.5 we can see that the temperature profile shifts to the right when aerosol is introduced and a cloud is formed, indicating an increase in temperature, owing to the latent heat release due to the condensation growth of cloud droplets. This process in turn decreases the available water vapor in the bulk causing the mixing ratio curves to shift to the left as illustrated in the figure.

The turbulent kinetic energy (TKE), energy dissipation rate ε, and the frequency of oscillations of the large-scale circulation are measures of the convective turbulence inside the chamber. Matching TKE and ε from the LES with experimental results

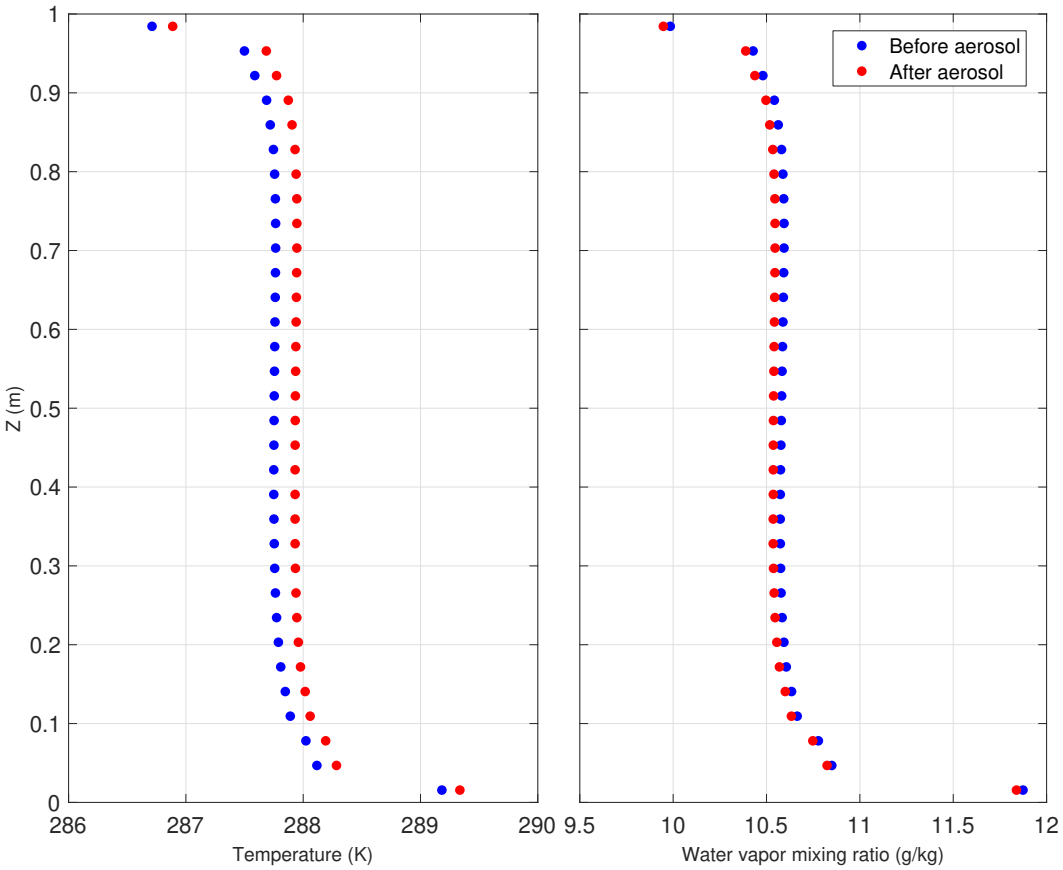

Figure 3.5: Vertical profiles of horizontally-averaged temperature and water-vapor mixing ratio. Profiles are shown for cloud-free, i.e., no aerosol particles, conditions (red circles), for a temperature difference of 20 K with T_b, T_s, T_w at 294 K, 284 K and 274 K, respectively. The results are obtained by averaging over time from 1800 s to 3600 s in the chamber simulation.

indicates that the boundary fluxes are properly evaluated. We use Particle Image Velocimetry (PIV) to visualize and measure the 2-dimensional velocity field at the center of the chamber. A 200 mW CW laser is used in combination with a laser-line-generator lens to illuminate a sheet of droplets at the center of the chamber. The illuminated droplets are recorded using a CCD camera (Alpha 7S2, Sony) at a framerate of 120 fps and a resolution of 1920×1080 pixels at $\approx 60 - 100$ μm/pixel, depending on the field of view (20×10 to 10×5 cm^2). By using the cloud droplets as a

fluid tracer, no additional particulates (such as oil droplets, or polymer powder) have to be introduced into the cloud environment. This requires that the Stokes number of the droplets, $St = \tau_d/\tau_\eta$ is very small, where $\tau_d = \rho_l d^2/18\nu\rho_a$ is the droplet response time and $\tau_\eta = (\nu/\varepsilon)^{1/2}$ is the turbulence dissipation eddy time scale. Here ρ_a and ρ_l are mass densities for air and liquid water, respectively, and ν is the kinematic viscosity of air. For the droplet distributions used in this experiment, assuming an (expected) dissipation rate $\varepsilon \approx 10^{-3}$ m^2 s^{-3} [21], the Stokes number results vary on the order of $10^{-5} - 10^{-3}$, and therefore droplets serve as reasonable tracers.

To obtain a converged estimate of the turbulence statistics, the camera records the droplet dynamics for approximately an hour for each condition measured. Image pairs at a time delay of $\Delta t = 1/120$ s are sampled at 2 Hz, resulting in approximately 2500-4000 image pairs per experiment (accounting for adequate averaging). Commercial PIV software (Pivtec, PIVTEC Gmbh) was used to process the images. PIV correlation windows of 48×48 and 64×64 pixels are used, depending on the droplet number concentration and field of view, with a consistent window overlap of 50%.

To determine the TKE, the root-mean-square of the droplet velocity components (in both horizontal (u) and vertical (w) directions) are averaged over the available data, i.e., $U = \sum (u^2 + w^2)^{1/2}$, where the sum is taken over the full PIV window and all available image pairs.

The dissipation rate ε can be estimated using the Smagorinsky turbulence model

from the measured velocity gradients in the PIV. As the measurement has a limited resolution, the minimum PIV window size (5 cm) is 50 times larger than the Kolmogorov length (1 mm) of the small-scale turbulent eddies. This results in an inherent filtering of the turbulent velocity field, which requires a correction of the resulting dissipation rate, detailed by Bertens et al.[80]. This correction, based on the size of the PIV window to the Kolmogorov scale η, gives an uncertainty $\approx$25% in homogeneous, isotropic turbulence. It should also be noted that the turbulence in Rayleigh-Bénard convection is somewhat anisotropic, so the equipartition of TKE is not strictly valid and therefore we make the comparison of PIV and LES results in 2D.

The left two panels of Fig. 3.6 show the comparison of the average TKE and ε for LES (blue circles) and experiments (red squares), for four different values of ΔT. As expected, in the experiments both the turbulent kinetic energy and consequently the energy dissipation rates increase as the temperature difference is increased. The LES captures a quantitatively similar trend. The TKE and ε from the simulations are slightly higher than the experimental observations, but within the experimental uncertainties.

The presence of a coherent, large-scale circulation in Rayleigh-Bénard convection within the Pi Chamber has been documented by Andersen et al.[81]. Encouragingly, the LES also produces a large-scale circulation, and it is observed to experience

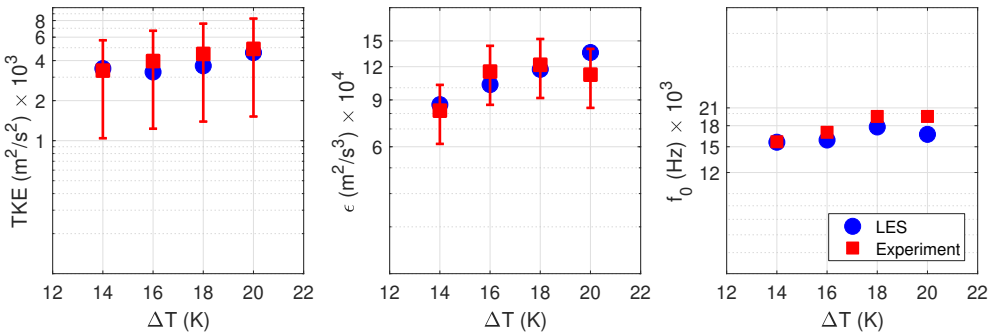

Figure 3.6: Turbulent kinetic energy (TKE), eddy dissipation rate (ε), and large-scale oscillation frequency versus temperature difference ΔT. The LES results are shown by the blue circles and the experimental results by the red squares. The LES results are time averaged between $1800 - 3600$ s. The 2D TKE is calculated from the u and w velocity fluctuations, and similar to the experimental results, the effect of large-scale oscillations are filtered by subtracting a moving mean over 1 minute from the point measurements in the simulation. ϵ is obtained from the center plane and the large-scale oscillation frequency is obtained from the FFT of point temperature measurements in the simulation.

oscillations similar to the experiments. To determine the frequency of large scale oscillation in the LES, a Fourier analysis is performed on the temperature sampled at 50 Hz from a point at the center of the chamber. From the frequency spectra thus obtained, the maximum between 0.1 to 0.01 Hz is identified as the large scale oscillation frequency (an example of a frequency spectrum is shown Figure 1 in the Supplemental Materials).

As shown in the right panel of Fig. 3.6, the LES is able to qualitatively, and even to some extent quantitatively capture the frequencies measured in the cloud chamber experiments.

3.3.4 Simulated steady-state cloud

A primary motivation for experiments in the Pi Chamber is to study aerosol-cloud-turbulence interactions in a controlled environment [21]. For example, Chandrakar 2016 & 2018[24, 43] found that the width of cloud droplet size distribution increases with a decreasing aerosol injection rate, and this broadening is due to a combination of mean and variability in the diffusional growth of cloud droplets in a turbulent environment, rather than broadening due to the collision-coalescence process. However, there is only indirect observational evidence to support the predominant role of condensation growth including a significant contribution from turbulence, as well as the absence of collisions in the chamber. This is because the growth history of individual cloud droplets is unknown (and currently unobservable), and only the distribution properties are known. The modified cloud-resolving LES in this study provides a useful tool to study the relative roles of condensation and collisions in the growth process, and on the cloud droplet size distribution in the cloud chamber.

Here we present the results of the simulated steady-state clouds in detail, as a parallel study to Chandrakar 2016 & 2018[24, 43]. The scientific questions we want to address are (1) can the model simulate the microphysical properties of steady-state clouds? (2) do simulations reproduce the broadening of cloud droplet size distribution with the decrease of cloud droplet number concentration? (3) does the collision-coalescence

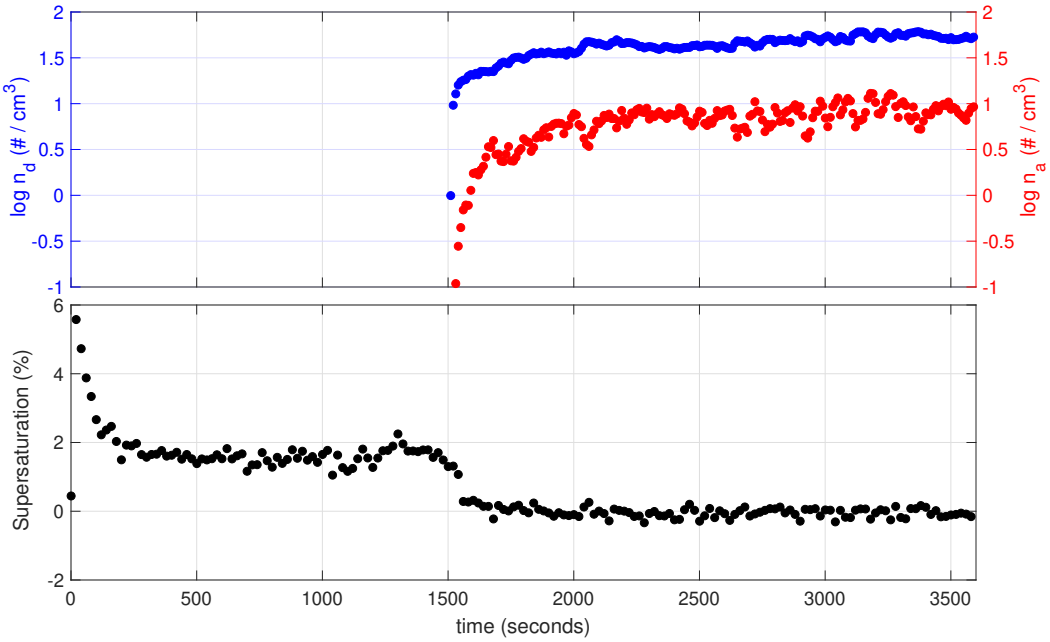

Figure 3.7: Time series of cloud droplet number density (top panel, blue circles), aerosol concentration (top panel, red circles), and supersaturation (bottom panel, black circles). Up to a time of 1500 s no aerosols or cloud droplets are present, and at 1500 s a steady injection rate of aerosol particles is initiated. The plots are volume averaged droplet concentration, CCN concentration and supersaturation, excluding the grid points close to the boundaries.

process really play a negligible role in droplet growth in the chamber? It should be mentioned that this model can also be applied to investigate several other processes, including cloud cleansing and collapse [25], and the influence of variable cloud microphysical properties on stochastic condensation [27]. Simulations under those conditions will be investigated in the future. For this paper, our purpose is to demonstrate that previously-published, steady-state microphysical results can be reasonably replicated by the LES.

The simulation is set up with a temperature difference of 19 K, with bottom, top

and sidewall temperatures set to 299 K, 280 K and 285 K, respectively. The cloud box is modeled with a grid size of 3.125 cm and a step size of 0.02 seconds. The top and bottom walls are saturated and the sidewall saturation ratio is set to 0.82 to ensure a mean supersaturation of 2.5% when no cloud droplets are present. The cloud microphysical processes are simulated using a bin microphysical scheme [73]. There are 33 mass-doubling bins for aerosol and 33 mass-doubling bins for cloud droplets. Aerosol particles in one bin are activated as cloud droplets if their critical supersaturation is smaller than the environmental supersaturation in that grid box, based on Köhler theory. Diffusional growth, collisional growth and sedimentation of cloud droplets are considered. To mimic the constant aerosol injection rate during the experiments [24, 43], a point source of monodisperse aerosol with a fixed number concentration is added at the center of the simulation domain. It should be mentioned that instead of injecting aerosol in the simulation domain, we forced a constant aerosol number concentration in one grid box (at the center). This is because the current LES model and microphysical scheme lack two important sinks for aerosols: cloud scavenging and wall loss. Without those processes, the simulated aerosol number concentration will continuously increase with time for a constant aerosol injection rate, which is not consistent with the observed steady-state aerosol number concentration in the cloud chamber. (In experiments, steady state conditions in cloud properties are reached before steady state conditions in aerosol concentration because of the differing sinks for the two. See, e.g., Fig.1 in Chandrakar et al.[25].) The total simulation time

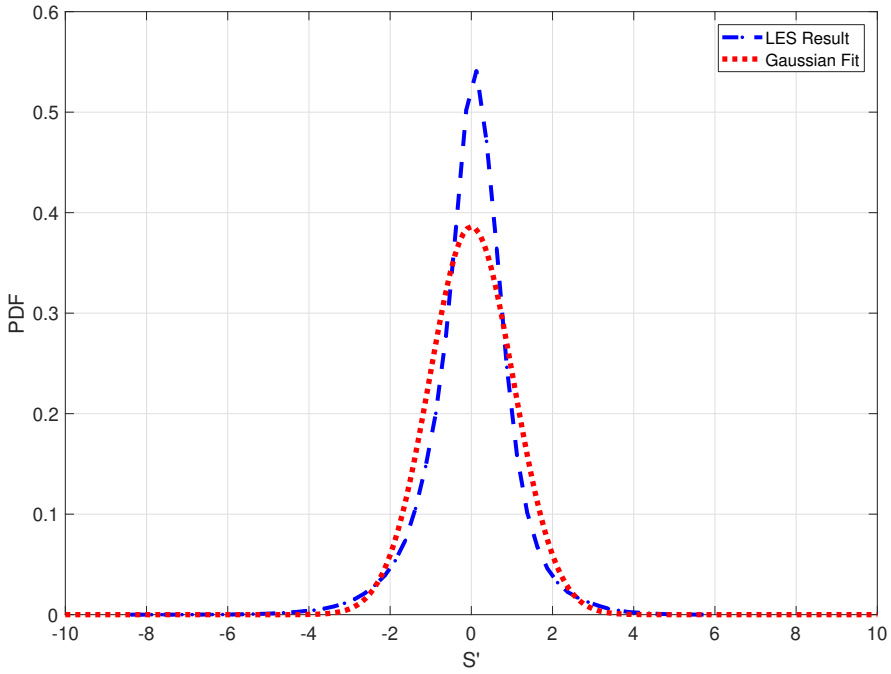

Figure 3.8: The PDF of supersaturation fluctuations at the center of the chamber, with no aerosol injection. The standard deviation is 1.033. The measurements are from spatial and temporal averages within the simulated chamber. The kurtosis of the supersaturation is 5.7, greater than 3 for Gaussian, implying greater excursions of supersaturation fluctuation from the normal distribution.

is one hour: without aerosol input for the first half an hour and with aerosol input for the second half an hour.

Figure 3.7 shows the time series of the domain-averaged cloud droplet number concentration, aerosol number concentration, and relative humidity for one cloud simulation with an aerosol source number concentration of 3697 cm^{-3} for the bin centered at 62.5-nm diameter at the center of the chamber. It can be seen that cloud does not form without aerosol input within the first half an hour, even though the relative humidity is above 100%. The domain-averaged relative humidity reaches a steady

state of about 102% after about 100 s. Relative humidity varies due to fluctuations in temperature and water vapor within the turbulent environment [82]. The PDF of supersaturation fluctuations ($s' = s - \bar{s}$) at the center of the chamber without aerosol input is similar to a Gaussian distribution, as shown in Fig. 3.8. This is consistent with the observational results [24] and the assumptions made in several additional studies [25, 27, 43]. It should be noted, however, that the LES suggests a somewhat more intermittent distribution than Gaussian, with a kurtosis of 5.7; this departure and its possible implications will be interesting topics for an additional study in the future. When aerosols are introduced to the simulation domain, the relative humidity decreases as expected due to the formation and growth of cloud droplets (bottom panel of Fig. 3.7). Cloud droplet number concentration, aerosol number concentration and the relative humidity reach a steady-state, consistent with the observations [21]. Finally, the PDF of supersaturation fluctuations after the cloud has formed becomes narrower, as expected (see Figure 2 in Supplemental Materials).

To investigate the influence of aerosol concentration on the cloud droplet size distribution, we did sensitivity studies by changing the aerosol number concentration of the point source. Four different aerosol number concentrations were implemented by maintaining concentrations of 3697 cm^{-3}, 5545 cm^{-3}, 7394 cm^{-3} and 9242 cm^{-3} at the center of the chamber. The mean and standard deviation of cloud droplet diameter during the steady state, as obtained from both a temporal and spatial average, are calculated for each case. Figure 3.9 shows that both the mean and the standard

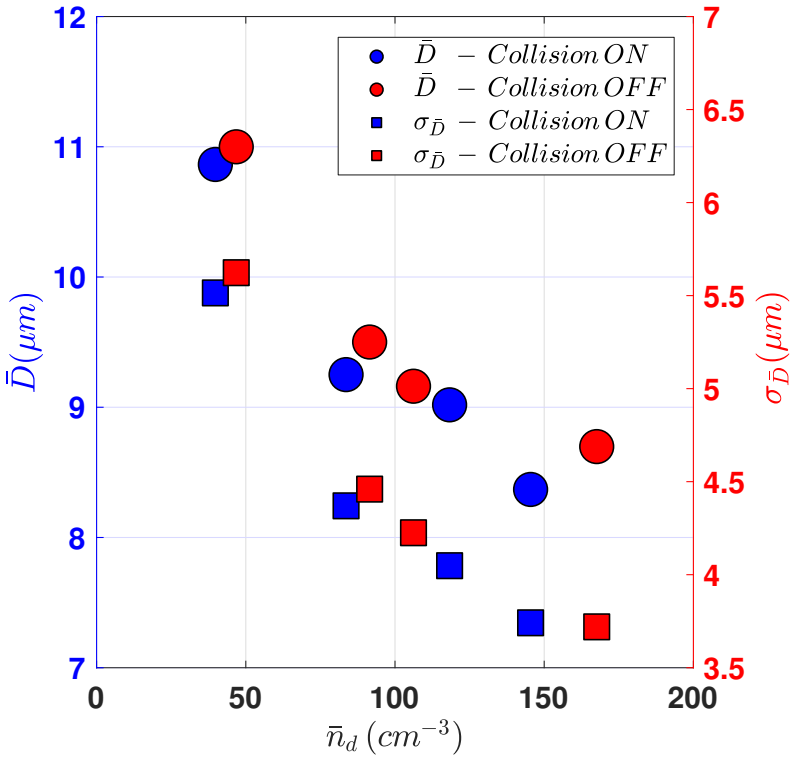

Figure 3.9: Mean (circles) and standard deviation (squares) of cloud droplet diameter versus cloud droplet concentration.Blue symbols denote collisions on and red symbols denote collisions off. The relative dispersion ($\sigma_r/\bar{r}$) varies from 0.51 to 0.42 with increasing cloud droplet concentration for cases with collisions off. Size distributions are obtained from the number per bin at each grid point in the bulk of the chamber for a single snapshot, and mean and standard deviations are calculated from the distributions.

deviation of droplet size decrease with increasing cloud droplet number concentration, which is consistent with the observations of Chandrakar [24, 43]. The trends are consistent, but the exact values of mean diameter and standard deviation do not closely match the observational results (e.g., Table 1 in Chandrakar et al.[24]), especially for relatively clean conditions, where the simulated mean diameter and standard deviation are both smaller than the observations. This might be due to the different averaging procedures in LES versus experiment, the differences in injected aerosol

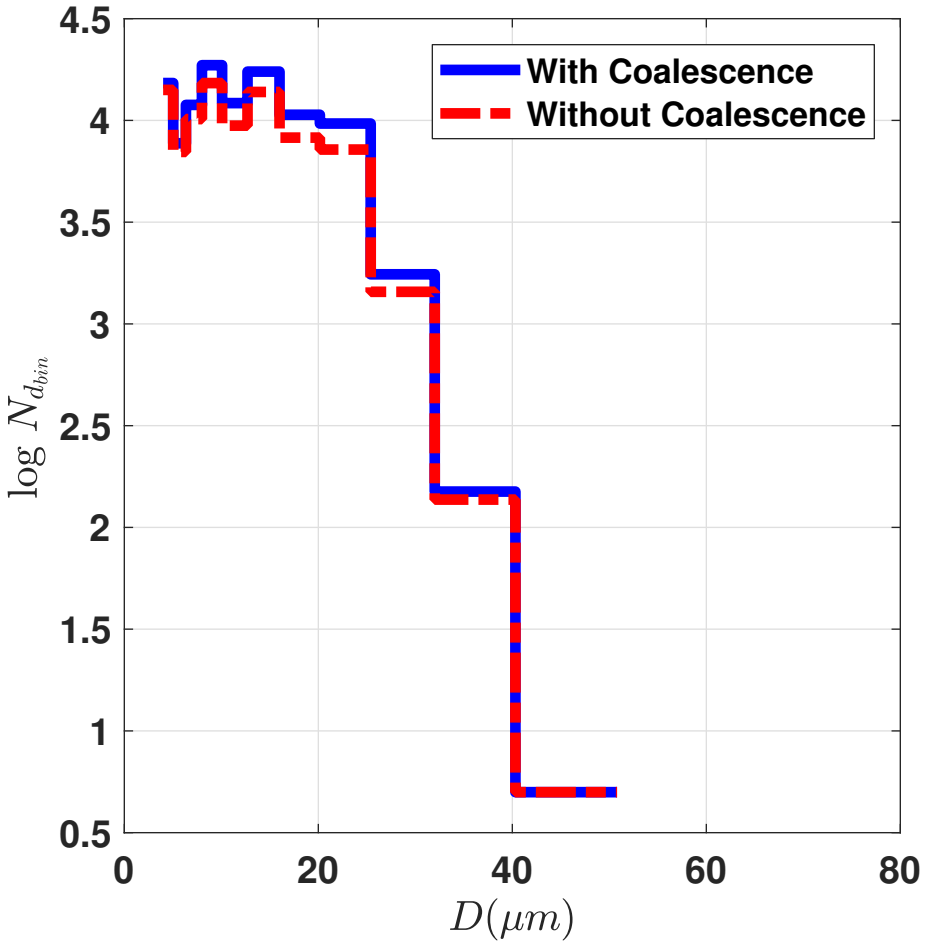

Figure 3.10: Number of droplets observed in the cloud chamber simulation versus the diameter for one set of aerosol conditions. The collision coalescence physics is turned on and off in the simulations for blue and red, respectively. The distribution is obtained from the number of droplets per bin at each grid point in the bulk of the chamber, for a single snapshot.

size distribution, the measurement uncertainties, or the inaccurate representation of either dynamics or microphysics or both. A careful investigation of this will be carried out in the future. Finally, we note that examples of size distributions due to aerosol injection are shown in Figure 3 in the Supplementary Materials file.

The LES model can simulate and maintain a steady-state cloud by adding a source of

aerosol with a constant aerosol number concentration (cf., Fig. 3.7). Modeling results also show the broadening of cloud droplet size distribution with the decrease of cloud droplet number concentration (Fig. 3.9). These results are consistent with observations Chang et al. and Chandrakar et al. [21, 24], implying that the cloud-resolving LES model captures the essential cloud microphysical properties in the convection chamber. An additional question is, does the collision-coalescence process contribute to the observed broadening of the droplet size distribution? In order to answer this question, we did another set of simulations without the collision-coalescence process. An example result is shown in Fig. 3.10, corresponding to an aerosol concentration of 5545 cm^{-3} at the center of the chamber and a steady-state cloud droplet concentration of 40 cm^{-3} without coalescence and 47 cm^{-3} with coalescence. The results, which are representative of the other cases, show that the shape of the cloud droplet size distribution does not change significantly without the collision-coalescence process. This confirms that the width of the droplet size distribution is primarily a result of the vapor condensation process. The small change in droplet concentration observed between the with and without coalescence runs is intriguing and is the topic of ongoing study. We note, however, that the estimate of mean diameter varies spatially and temporally, so determining what differences are a result of statistical fluctuations versus actual changes in mean properties, will require careful averaging. For example, for the results shown in Fig. 3.9, the standard deviation of the estimate of the mean diameter, estimated from spatial variations at one time, is between 0.2 and 0.5

μm. Thus, interpreting the small changes in distribution shape when collisions are included or not, will require longer averaging.

3.4 Summary and Discussion

The System for Atmospheric Modeling (SAM) LES code coupled with spectral-bin cloud microphysics, has been modified to simulate conditions in the Pi Chamber. To accommodate the presence of the lateral and top walls, momentum and scalar fluxes are implemented using Monin-Obukhov similarity with the roughness parameter scaled for quantitative matching. The top and bottom walls are held at saturated conditions and at constant temperatures during the simulations, with an unstable temperature difference that drives turbulent Rayleigh-Bénard convection. The lateral walls are prescribed a saturated fraction to achieve realistic supersaturation levels consistent with the condensation growth observed in the cloud chamber experiments.

A flux balance model is introduced to quantify the steady state scalar values, and this model is used to explore the supersaturations achieved by treating temperature and water vapor mixing ratio as independent scalars. The presence of the sidewalls decrease the supersaturation from the maximum attainable values for an idealized condition with no sidewalls. The supersaturation thus attained can be further decreased by the presence of an additional heat flux or partially saturated sidewalls.

The trend predicted by the flux balance model is faithfully replicated by the LES model.

With these changes to SAM, the results from the simulation agree adequately with the experiments in terms of dynamics and microphysical properties. The dynamics, measure by TKE, turbulence energy dissipation rate, and oscillation frequency of the large-scale circulation are within the uncertainty range of experiments. Furthermore, key microphysical behaviors observed in experiments with the Pi Chamber are able to be reproduced in the simulations. Specifically, steady-state microphysical conditions are achieved for a constant injection of aerosol particles to the chamber; the supersaturation field in the cloud chamber shows an approximately Gaussian distribution; mean and standard deviation of the cloud droplet size distribution increase monotonically with decreasing cloud droplet number density; and finally, the droplet growth is dominated by condensation rather than collisions for typical conditions in the cloud chamber. Taken together, these results imply that there is reasonable scalability of the LES model and the microphysical processes to the laboratory context.

The initial motivation for developing a LES of the convection and aerosol-cloud interactions in the Pi Chamber was to more deeply understand and interpret laboratory observations, which are usually Eulerian in nature and do not provide easy access to some important variables, like absolute water vapor supersaturation (water vapor fluctuations can be more reliably quantified). But as the work progressed we began

to see it in a broader context. First, LES provides an excellent opportunity to scale processes and results observed in the laboratory to a more realistic atmospheric context. In that sense, it is especially compelling to perform this study with a model like SAM that is widely used in the cloud community.

Second, and perhaps more ambitiously, LES not only can inform the experiments and allow for re-scaling of results, but also provides an opportunity to evaluate and even, at some stage, to validate numerical models for turbulence and microphysics. Simply put, intercomparison with a steady-state laboratory flow with known boundary conditions, and carefully measured properties, allows LES and bin microphysics to be compared to experiment with a level of detail and precision heretofore not possible. The atmospheric-boundary-layer community has a history already of synergy between laboratory experiments and LES [67, 83, 84, 85]. Furthermore, the need for such intercomparison has been emphasized. For example, Stevens [86] pointed out the need for "initiatives to develop symbiotic relationships between observations, experiments, and LES" and Wyngaard[46] particularly emphasized the role of laboratory experiments: "A remaining and not widely acknowledged problem is the great difficulty of testing the fidelity and reliability of the LES results. Here laboratory flows can serve as ground truth, since they generally provide 'cleaner', less scattered data than the atmosphere itself." The cloud physics community, in contrast, has long relied on laboratory experimentation for the investigation of fundamental processes, often linked to single particles, such as ice nucleation or collision efficiencies. But to

our knowledge, there has been little discussion of the potential benefits of comparing the observed dynamics of ensembles of aerosol and cloud hydrometeors within a turbulent flow directly with cloudy LES. In that regard, we consider this as a first, tentative step, with emphasis on description of the LES model as applied to the Pi Chamber, and sufficient evaluation of the flow dynamics and cloud microphysical properties to provide support for the further study. Many opportunities for detailed intercomparison focused on specific problems now are possible: the role of supersaturation mean and fluctuations on the broadening of size distributions, and the role of collision-coalescence under varying aerosol conditions stand out as examples. For the purposes of the current study, the default bins from HUJISBM are sufficient to capture the general trends observed in the experiments. However, to study other aspects of aerosol-cloud interactions, such as, for example broadening of DSD due to Ostwald ripening [87], one might have to rely on other approaches such as 2D bin microphysics[88, 89]. Grabowski et al.[90] have pointed out the challenges in modeling cloud microphysics using the popular bulk and bin methods, including the effect of numerical diffusion both in radius space and vertical advection causing artificial broadening, and they propose Lagrangian particle methods described by Andrejcuk et al., Shima et al., Solch et al., and Riechelmann et al.[49, 51, 91, 92] as a promising way forward. Thus, a potential extension of the current work would be to explore cloud chamber modeling using Lagrangian particles and an intercomparison with a laboratory validated LES study presented in this paper.

Chapter 4

Dimensionless parameters for cloudy convection: Supersaturation, Damköhler, and Nusselt numbers

"It's always seemed like a big mystery how nature, seemingly so effortlessly, manages to produce so much that seems to us so complex. Well, I think we found its secret. It's just sampling what's out there in the computational universe."

- Stephen Wolfram

Abstract

In turbulent, dry Rayleigh-Bénard convection under steady-state conditions, the sensible heat flux is constant with height. When water vapor is present and cloud formation occurs, there is also an additional latent heat flux component, and the exact flux profiles of each of these components depends on the microphysical state of the clouds: specifically, whether substantial supersaturations exist and whether cloud liquid water is removed through sedimentation/precipitation. In this article we bridge between the Rayleigh-Bénard convection literature and the atmospheric literature. We express the governing equations for cloudy convection in dimensionless form, thereby explicitly identifying the governing parameters of Rayleigh and Prandtl numbers, as for dry convection, as well as Schmidt, Damköhler, and sedimentation numbers for the cloudy case. We further connect to the atmospheric literature by obtaining a microphysics-independent heat flux Nusselt number (dimensionless heat flux) for a cloud–convection system, directly from the conservation equations for temperature and water vapor. This flux has the same form as that identified by Zhang et al. (2019) for convection with water vapor, but is extended to the cloudy case, and is independent of the microphysical details of the system, such as liquid water mixing ratio and cloud droplet number concentration and size distribution. For equal thermal and water vapor diffusivities, the flux corresponds to the widely-used atmospheric quantities equivalent temperature and moist static energy. We illustrate

the microphysic independence through a large eddy simulation (LES) of an idealized cloudy Rayleigh-Bénard convection system with fixed boundary conditions. From the results, we show the height-dependence in the profile of sensible heat flux and latent heat flux, depending on the liquid water content, whereas the modified heat flux remains a constant throughout the height of the chamber.

4.1 Introduction

Classical Rayleigh-Bénard convection is described by the Rayleigh number, $Ra = g\beta\Delta T H^3/(\nu_T \nu)$, which captures the competing roles of buoyancy forcing and diffusive losses, and the Prandtl number, $Pr = \nu/\nu_T$, which is a material parameter defining the relative magnitude of diffusion of momentum and thermal energy. Here, g is the gravitational acceleration, β is the coefficient of thermal expansion, ν_T is the thermal diffusivity, ν is the kinematic viscosity, and H is the separation distance between surfaces with imposed temperature difference ΔT. For sufficiently large Ra and $Pr \sim 1$ relevant to atmospheric flows, the convecting fluid is strongly turbulent. The hallmark of turbulent convection, in turn, is highly efficient transport of energy. The non-dimensional heat flux is given by the Nusselt number Nu, the ratio of the total heat flux to the conductive heat flux ($\nu_T \Delta T/H$) across an identical, static fluid

layer:

$$Nu = \frac{\overline{w'T'} + \nu_T \nabla_z \overline{T}}{\nu_T \Delta T / H}, \tag{4.1}$$

where w is the vertical component of velocity, overline denotes ensemble average over a horizontal surface and prime denote fluctuations from the mean [33]. By definition, in steady state this horizontally-averaged heat flux is constant with height within the convecting fluid. Seeking an understanding of the Nusselt number and its dependence on the Rayleigh number remains a challenge even for single-fluid ('dry') convection [33, 37]. When phase changes are included at the boundaries, even in idealized laboratory convection experiments, the heat flux problem becomes much more complex [93]. Furthermore, the flux problem becomes complex in the presence of phase change effects in the bulk as it introduces an additional heat source/sink via latent heat associated with the phase change processes [41, 94]. Additionally, the amount of condensate in the system depends on the rate at which phase change effects occur (e.g., condensation/evaporation). In the context of cloudy convection, the rate of evaporation/condensation is strongly influenced by the properties of the cloud droplets including size, number concentration, etc (henceforth, referred to as 'microphysics'). For example, if the condensate load is fixed, plentiful small droplets allow for efficient conversion of water vapor to the condensed phase compared to a few large droplets. Additionally, small droplets have lower sedimentation velocities and thus result in a higher condensate load in the system [41].

The idealization of Rayleigh-Bénard convection has a long history in guiding our understanding of cloud formation [53, 95, 96, 97, 98, 99]. In the atmospheric context the conundrum posed by the interaction between temperature, water vapor and liquid water on large scales is circumvented by using conserved variables derived from thermodynamics. However, for cloudy convection non-equilibrium conditions can exist depending on the microphysics, thereby making troublesome entropic variables derived under ideal assumptions of reversibility. At the same time, the fluid dynamics community making no such assumptions explored the parameter space for moist convection in the absence of any liquid water [93]. In Section 4.2, we present the governing equations for cloud Rayleigh-Bénard convection and introduce and discuss the associated dimensionless parameters. Then in Section 4.3 we provide a non-thermodynamic derivation of a microphysics independent heat flux and subsequently a Nusselt number independent of any cloud droplets analogous to and thus expanding the scope of the Nusselt number proposed by Zhang et al.[93]. Furthermore, under the assumptions of constant molecular/turbulent diffusivities of temperature and water vapor, we retrieve the equivalent temperature and moist static energy from the flux derivations that are widely used in the atmospheric sciences community (see Section 4.3). Both equivalent temperature and moist static energy are derived using only the first law and therefore avoid problems of reversibility [79, 100]. It should be noted that the microphysics-independent flux is not limited to atmospheric applications but can be extended to systems with phase change and chemically reactive systems (see

Section 4.6).

In this article we aim to connect the Rayleigh-Bénard literature with the atmospheric science literature in two ways. We present the equations for cloudy convection in dimensionless form, making clear the relevant parameters describing the system. As described in the previous paragraph, we derive a microphysics-independent Nusselt number for cloudy Rayleigh–Bénard convection, directly from the equations for temperature and water vapor mixing ratio. Entropy conservation is not assumed in the derivation and thus non-equilibrium conditions can be adequately represented; nevertheless, the derived heat flux is constant with height throughout the convection system, independent of the dimensionless parameters related to the microphysical properties of the cloud. We present Large Eddy Simulations (LES) of cloudy Rayleigh-Bénard convection with varying aerosol conditions to explore and illustrate the characteristics and the utility of the approach. In the final section we discuss the prospective implications of the conserved flux and its applications, as well as its connections to atmospheric variables.

4.2 Governing Equations and Dimensionless Parameters for Cloudy Convection

4.2.1 Governing equations in dimensional form

The Navier-Stokes equation for cloudy convection can be written as ([101])

$$\begin{aligned} \frac{\partial U_i}{\partial t} + U_i \cdot \nabla U_i &= -\frac{1}{\rho_a}\nabla p + \left[\, \beta \left(T - \overline{T}\right) + \epsilon \left(Q_v - \overline{Q_v}\right) - Q_L \,\right] g\hat{z} \\ &\quad + \nu \nabla^2 U_i, \end{aligned} \tag{4.2}$$

where U is the velocity vector, ρ_a is the density of air, p is the pressure, and ν is the kinematic viscosity. The buoyancy term contains three contributions multiplied by the gravitational acceleration g, which is assumed to act in the vertical $\hat{z}$-direction. First, the usual term depending on the difference between the temperature T and the average value $\overline{T}$, multiplied by the thermal expansion coefficient β. Second, a contribution from the perturbation in water vapor mixing ratio Q_v (the ratio of the mass of water vapor to the mass of the dry air) multiplied by term $\epsilon = m_d/m_v - 1$, where m_d and m_v are the molecular weights of dry air and water vapor, respectively.

Third, a contribution of the liquid water mixing ratio Q_L, which accounts for the drag force applied to the fluid due to settling cloud droplets.

For a cloudy convective system with phase change effects, the continuity equation, the energy equation and the water vapor and liquid mass balance equations are given by

$$\frac{D\rho}{Dt} + \rho\nabla \cdot U_i = 0 \tag{4.3}$$

$$\frac{\partial T}{\partial t} = \nabla \cdot (-U_i T + \nu_T \nabla T) + \frac{L}{C_p}\dot{Q}_L \tag{4.4}$$

$$\frac{\partial Q_v}{\partial t} = \nabla \cdot (-U_i Q_v + \nu_v \nabla Q_v) - \dot{Q}_L, \tag{4.5}$$

$$\frac{\partial Q_L}{\partial t} = \nabla \cdot (-U_i Q_L + w_T Q_L) + \dot{Q}_L, \tag{4.6}$$

where ν_T and ν_v are thermal and water vapor diffusivities respectively, w_T is the terminal speed of a cloud droplet, and $\dot{Q}_L$ is the rate of condensation/evaporation of water. It should be noted here that, while we include the sedimentation term in

equation 4.6, we have not included a corresponding energy-loss term in equation 4.4 because for typical cloud conditions the thermal inertia of droplets is negligible.

4.2.2 Non-Dimensional formulation

It is instructive to consider the non-dimensional form of the governing equations. We take the height of the chamber (H) and the free-fall velocity for dry Rayleigh-Bénard convection ($w = \sqrt{g\,\beta\,\Delta\,T\,H}$) as the scales for length and velocity. The non-dimensional scaled variables (denoted by tilde on the top of the variable) of length, time, velocity, temperature and water vapor for moist Rayleigh–Bénard convection are $\tilde{L} = L/H$, $\tilde{t} = tw/H$, $\tilde{U} = U/w$, $\tilde{T} = \frac{T-\overline{T}}{\Delta T}$, $\tilde{Q_v} = \frac{Q_v - \overline{Q_v}}{\Delta Q_v}$. The acceleration due to gravity is g, thermal expansion coefficient is β and ϵ is the ratio of dry air to water vapor gas constants. The non dimensional momentum equation is written as

$$\frac{\partial \tilde{U}}{\partial \tilde{t}} + \tilde{U} \cdot \tilde{\nabla}\tilde{U} = \frac{-1}{\rho_a}\tilde{\nabla}\tilde{p} + \left(\tilde{T} + B_v\,\tilde{Q_v} - B_L\right)\hat{z} + \sqrt{\frac{Pr}{Ra}}\tilde{\nabla}^2\tilde{U}$$

where, Ra is the Rayleigh number ($Ra = \frac{g\,\beta\,\Delta T\,H^3}{\nu_T\,\nu}$), Pr is the Prandtl number ($Pr = \nu/\nu_T$). The second term grouped within brackets on the right hand side of the non-dimensionalized Navier-Stokes equation is the buoyancy contribution to

momentum, and acts along the direction of gravity. The buoyancy contribution comes from temperature, water vapor and the drag associated with the sedimentation of the condensate. The dimensionless parameter for water vapor is $B_v = \epsilon \Delta Q_v/(\beta \Delta T)$ and that for liquid water is $B_L = Q_L/(\beta \Delta T)$.

The dimensionless equation for temperature (equation 4.4) can be rewritten as follows

$$\frac{\partial \tilde{T}}{\partial \tilde{t}} + \tilde{U} \cdot \tilde{\nabla} \tilde{T} = \frac{1}{\sqrt{Ra\, Pr}} \tilde{\nabla}^2 \tilde{T} + \frac{L}{C_p \Delta T} \frac{H}{w} \frac{Q_L}{\tau_{cond}}. \tag{4.7}$$

Here we have taken $\dot{Q}_L = Q_L/\tau_{cond}$, where τ_{cond} is a characteristic time for the condensation process. We then note that the terms $L/C_p\Delta T$ and τ_t/τ_{cond}, where $\tau_t = H/w$, are dimensionless numbers associated with the cloud condensation process. The time scale for condensation can be conceptually understood by considering the idealization of growth of a population of single-sized cloud droplets in a supersaturated environment. A cloud of droplets with radius R and number density N in an environment with mean supersaturation $\overline{s}$,

$$\dot{Q}_L = \frac{\rho_l}{\rho_a} \frac{d}{dt} \left(\frac{4\pi}{3} N R^3 \right) = \frac{\rho_l}{\rho_a} 4\pi N R^2 \frac{dR}{dt}, \tag{4.8}$$

where ρ_l is the density of water and ρ_a is the density of air. Using an expression [39]

for the droplet growth rate $d\overline{R}/dt$, equation 4.8 can be rewritten as

$$\dot{Q_L} \;=\; 4\pi\xi N R\,\overline{s}\,\frac{\rho_l}{\rho_a}. \tag{4.9}$$

Here ξ is a factor associated with thermal and vapor diffusion during the droplet growth[39]. Thus, the phase relaxation time (τ_c) can be understood as the timescale at which droplets respond to any change in its surrounding environment, defined as $\tau_c = (4\pi\xi N\overline{R})^{-1}$ [102]. Assuming the flux timescale, given by $\tau_t = H/w$, represents the scale at which the environment changes, the Damköhler number (Da) can be defined as τ_t/τ_c [24]. At very high Damköhler numbers, the droplets respond quickly to any change in the surrounding environment and conversely at small Damköhler numbers the environment changes faster than the droplets can respond to it. Hence, these regimes are called fast and slow microphysics respectively. Therefore, equation 4.7 can be rewritten as

$$\frac{\partial\tilde{T}}{\partial\tilde{t}} \;+\; \tilde{U}\cdot\tilde{\nabla}\tilde{T} \;=\; \frac{1}{\sqrt{Ra\,Pr}}\tilde{\nabla}^2\tilde{T} \;+\; \frac{1}{Ste}\,\frac{\rho_l}{\rho_a}\,Da\,\overline{s}. \tag{4.10}$$

We note that the expression on the right hand side consists of dimensionless quantities $Ste = C_p\Delta T/L$, ρ_l/ρ_a, Da and $\overline{s}$, where Ste is the Stefan number. Similarly, the equation for water vapor mixing ratio becomes

$$\frac{\partial\tilde{Q_v}}{\partial\tilde{t}} \;+\; \tilde{U}\cdot\tilde{\nabla}\tilde{Q_v} \;=\; \frac{1}{\sqrt{Ra\,Sc\,Le}}\tilde{\nabla}^2\tilde{Q_v} \;-\; \frac{1}{\Delta Q_v}\,\frac{\rho_l}{\rho_a}\,Da\,\overline{s}, \tag{4.11}$$

where Sc is the Schmidt number ($Sc = \nu/\nu_v$) and Le is the Lewis number($Le = Sc/Pr$). Using $\tilde{Q_L} = Q_L/\Delta Q_v$, the non dimensional form of liquid water mixing ratio (equation 4.6) is,

$$\frac{\partial \tilde{Q_L}}{\partial \tilde{t}} + \tilde{U} \cdot \tilde{\nabla} \tilde{Q_L} = Rou\ \tilde{Q_L} + \frac{1}{\Delta Q_v} \frac{\rho_l}{\rho_a}\ Da\, \overline{s}. \tag{4.12}$$

An additional dimensionless group appears, the ratio of the droplet terminal speed and the convection free-fall speed, which is sometimes referred to as the Rouse number $Rou = w_T/w$ [103, 104]. It is essentially a gravitational settling parameter or, it can be expressed as the inverse of a dimensionless droplet residence time τ_t/τ_{res}.

These dimensionless parameters appearing in these equations are summarized in Table 4.1. The parameters Pr, Sc, Le, Ste, and B_v describe material properties, so for a water-air system as in Earth clouds, they are essentially constants. Note that the water vapor contribution to buoyancy B_v can be considered a material property because, assuming saturated boundaries, the quantity $\Delta Q_v/\Delta T$ can be related to the Clausius-Clapeyron equation $dp_s/dT = L/(RT)$, where p_s is the saturation water vapor pressure; it is however a material property that depends on the mean temperature of the system. The dimensionless parameters that describe the cloud microphysical properties are s, Da, Rou, and B_L. It can be noted that B_L connects the microphysics directly to the buoyancy term in the Navier-Stokes equation, but in fact the phase changes described by s and Da also influence the buoyancy term through their

Dimensionless Number	**Definition**	**Description**
Ra	$g\beta\Delta T H^3/(\nu_T \nu)$	Buoyancy forcing and diffusive losses
B_v	$\epsilon \Delta Q_v/(\beta \Delta T)$	Relative contribution of water vapor to buoyancy
B_L	$Q_L/(\beta \Delta T)$	Relative contribution of cloud water to buoyancy
Pr	ν/ν_T	Diffusion of momentum relative to thermal energy
Sc	ν/ν_v	Diffusion of momentum relative to water vapor
Le	ν_T/ν_v	Diffusion of thermal energy relative to water vapor
Da	τ_t/τ_c	Rate of turbulent mixing relative to Rate of water vapor condensation in a cloud
s	$Q_v/Q_s(T) - 1$	Excess water vapor driving condensation
Ste	$C_p \Delta T/L$	Latent heat compared to sensible heat
Rou	w_t/w	Rate of removal of cloud droplets by sedimentation relative to rate of turbulent mixing
Nu_μ	Eqn. 4.21	Microphysics-independent energy flux relative to conductive flux

Table 4.1
Dimensionless parameters for the microphysical state in cloudy Rayleigh-Bénard convection.

contributions to the T and Q_v fields. Finally, the state of macroscopic convection is described by the dimensionless parameter Ra, as well as a Nusselt number Nu discussed in the next section.

4.3 Heat Flux and a Microphysics-Independent Nusselt Number

A defining aspect of convection is the efficient transfer of energy, which can be expressed through the dimensionless Nusselt number. Here we outline a simple route to obtaining a Nusselt number for cloudy convection and discuss its relationship to known variables of atmospheric thermodynamics and the relevance of cloud microphysical properties. We proceed initially with the dimensional forms of the equations for notational clarity.

Applying Reynolds decomposition, we write the instantaneous variable as a sum of the mean and the fluctuations represented by overbar and prime respectively,

$$U = \overline{U_i} + u_i'; T = \overline{T} + T'; Q_v = \overline{Q_v} + Q_v', \tag{4.13}$$

and it then follows from equations. (4.4) and (4.5) that the mean scalar evolution equations are

$$\frac{\partial \overline{T}}{\partial t} = \nabla \cdot \left(-\overline{U_i T} - \overline{u_i' T'} + \nu_T \nabla \overline{T}\right) + \frac{L}{C_p}\overline{\dot{Q}_L} \tag{4.14}$$

$$\frac{\partial \overline{Q_v}}{\partial t} = \nabla \cdot \left(-\overline{U_i Q_v} - \overline{u_i' Q_v'} + \nu_v \nabla \overline{Q_v}\right) - \overline{\dot{Q}_L}. \tag{4.15}$$

The two scalar equations can be combined together by eliminating the net condensation/evaporation rate $\overline{\dot{Q}_L}$ by adding equation. (4.14) and $L/C_p\times$ equation. (4.15):

$$\begin{aligned}\frac{\partial}{\partial t}\left(\overline{T}+\frac{L}{C_p}\overline{Q_v}\right) = \nabla\cdot\left(-\overline{U_i}\left(\overline{T}+\frac{L}{C_p}\overline{Q_v}\right)-\overline{u_i'\left(T'+\frac{L}{C_p}Q_v'\right)}\right)\\ +\nabla\cdot\nabla\left(\nu_T\,\overline{T}+\nu_v\,\frac{L}{C_p}\overline{Q_v}\right).\end{aligned} \tag{4.16}$$

Equation 4.16, steady in time and averaged over a plane with normal along the direction of gravity is

$$\nabla_z\cdot\left(-\overline{w'T'}+\nu_T\nabla_z\overline{T}\right)+\frac{L}{C_p}\nabla_z\cdot\left(-\overline{w'Q_v'}+\nu_v\nabla_z\overline{Q_v}\right)=0. \tag{4.17}$$

From equation. (4.17), a constant surface flux is obtained along the z-direction:

$$\Phi_\mu = \overline{w'T'}+\frac{L}{C_p}\overline{w'Q_v'}-\nu_T\nabla_z\overline{T}-\frac{L}{C_p}\,\nu_v\nabla_z\overline{Q_v}. \tag{4.18}$$

Thus, an effective Nusselt number can be defined as,

$$\mathrm{Nu}_\mu = \frac{\overline{w'T'}+\frac{L}{C_p}\overline{w'Q_v'}-\nu_T\nabla_z\overline{T}-\frac{L}{C_p}\,\nu_v\nabla_z\overline{Q_v}}{\nu_T\,\frac{\Delta T}{H}+\nu_v\,\frac{L}{C_p}\,\frac{\Delta Q_v}{H}}. \tag{4.19}$$

This microphysics independent flux (equation. 4.18) has been obtained from the temperature and water-vapor governing equations, independent of the rate and amount of condensation or evaporation occurring within the flow. It depends only on the temperature difference and water vapor difference imposed at the top and bottom

boundaries across the convecting system. We note that equation 4.19 is identical to the Nusselt number obtained by Zhang et al. [93] for moist convection without phase change, here we have demonstrated that it is useful for cases with phase change as well.

In fact, assuming temperature and water vapor to have the same diffusivities, the Nusselt number can be written solely in terms of the familiar atmospheric quantity 'equivalent temperature' (e.g., refer to equation 6.74, page 285 of Bohren and Albrecht [79]):

$$T_e = T + (L/C_p)Q_v. \tag{4.20}$$

The equivalent temperature is defined as the temperature to which air would rise if all its water vapor were to condense in an adiabatic, isobaric process. Such a process is allowed by the first law of thermodynamics, but it is prohibited by the second law of thermodynamics for a closed system [79]. This connection is discussed further in section 4.6.

Following the exact same steps but using the dimensionless forms of the governing equations, we get the flux (equation 4.18) in terms of non–dimensional quantities.

$$\tilde{\Phi}_\mu = \overline{\tilde{W}\cdot\left(\tilde{T}+\frac{L}{C_p}\frac{\Delta Q_v}{\Delta T}\tilde{Q}_v\right)} - \frac{1}{\sqrt{Ra}}\left(\frac{1}{\sqrt{Pr}}\tilde{\nabla}\tilde{T}+\frac{L}{C_p}\frac{\Delta Q_v}{\Delta T}\frac{1}{\sqrt{Sc\,Le}}\tilde{\nabla}\tilde{Q}_v\right)_z \tag{4.21}$$

The Nusselt number expressed in non-dimensional form would be

$$\mathrm{Nu}_\mu = \frac{\Phi_\mu}{\frac{L}{C_p}\frac{\Delta Q_v}{\Delta T}\frac{1}{\sqrt{Ra\,Sc\,Le}}\Delta\tilde{Q}_v+\frac{1}{\sqrt{Ra\,Pr}}\Delta\tilde{T}} \tag{4.22}$$

$$\mathrm{Nu}_\mu = \frac{\overline{\tilde{W}\cdot\left(\tilde{T}+\frac{L}{C_p}\frac{\Delta Q_v}{\Delta T}\tilde{Q}_v\right)}}{\frac{L}{C_p}\frac{\Delta Q_v}{\Delta T}\frac{1}{\sqrt{Ra\,Sc\,Le}}\Delta\tilde{Q}_v+\frac{1}{\sqrt{Ra\,Pr}}\Delta\tilde{T}} - \frac{\frac{1}{\sqrt{Ra}}\left(\frac{1}{\sqrt{Pr}}\tilde{\nabla}\tilde{T}+\frac{L}{C_p}\frac{\Delta Q_v}{\Delta T}\frac{1}{\sqrt{Sc\,Le}}\tilde{\nabla}\tilde{Q}_v\right)_z}{\frac{L}{C_p}\frac{\Delta Q_v}{\Delta T}\frac{1}{\sqrt{Ra\,Sc\,Le}}\Delta\tilde{Q}_v+\frac{1}{\sqrt{Ra\,Pr}}\Delta\tilde{T}} \tag{4.23}$$

From equations. 4.21 and 4.22, we note that the flux is independent of Damköhler

number and supersaturation, the two microphysically-relevant dimensionless parameters. Compared to the dry-convection Nusselt number, which depends on Ra and Pr, for cloudy convection the dimensionless parameters Sc and Le are also needed.

4.4 Numerical Simulations of Moist Rayleigh-Bénard Convection with Varying Cloud Microphysics

In this section, we explore the microphysics-independent flux and the equivalent temperature derived in Section 4.2.2 by simulating moist Rayleigh-Bénard convection under varying microphysical conditions. The simulations are motivated by prior observations from and simulations of the Pi convection-cloud chamber [24, 41, 94]. The convection is initiated by imposing an unstable gradient of temperature and water vapor between the top and bottom plates. The bottom and top plates are maintained at saturated conditions at 290 K and 276 K respectively. The four sidewalls have adiabatic conditions for both temperature and water vapor mixing ratio, and a no slip condition for velocity. The different aerosol injection rates used in the current study are listed in Table 4.2, with a cloud-free case included for reference. Corresponding steady-state microphysical properties including the liquid water mixing ratio, the

cloud droplet number concentration, mean diameter, and water vapor supersaturation are also listed in Table 4.2. These conditions are chosen such that significant supersaturations and cloud droplet removal by sedimentation are observed. The existence of non-zero supersaturation implies that the cloud is not in an equilibrium state, and the condensation process is therefore irreversible. As the aerosol injection rate is increased, the cloud droplet number concentration increases and the mean diameter decreases. We also observe an increase in the liquid water content as the aerosol injection rate is increased, because smaller cloud droplets have lower sedimentation rates.

Reference	Injection Rate (s^{-1})	Q_L (g/kg)	N (cm^{-3})	$\bar{R}\,(\mu m)$	s (%)	Rou	Da
A	3.26	0.054	5.9	10.49	2.721	0.115	0.064
B	9.78	0.109	30.61	7.77	0.7279	0.073	0.252
C	72.88	0.252	403.98	4.42	0.0239	0.029	1.857
D	158.5	0.292	692.41	3.92	0.0054	0.029	2.801
E	115.69	0.321	990.17	3.60	0.0026	0.019	3.658
F	317.00	0.384	2253.01	2.95	0.0004	0.012	6.733
G	425.50	0.416	3520.20	2.63	0.0002	0.008	9.328

Table 4.2

Varying microphysical conditions explored in the simulations of moist Rayleigh-Bénard convection. The table shows aerosol (cloud condensation nucleus) injection rate, liquid water mixing ratio, cloud droplet number concentration, mean cloud droplet radius and steady state supersaturation.

Details of the model setup for the Pi convection-cloud chamber are discussed in Thomas et al. [41]. A brief description of the model is provided here for sake of completeness. The simulations use the modified System for Atmospheric Modeling (SAM) [70] combined with a spectral bin microphysics (SBM) model[105]. The System for Atmospheric Modeling is a large eddy simulation (LES) code that solves the equations of motion under the anelastic approximation, and that uses a Smagorinsky model for the subgrid-scales. The equations are integrated using a third-order Adams-Bashforth scheme on a fully staggered Arakawa C-type grid with uniform horizontal and vertical grid sizes. The prognostic scalars are advected using a multidimensional positive definite advection transport algorithm [71]. Boundary fluxes are calculated using Monin-Obukhov similarity theory.

Aerosol-cloud interactions in SAM are simulated using SBM. The SBM model involves aerosols and water droplets with size distributions represented in 33 mass-doubling bins. The model accounts for relevant microphysical processes and interactions, such as activation of cloud droplets, diffusion growth or evaporation of droplets, drop collisions, turbulence effects on collisions, and collisional breakup. The present study focuses only on warm clouds with droplet activation and diffusional growth, and the effects of collisional growth are turned off.

We consider a convection chamber of dimensions 2 m $\times$ 2 m $\times$ 1 m along the x, y and z directions respectively. The computational domain is discretized uniformly with

cubic boxes of side length 3.125 cm yielding $64 \times 64 \times 32$ grid boxes. The time step is 0.02 s, and the system is initialized with an unstable temperature and water vapor gradient. For the current study, we allow the system to evolve in a cloud-free state and reach a steady supersaturation of 10.5% ($\Delta T = 14K$, $T_{mean} = 283.15K$), after which we inject a single size of cloud condensation nuclei (CCN), corresponding to the bin centered at 62.5 nm, injected uniformly in the volume of the chamber. The cloud reaches a steady state after about an hour of simulated time by reaching a balance between droplet activation and removal due to sedimentation. On reaching a steady state with respect to microphysics after 1 hour, the system is allowed to evolve for another 2 hours.

After one hour of physical time, 3D fields are output at every five minutes for the next three hours to obtain statistically independent droplet size distributions within the simulated cloud chamber (this time is chosen so as to be larger than the large-scale circulation time so as to ensure independence). Each grid point thus has a cloud droplet number concentration sorted into 33 different bins according to their sizes. The fluxes are evaluated from 3D fields of velocity u, v, w, temperature, water vapor and liquid water mixing ratio.

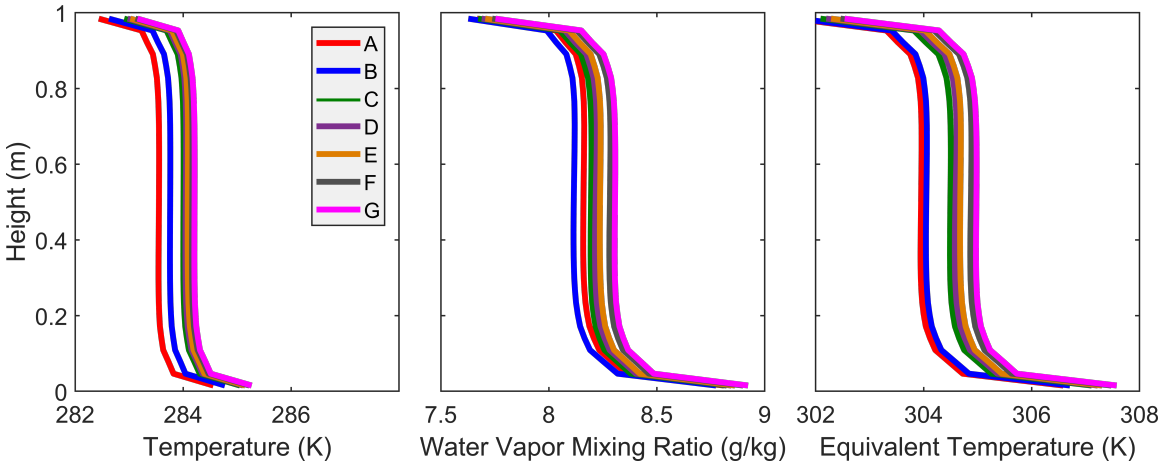

Figure 4.1: Averaged profiles of (a) temperature, (b) water vapor and (c) equivalent temperature. These profiles were obtained by horizontal averaging of the 3D output obtained every 5 minutes within a span of 2 hours, after reaching a steady state. Each color refers to different CCN injection rates; for details refer to Table 4.2.

4.5 Results: LES of Cloudy Convection with Varying Microphysics

4.5.1 Vertical profiles of scalars

Figure 4.1 shows vertical profiles of temporal and area (horizontal) averaged temperature, water vapor mixing ratio and total water content for the different aerosol injection rates. The injection of aerosols into the supersaturated system described in section 4.4 results in the formation of cloud droplets. The liquid water content

in the chamber reaches a steady state through a dynamic equilibrium between condensational growth and gravitational sedimentation. As shown already in Table 4.2, and as observed in both experiments and prior simulations [24, 41], increasing the aerosol injection rate results in a corresponding increase in the steady-state liquid water content in the cloudy Rayleigh Bénard convection system. The condensation rate is proportional to $N_d \overline{D}$, where N_d is the number concentration of droplets and $\overline{D}$ is the mean droplet diameter, and therefore increases with aerosol injection rate. That leads to a reduction of the mean water vapor mixing ratio as shown in figure 4.1(b) and an increase in the bulk temperature due to enthalpy change associated with condensation Fig 4.1(a). This reduction in the mean water vapor mixing ratio and increase in the mean temperature result in a much lower supersaturation for cloudy conditions compared to moist conditions without any aerosols. Therefore, as evident from Table 4.2, the mean bulk supersaturation shift towards zero as the number concentration and liquid water content increase. We observe a monotonous increase of equivalent temperature in Fig 4.1(c) with increasing cloud droplet number concentration. From a parcel point of view, one would expect the equivalent temperature to be a constant for a given total water content. However, the total water content inside the cloud chamber is not a constant. As the number of cloud droplets increase, the droplet radius decreases increasing the droplet lifetime. Thus, with a reduced the precipitation efficiency, the total water content and consequently the equivalent temperature increases.

4.5.2 Sensible heat flux, latent heat flux and microphysics-independent flux

The sensible heat flux (SHF), latent heat flux (LHF) and microphysics-independent flux defined in equation (4.18) are plotted in figure 4.2. The boundary flux contributions are discussed later, and only the turbulent fluxes are considered in this figure. In the bulk, the turbulent transport terms for scalars are of the form, $\overline{u_i'\phi'}$, where ϕ' is the fluctuation component of a scalar. The turbulent sensible heat flux and latent heat flux at any height z are given by:

$$SHF_{turbulent} = \rho_z \, C_p \langle \overline{u_k' T'} \rangle_z \tag{4.24}$$

$$LHF_{turbulent} = \rho_z \, L_w \langle \overline{u_k' Q_v'} \rangle_z. \tag{4.25}$$

The height-dependent density ρ_z has to be multiplied to account for non-Oberbeck–Boussinesq (NOB) effects associated with strong temperature gradients. Again, the SGS fluxes and boundary contributions are not considered here, therefore these equations are applied along the height of the chamber to generate figure 4.2. The variability inherent in the turbulent flow is shown with uncertainty bars obtained from the standard deviation of the average values of 12 samples, with each sample representing a 10-minute average (roughly 10 large-scale circulation times). The averaged microphysics-independent flux, as predicted, remains relatively constant

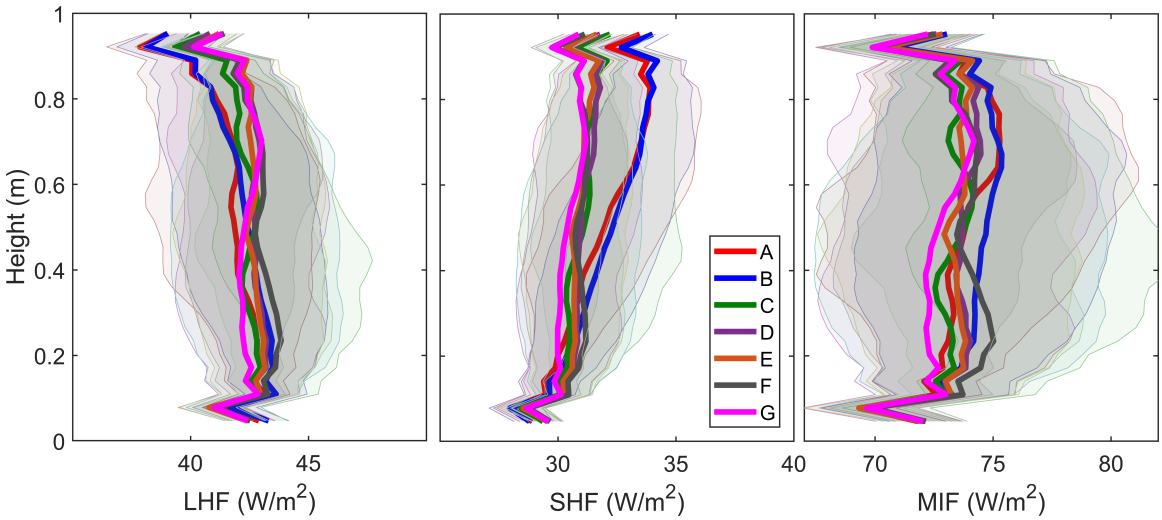

Figure 4.2: Time averaged profiles of (a) SHF ($\rho\, C_p\, \overline{w'T'}$), (b) LHF ($\rho\, L_w\, \overline{w'Q_v'}$) and (c) microphysics independent flux (MIF) from 3D outputs sampled at a frequency of 5 minutes for 2 hours. The shaded region shows the turbulent variability in the data. The line colors refer to the different CCN injection rates, as defined in Table 4.2.

compared to SHF and LHF under different aerosol injection rates. Specifically, the sensible and latent heat flux profiles are increasingly sloped as aerosol injection rate increases, and the curves lie outside the turbulent variability envelopes near the top and bottom boundaries. The microphysics-independent fluxes calculated for different aerosol injection rates, however, fall within the inherent turbulent variability.

The profiles of SHF [figure 4.2(a)] and LHF [figure 4.2(b)] can be interpreted by considering the governing equations for temperature and water vapor in the presence of cloud droplets:

$$\frac{\partial T}{\partial t} = \nabla \cdot (-U_i T + \nu_T \nabla T) + \frac{L_w}{C_p} \dot{Q}_L \tag{4.26}$$

$$\frac{\partial Q_v}{\partial t} = \nabla \cdot (-U_i Q_v + \nu_v \nabla Q_v) - \dot{Q_L} \tag{4.27}$$

For a steady state system the left sides of Eqs. (4.26) and (4.27) are zero. On applying Reynolds decomposition and horizontal area averaging, the first term in $C_p\times$ equation (4.26) is the sensible heat flux $C_p\left(\overline{w'T'} - \nu_T \nabla_z \overline{T}\right)$, and the first term in $L_w\times$ equation (4.27) is the latent heat flux $L_w\left(\overline{w'Q_v'} - \nu_v \nabla_z \overline{Q_v}\right)$. Under these assumptions, $C_p\times$ equation (4.26) and $L_w\times$ equation (4.27) can be written as

$$\frac{d\left(\overline{SHF}\right)}{dz} = L_w \overline{\dot{Q}_L} \tag{4.28}$$

$$\frac{d\left(\overline{LHF}\right)}{dz} = -L_w \overline{\dot{Q}_L} \tag{4.29}$$

From equation (4.28) and equation (4.29) it is clear that a net condensation rate results in vertical gradients of SHF and LHF, and that horizontally-averaged vertical profiles of SHF and LHF have opposite slopes as demonstrated in low cloud droplet number cases A, B, and C in figure 4.2. However, as the number of cloud droplets in the bulk increases the supersaturation approaches water vapor saturation (refer Table 4.2). In such cases, any supersaturation is produced at the boundaries due to the mixing of plumes from the boundary with the bulk parcels thus localizing any condensation predominantly to the boundaries. Therefore, the slope of SHF and LHF in the bulk of the chamber, characterizing the condensation rate, reduces as shown by the SHF and LHF profiles of cases D, E, F, and G in figure 4.2. From the theoretical

derivation, we expect the MIF to remain a constant along the height of the chamber. From the LES simulations, we notice from panel (c) of figure 4.2, MIF remains within the turbulent variability for different cloud droplet number cases.

4.6 Discussion

The theoretical analysis and results presented so far confirm that the effective heat flux in a cloudy convection is conserved, and is independent of the rate of condensation/evaporation in the fluid from the LES simulations. Additionally, the theoretical analysis also shows that the effective flux is independent of the nature of the nucleation: heterogeneous (aided by aerosols - current study) or homogeneous ([106]). The effective heat flux is only a function of Ra, Pr, Sc and Le. The fact that the effective heat flux is independent of the form of phase change aids in generalizing the present work to any form of phase change in the bulk. This would indicate that convective system with a heat source/sink in the core of the flow, similar to effects of a first order phase transition, will have an effective heat flux similar to the one in equation (4.18).

Let us consider the simple case of a boiling system [107]. A similar formulation is applicable in the context of a two-phase boiling convection system (e.g. boiling of water), where the roles of vapor and liquid is reversed with reference to the current study. The latent heat of condensation is replaced with the latent heat of vaporization

in the corresponding temperature, i.e., the sign of the phase change term in the temperature, water vapor and liquid water equation is reversed. Furthermore, the rate of boiling in the bulk of the fluid will depend on the number concentration of the bubbles and their total surface area, similar to the observations discussed in Section 4.5. Thus, the net heat flux in a boiling convective system will have the exact form as Equation 4.18, with the latent heat of condensation replaced by the latent heat of fusion/vaporization.

Additionally, this analysis can be extended to chemically reacting systems, where the heat release/absorption associated with the reaction is analogous to the latent heat of condensation/evaporation in a cloudy system. The idea of Damköhler number discussed in the present work is borrowed from studies involving chemically reacting systems, and is used for identifying slow, moderate and fast reaction with respect to the flow timescale [108]. Thus, a chemically reacting system is analogous to a cloudy convection system, and will have an effective heat flux that will be independent of the Damköhler number.

The discussion so far suggests that in a convection system, the heat released/absorbed in the bulk of the fluid due to phase change effects or chemical reactions does not influence the effective flux, which is dependent only on the boundary contributions. Thus, this flux (in the limit when $Sc = Pr$) is conserved and could be used for identifying the effects of non-conservative contributions to the flow, for e.g., entrainment

effects in a cloudy boundary layer flow (see the sub-section on atmospheric implications for additional details), evaporating jets, etc.. Additionally, the properties of the effective flux is applicable in the context of extrasolar planetary atmosphere that have cloud systems composed of fluids with properties very different from that of water [106, 109].

Finally, the equivalent potential temperature is defined as the temperature attained by a parcel of air when all the water vapor content is converted to liquid water by raising the parcel from the surface to infinity :

$$\theta_e = \theta \exp(L_w Q_v / C_p T) \approx \theta + L_w Q_v / C_p. \tag{4.30}$$

Further, it should also be noted that this derivation assumes the entropy change to be zero. Multiplying equation 4.30 with C_p, gives another familiar atmospheric quantity, the moist static energy $S_e = C_p\, T + g\, z + L_w\, Q_v$. The moist static energy is obtained from the first law and is essentially equivalent to the enthalpy [110]. It has been widely used to study the energy budget in deep convective clouds as well as the response of clouds to entrainment [111, 112, 113, 114].

4.7 Summary and Outlook

In Section 4.2.2, we have derived a flux independent of microphysics that is conserved with the height of the chamber. Over the range of the microphysics explored here, we also observe that the flux is independent of microphysics. Subsequently, we expand the definition of Nusselt number derived by Zhang et al[93] to include the effect of cloud microphysics as well. Further, by non dimensionalizing equations of temperature and water vapor mixing ratio, we identify Damköhler number, Schmidt number, Prandtl number and Lewis number are relevant for cloudy Rayleigh Bénard convection cases, in addition to the traditional Rayleigh number and Prandtl number for dry Rayleigh Bénard cases.

In Section 4.5 we demonstrate that the microphysics independent flux remains a constant for different aerosol injection cases explored using an atmospheric LES modified to simulate cloudy Rayleigh Bénard processes. One of the caveats associated with atmospheric models is that they assume the same turbulent diffusivities for temperature and water vapor in the LES. We demonstrate the increase in latent heat flux and a commensurate decrease in the sensible heat flux from bottom surface resulting in a constant heat flux for different cloud droplet number cases. Further, we explain the profiles of latent heat flux and sensible heat flux within the chamber as a function of the condensation rate within the bulk of the Rayleigh-Bénard convection flow.

Finally in Section 4.6, we explore the possibility of using fluxes analogous to microphysical independent flux for other phase change systems such as boiling convection systems and for chemically reacting systems. Further, we connect the microphysical independent flux to the atmospheric context - in terms of equivalent temperature, equivalent potential temperature and moist static energy.

Ideally, investigations using direct numerical simulations with point particles would allow for a more detailed investigation on the conservation of the microphysics independent flux. Thus a parameters space varying $Ra\,, Pr\,, Sc\,, Da$ can be explored from a fluid dynamics perspective and from an atmospheric context, the effect of roughness and surface flux parameterizations needs to be explored thoroughly. Thus the microphysics independent flux can lead to the development of improved parameterizations of heat and mass fluxes for cloudy convection.

Chapter 5

Is the water vapor supersaturation distribution Gaussian?

"It is by logic that we prove, but by intuition that we discover."

- Henri Poincaré

This chapter is about the mixing supersaturation PDFs. It is based on a collaborative research published in the Journal of Atmospheric Sciences.[1].

[1]An edited version of the paper is published by AMS[115]

Abstract

Water vapor supersaturation in the atmosphere is produced in a variety of ways, including the lifting of a parcel or via isobaric mixing of parcels. However, irrespective of the mechanism of production, the water vapor supersaturation in the atmosphere has typically been modeled as a Gaussian distribution. In the current theoretical and numerical study, the nature of supersaturation produced by mixing processes is explored. The results from large eddy simulation and a Gaussian mixing model reveal the distribution of supersaturations produced by mixing to be negatively skewed. Further, the causes of skewness are explored using large eddy simulations and the Gaussian mixing model. The correlation in forcing of temperature and water vapor fields is recognized as playing a key role.

5.1 Introduction

According to Köhler theory, cloud microphysical processes such as activation, deactivation and growth of cloud particles depend on the mean thermodynamic properties of the environment surrounding the particle [39]. These thermodynamic properties are determined by the temperature and water vapor content present in the system. Cloud particles respond to any non-equilibrium conditions present in the cloud system by

condensational growth or evaporation according to the Le Chatelier's principle [102]. In a thermodynamically stable two-phase system, the water vapor pressure dynamically balances the condensation and evaporation fluxes over a flat, pure water surface at temperature T. This vapor pressure is called the saturation vapor pressure and is given by the Clausius–Clapeyron equation. Any excess/deficit of vapor pressure leads to non-equilibrium conditions, and is quantitatively expressed by supersaturation (s), and is given by,

$$s = \frac{q_v}{q_{sat}(T)} - 1 \tag{5.1}$$

Please refer to Appendix A for variable definitions.

The study described in [116] theoretically explored the implications of turbulent fluctuations on droplet size distributions, and recent experimental [23, 24, 40] , field [82, 117, 118, 119] and numerical [1, 2, 36, 120, 121, 122, 123, 124] studies have demonstrated the importance of scalar fluctuations caused by turbulence on activation, condensational growth and deactivation processes for aerosol and cloud particles, in addition to the mean supersaturation [39, 44]. Thus, an accurate representation of the supersaturation variability is required to capture the cloud microphysics effects [125].

In modeling studies, if supersaturation is treated as a random variable at all, its probability density function (PDF) is usually treated as Gaussian [2, 43, 123], similar to scalars like temperature and water vapor mixing ratio. However, the supersaturation

PDF is dependent on the process by which supersaturation is produced. In a parcel view of the atmospheric clouds, supersaturation can be produced by the vertical ascent of parcels [39] and by the isobaric mixing of parcels [126]. Cloud entrainment [127, 128] and cloud–free Rayleigh-Bénard convection [2, 3, 93] are examples of processes that can produce supersaturation via isobaric mixing, occurring both in nature and in the laboratory. For the current study, we focus on supersaturation generated via mixing processes, and cloud–free Rayleigh-Bénard convection (RBC) is an ideal surrogate for such processes. RBC can be considered the simplest model of the subgrid-scale mixing within a typical cloud Large Eddy Simulation(LES), for example. It is further advantageous because it efficiently produces a statistically stationary thermodynamic state corresponding to the mixing processes. Furthermore, an atmospheric LES model can be modified to simulate cloud–free RBC to exclusively study mixing processes without any complexities and uncertainties involving cloud-supersaturation feedback interactions and boundary forcings. This model not only serves as the test bed to reveal insights into the nature of supersaturation PDF produced by mixing processes in the absence of cloud droplets, but also helps in validating a computationally inexpensive Gaussian mixing model introduced here.

In this study, we investigate the shape of the supersaturation PDF in the context of atmospheric mixing processes in the absence of cloud droplets using an atmospheric LES and a Gaussian mixing model(GMM) detailed in section 5.3. The results are presented in section 5.4 and atmospheric implications are discussed further in section

5.5.

5.2 Theory

Scalar equations

We begin by considering the origin of supersaturation fluctuations. The advection–diffusion equation of scalars with external large scale forcing required to sustain the fluctuations is given by

$$\frac{\partial T}{\partial t} = \nabla \cdot (-\mathbf{U}\, T + \alpha \nabla T) + \frac{L_v}{C_p}\dot{q}_l + f_T \tag{5.2}$$

$$\frac{\partial q_v}{\partial t} = \nabla \cdot (-\mathbf{U}\, q_v + \nu_v \nabla q_v) - \dot{q}_l + f_q \tag{5.3}$$

Consider Eq. 5.2; the rate of change of temperature at a point depends on the temperature advected by the fluid motion, the diffusional heat transfer due to local gradients, rate of release/absorption of latent heat due to condensation/evaporation and finally any external forcing. Similarly in Eq. 5.3, for water vapor, all the terms on the right hand side are analogous to Eq. 5.2 except for the latent heat effects term which is replaced by rate of condensation/evaporation of water vapor. Note that we have used

temperature (T) instead of pressure compensated potential temperature because isobaric mixing assumes the process to be local in nature. For parcel studies such as [122], f_T & f_q represent the change in forcing of temperature and water vapor due to the entrainment of surrounding environmental air into the parcel.

From Eqs. 5.2 and 5.3 we gather that for a given flow field, the difference between appropriately normalized temperature and water vapor fields at a location can arise only from one of the following scenarios: (i) differential diffusivity of scalars, (ii) condensation/evaporation processes and (iii) correlation between f_T & f_q.

In the absence of cloud droplets for a RBC system in steady state, the bulk mean temperature ($\overline{T}$) and water vapor ($\overline{q_v}$) are given by

$$\overline{T} = \frac{\rho_t\, T_t \,+\, \rho_b\, T_b}{\rho_t \,+\, \rho_b} \tag{5.4}$$

$$\overline{q_v} = \frac{\rho_t\, q_{vt} \,+\, \rho_b\, q_{vb}}{\rho_t \,+\, \rho_b}. \tag{5.5}$$

In this context, *bulk* refers to the region of fluid sufficiently far away ($\sim$ 12.5cm) from the boundaries. Without considering the effects of turbulence, at a given pressure, the mean supersaturation expressed in mixing ratios is given by

$$\overline{s} \;=\; \frac{\overline{q_v}}{q_{sat}(\overline{T})} - 1 \tag{5.6}$$

For a turbulent flow, [36] derived the supersaturation mean and variance to be

Eq. (5.7) and (5.8) respectively:

$$\begin{aligned}\overline{s} = & \frac{\overline{q_v}}{q_{sat}(\overline{T})}\Bigg\{1 - \frac{L_v}{R_v\overline{T}}\frac{\overline{q_v'T'}}{\overline{q_v}\,\overline{T}} + \\ & \left[\frac{1}{2}\left(\frac{L_v}{R_v\overline{T}}\right)^2\frac{\overline{T'^2}}{\overline{T}^2} + \frac{L_v}{R_v\overline{T}}\frac{\overline{T'^2}}{\overline{T}^2}\right]\Bigg\} - 1\end{aligned} \tag{5.7}$$

$$\begin{aligned}\sigma_s^2 = & \left(\frac{\overline{q_v}}{q_{sat}(\overline{T})}\right)^2\Bigg\{\frac{\overline{q_v'^2}}{\overline{q_v}^2} - 2\frac{L}{R_v\overline{T}}\frac{\overline{q_v'T'}}{\overline{q_v}\,\overline{T}} + \\ & \left(\frac{L_v}{R_v\overline{T}}\right)^2\frac{\overline{T'^2}}{\overline{T}^2}\Bigg\}.\end{aligned} \tag{5.8}$$

For random variables x and y, the ensemble mean is represented as $\overline{x}$, any fluctuations from the mean by prime x' and co–variance terms by $\overline{x'y'}$.

To understand the role of turbulence on the mean supersaturation, one can subtract Eq. 5.6 from Eq. 5.7. The coefficient of terms with $(T'/\overline{T})^2$ is always positive and hence tends to increase the mean supersaturation. On the other hand, the coefficient of the co-variance term $\overline{q_v'T'}$ is negative, hence its effect on mean supersaturation depends on the sign of the covariance term. In the subsequent sub-section we explore the factors affecting $\overline{q_v'T'}$.

Discussions on the water vapor temperature co-variance

On applying Reynolds decomposition for temperature and water vapor (e.g., refer to chapters 3 and 4 of [129]) by separating into mean and fluctuation components and

subtracting the mean equations, we get the evolution equation for temperature and water vapor fluctuations:

$$\frac{\partial T'}{\partial t} = \nabla \cdot \left(-\overline{\mathbf{U}}\, T' - \mathbf{U}'\, \overline{T} + \alpha \nabla T' - \overline{\mathbf{U}' T'}\right) + \frac{L_v}{C_p}\dot{q_l'} + f_T \tag{5.9}$$

$$\frac{\partial q_v'}{\partial t} = \nabla \cdot \left(-\overline{\mathbf{U}}\, q_v' - \mathbf{U}'\, \overline{q_v} + \nu_v \nabla q_v' - \overline{\mathbf{U}' q_v'}\right) - \dot{q_l'} + f_q. \tag{5.10}$$

To derive the evolution equation for $\overline{q_v' T'}$, we multiply Eq. 5.9 with q_v' and Eq. 5.10 with T'

$$\begin{aligned} q_v' \frac{\partial T'}{\partial t} &= q_v' \nabla \cdot \left(-\overline{\mathbf{U}}\, T' - \mathbf{U}'\, \overline{T} + \alpha \nabla T' - \overline{\mathbf{U}' T'}\right) \\ &\quad + \frac{L_v}{C_p} q_v' \dot{q_l'} + q_v' f_T \end{aligned} \tag{5.11}$$

$$\begin{aligned} T' \frac{\partial q_v'}{\partial t} &= T' \nabla \cdot \left(-\overline{\mathbf{U}}\, q_v' - \mathbf{U}'\, \overline{q_v} + \nu_v \nabla q_v' - \overline{\mathbf{U}' q_v'}\right) \\ &\quad - T' \dot{q_l'} + T' f_q. \end{aligned} \tag{5.12}$$

Summing Eqs. 5.11 and 5.12 we obtain

$$\begin{aligned} \frac{\partial q_v' T'}{\partial t} &= -q_v' \nabla \cdot \left(-\overline{\mathbf{U}}\, T' - \mathbf{U}'\, \overline{T} + \alpha \nabla T' - \overline{\mathbf{U}' T'}\right) \\ &\quad - T' \nabla \cdot \left(-\overline{\mathbf{U}}\, q_v' - \mathbf{U}'\, \overline{q_v} + \nu_v \nabla q_v' - \overline{\mathbf{U}' q_v'}\right) \\ &\quad + \frac{L_v}{C_p} q_v' \dot{q_l'} - T' \dot{q_l'} + q_v' f_T + T' f_q. \end{aligned} \tag{5.13}$$

The time evolution of $\overline{q_v' T'}$ is obtained by averaging Eq. 5.13

$$\begin{aligned}
&\frac{\partial \overline{q_v' T'}}{\partial t} + \overline{\mathbf{U}} \cdot \nabla \left(\overline{q_v' T'} \right) \; + \; \overline{\mathbf{U}' \cdot \nabla \left(q_v' T' \right)} + \\
&\qquad \overline{\mathbf{U}' T'} \cdot \nabla \left(\overline{q_v} \right) \; + \; \overline{\mathbf{U}' q_v'} \cdot \nabla \left(\overline{T} \right) \; = \\
&\qquad \nu_v \nabla^2 \left(\overline{q_v' T'} \right) \; - \nu_v \, 2 \left(\overline{\nabla q_v' \nabla T'} \right) + (Le - 1) \; \nu_v \, \overline{q_v' \nabla^2 T} \\
&\qquad + \frac{L}{C_p} \overline{\dot{q}_l' q_v'} - \overline{\dot{q}_l' T'} + \overline{T' f_q} + \overline{q_v' f_T}.
\end{aligned} \tag{5.14}$$

In Eq. 5.14, the first term on the left hand side is the time evolution of $\overline{q_v' T'}$, while the second and the third terms represent advective transport by mean and fluctuating components of the flow. The fourth and fifth terms on the left hand side are the two sources for production of $\overline{q_v' T'}$ due to the presence of a mean gradient in temperature and water vapor. The interpretation of the right hand side of Eq. 5.14, is complicated due to the production of local gradients in temperature and water vapor due to phase change processes.

For the ease of interpretation, let us assume a case in the absence of droplets and external forcing. Therefore, terms with $\dot{q}_l{}'$ disappear from the right hand side of Eq. 5.14 and only the diffusive terms are retained. For such a case the right hand side can be rewritten as

$$\nu_v \nabla^2 \left(\overline{q_v' T'} \right) - \nu_v \, 2 \left(\overline{\nabla q_v' \nabla T'} \right) + (Le \; - \; 1) \, \nu_v \, \overline{q_v' \nabla^2 T}, \tag{5.15}$$

where $Le = \alpha/\nu_v$ is the Lewis number. These terms on the right hand side of Eq. 5.15 can be interpreted as follows: the first term is the diffusive transport of $\overline{q_v' T'}$ and the second term is the dissipation term since $\overline{\nabla q_v' \nabla T'}$ is positive definite since both scalars behave identically in the flow field. The third term is relevant for cases with differential diffusivity, $Le \neq 1$. The effects of differential diffusivity make the interpretation of the term difficult without a fully resolved study. It should be noted that these effects are significant only at diffusive length scales.

To evaluate the phase change effects, consider a system with temperature and water vapor transported only by advection processes but including condensation effects. In such a case, any local condensation results in the depletion of water vapor and increase in temperature and vice versa for any local evaporation. Therefore, $\overline{\dot{q}_l' q_v'} - \overline{\dot{q}_l' T'}$ would always be negative and hence acts as a sink term for $\overline{q_v' T'}$. However, in physical systems phase change events produce local gradients of temperature and water vapor, resulting in interactions of all terms on the right hand side of Eq. 5.14. Strictly speaking, these processes can only be disentangled through particle-resolved simulations of the turbulent flow, i.e., even beyond direct numerical simulation of turbulence, down to the temperature and vapor gradients existing at particle scales. Here, we will focus primarily on the supersaturation PDF without cloud droplet growth.

The production terms $\overline{\mathbf{U}' T'} \cdot \nabla \overline{q_v}$ and $\overline{\mathbf{U}' q_v'} \cdot \nabla \overline{T}$ in Eq. 5.14 are active only close to

the boundaries where $\nabla\overline{T}$ and $\nabla\overline{q_v}$ are significant. The terms $\overline{\mathbf{U}'T'}$ and $\overline{\mathbf{U}'q_v'}$ at these boundaries are generally modeled using Monin-Obukhov similarity theory. The diffusive terms in atmospheric models are modeled using sub-grid scale parameterizations. Finally, the rate of condensation depends on the microphysical parameterization. It should be noted that the time rate of change of $\overline{q_v'T'}$ depends entirely on the level of approximation with reality by Monin-Obukhov similarity theory, subgrid-scale parameterization of diffusivity and microphysics.

5.3 Analysis Tools

In this paper, we use two computational approaches to explore supersaturation fluctuations in a turbulent Rayleigh-Bénard convection flow. First, we describe a detailed Large Eddy Simulation approach, and second, we introduce an idealized Gaussian mixing model based on observed behavior of scalar fields from measurements and numerical studies of Rayleigh-Bénard convection. The latter model also can explore the effect of differential diffusivity, forcings of temperature and water vapor and their correlations on the supersaturation PDF.

5.3.1 Large Eddy Simulation

The System for Atmospheric Modeling (SAM) [70] coupled with Hebrew University Spectral Bin Microphysics [65, 74] is configured to simulate the Michigan Tech Pi Cloud Chamber as described in [41]. We provide a brief discussion of the model for completeness. The RBC system is a $2\,m \times 2\,m \times 1\,m$ box modeled as $64 \times 64 \times 32$ grid points with a grid size of $3.125\,cm$. The convective system is initialized by imposing an unstable temperature gradient and water vapor mixing ratio gradient along the height of the chamber, keeping the top and bottom boundaries saturated. Furthermore, adiabatic conditions for temperature and water vapor mixing ratio are imposed for the sidewalls. Once initialized, the system is allowed to evolve for 2 hours of physical time and the simulation reaches a stationary state in 20 minutes. The results from the last 1 hour of the simulation are used for the analysis presented here.

5.3.2 Gaussian Mixing Model

The isobaric mixing process in a turbulent cloud–free RBC system is emulated using a Gaussian mixing model. In the model, the PDFs of temperature and water vapor are assumed to be Gaussian in nature, as is observed for the bulk fluid in turbulent RBC ([35, 130] and references therein). The mean for temperature and water vapor

are given by Eqs. 5.4 and 5.5. The standard deviation required for the description of a Gaussian PDF in RBC is given by equations 3.6 and 3.7 from [3] and can be rewritten as

$$\sigma_T^* \;=\; C^{-1/2}\, Ra_m^{-1/6} \left(\frac{z}{H}\right)^{-1/2} \tag{5.16}$$

$$\sigma_{q_v}^* \;=\; C^{-1/2}\, Ra_m^{-1/6}\, Sc^{-1/2}\, Pr^{1/2} \left(\frac{z}{H}\right)^{-1/2}, \tag{5.17}$$

with

$$\sigma_T^* \;\equiv \sigma_T \Delta T^{-1}$$

$$\sigma_{q_v}^* \;\equiv \sigma_{q_v} \Delta q_v^{-1}$$

$$C = \kappa \times {C_1}^{-2}.$$

Here, Ra_m is the ratio of time–scale for transportation via diffusion to convection, Pr is the ratio of momentum diffusivity to thermal diffusivity, Sc is the ratio of momentum to vapor diffusivity and Le is the ratio of thermal diffusivity to vapor diffusivity or Sc/Pr. The procedure for calculating C is described next. For a given temperature difference, the mean and standard deviation of temperature are obtained at the mid-plane ($z = H/2$) of the RBC cell using LES. From Eqs. 5.16 and 5.17, C is calculated after setting Pr equal to Sc since the effects of differential diffusivity are not captured in the current LES model.C has a mean value of 3.378 and standard deviation of 0.51 from the 4 LES simulations. In the absence of any trend, for the subsequent calculations, C is assumed to be a constant 3.378. A Gaussian profile is

assumed for the temperature and water vapor, with the mean values calculated using Eqs. 5.4 and 5.5. Thus a single realization of random variables – temperature and water vapor mixing ratio, is obtained by the following expression.

$$T = \overline{T} + \sigma_T \mathcal{N}_T(0,1) \tag{5.18}$$

$$q_v = \overline{q_v} + \sigma_{q_v} \mathcal{N}_{q_v}(0,1). \tag{5.19}$$

Here, $\mathcal{N}_T(0,1)$ and $\mathcal{N}_{q_v}(0,1)$ are normally distributed Gaussian random numbers with zero mean and unit variance. Generally, $\mathcal{N}_T$ and $\mathcal{N}_{q_v}$ need not be correlated, however for physical systems one can expect a certain level of correlation between the temperature and water vapor scalars. From LES results, we find this correlation coefficient to be 0.9994. We use Cholesky decomposition of the T–q_v co-variance matrix to generate a lower triangular matrix and its transpose, and further we use the resulting lower triangular matrix to create any desired correlation coefficient between the temperature and water vapor scalars.

Figure 5.1 shows the supersaturation PDFs of four cases with temperature differences of 8 K, 10 K, 14 K and 18 K. The solid line shows the data obtained from LES at the mid plane of the chamber, at least 12.5 cm away from the sidewalls. The dashed lines are the results from the GMM model with correlation coefficient between T – q_v to be 0.9994 and the constant C set to 3.378. We notice the shapes of the PDFs are qualitatively the same and the modes are shifted by 10% maximum. This level

of agreement of the GMM will suffice for exploring the qualitative behavior of the supersaturation distribution under varying assumed $T - q_v$ correlations.

Assuming the correlation coefficient between temperature and water vapor remains the same, the effects of differential diffusivity of scalars are explored by varying Pr and Sc. In order to understand the effect of scalar forcings, the correlation coefficient between $\mathcal{N}_T(0,1)$ and $\mathcal{N}_{q_v}(0,1)$ is changed and further in section 5.4 explored without considering the differential diffusivity effects .

5.4 Results

The supersaturation PDFs simulated using LES are shown in Fig. 5.1, for temperature differences of 8 K, 10 K, 14 K and 18 K with an initial mean of 283.16 K. Though the bulk temperature and bulk water vapor PDFs are Gaussian in nature, a negatively skewed supersaturation PDF is observed in the bulk of the chamber. From Table 5.1, it is clear that the magnitude of the skewness is larger at lower temperature differences than at higher values. For LES, the term 'bulk' here refers to all the grid cells that are at least 12.5 cm away from the walls of the chamber, in order to avoid the wall effects.

In order to understand this negative skewness, the supersaturations obtained from

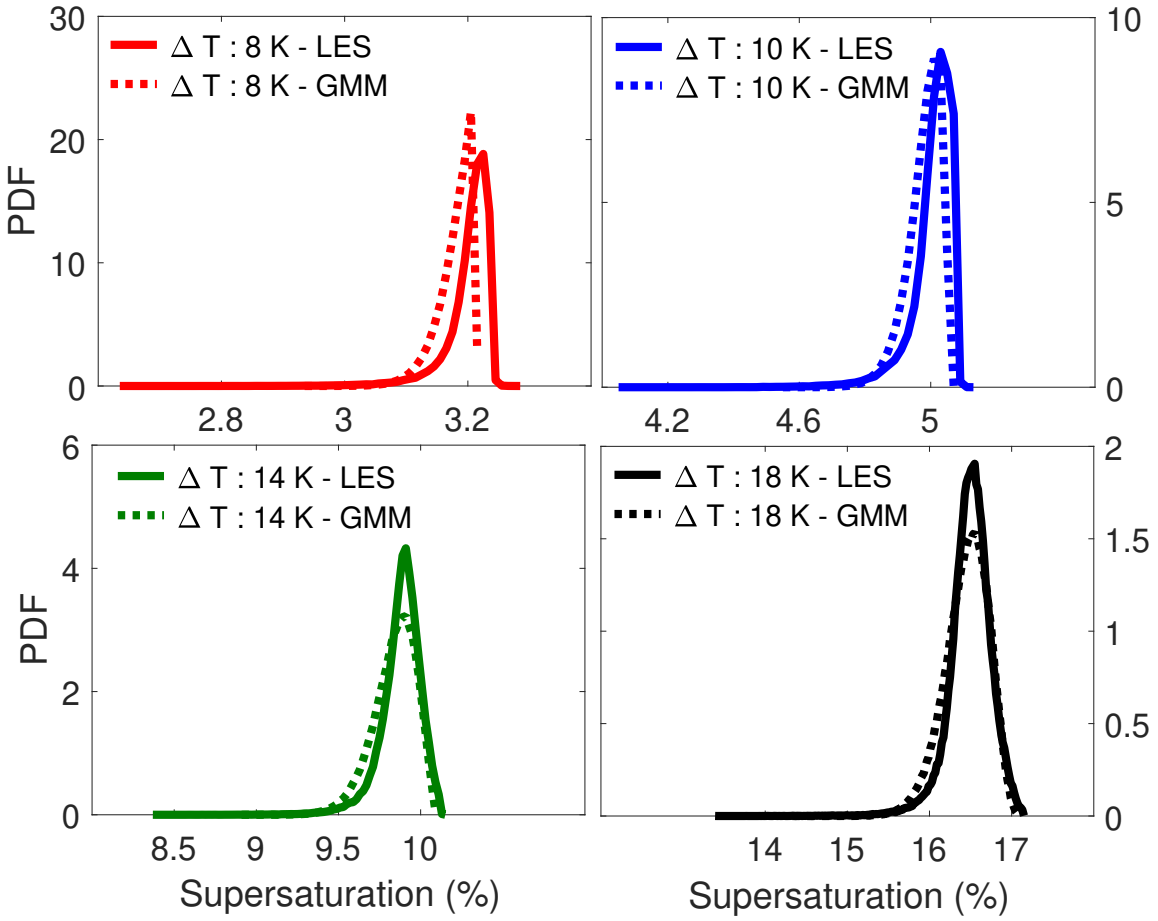

Figure 5.1: Cloud–free Rayleigh-Bénard convection supersaturation PDFs for different temperature differences (ΔT, refer to labels) centered at the same mean temperature (T_m = 283.16 K). As the temperature difference increases, the supersaturation PDF becomes more symmetric. The LES data is obtained from the *bulk*, whereas the GMM data is obtained at the center of the chamber $z = 0.5H$.

the LES runs are plotted against temperature. A mixing curve obtained by mixing parcels from top and bottom plates, characterized by different temperature and saturated water vapor mixing ratios, in different proportions, is also shown. In Fig. 5.2 the mixing curves (dashed lines) are plotted in supersaturation and temperature coordinates. The filled circles are the LES results from the bulk of the chamber. For a RBC system without the density effects, the density–weighted mean temperature is

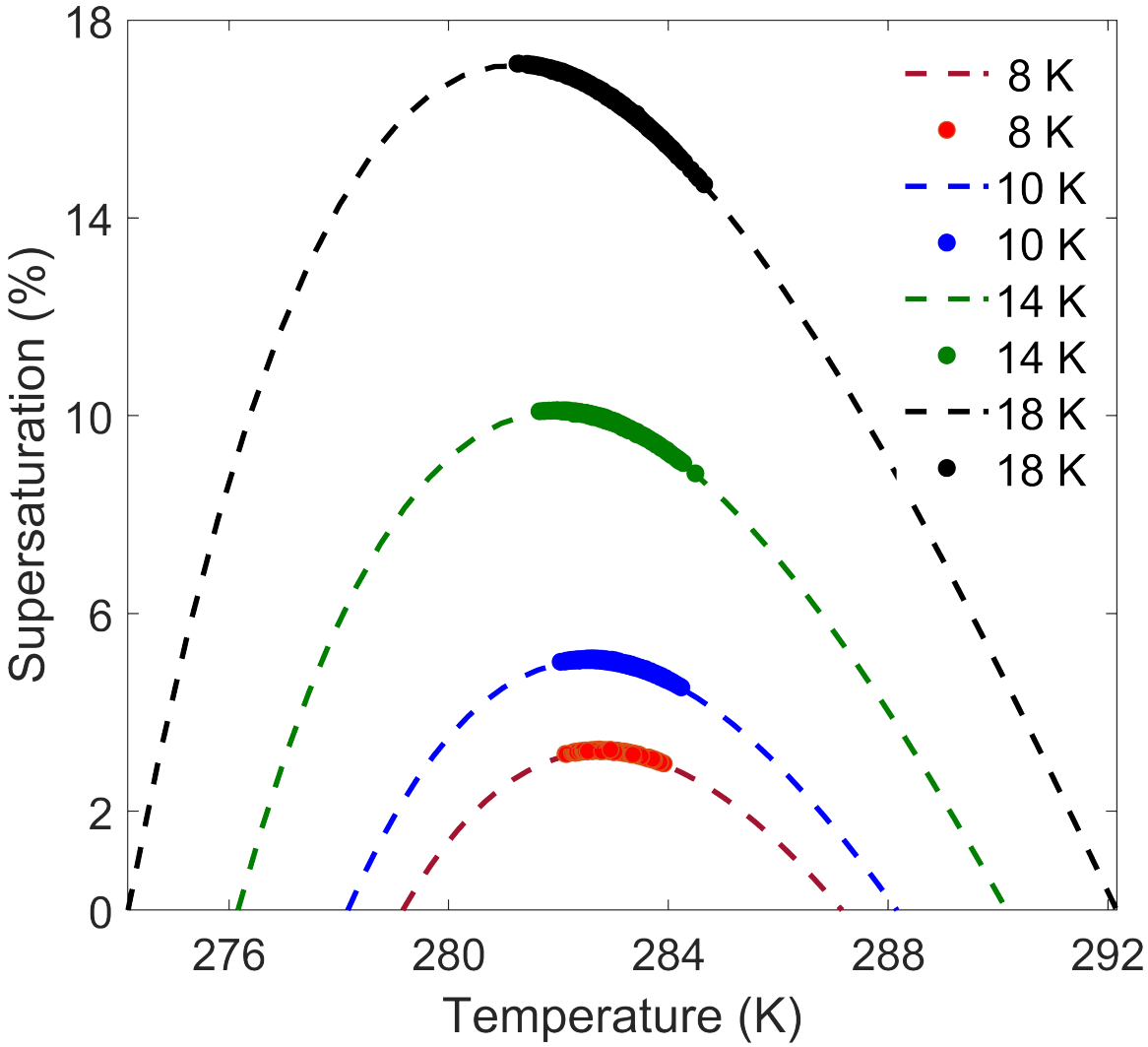

Figure 5.2: Supersaturation versus temperature, illustrating the mixing line (dashed line) and LES data (filled circles) for different temperature differences (ΔT, refer to labels) centered at the same mean temperature ($T_m = 283.16$ K). Note that only a small part of the mixing curve is sampled during a turbulent mixing process in the bulk. The part of the mixing curve sampled becomes less symmetric as the temperature difference is increased.

the mean temperature between the top and the bottom plates. At low temperature differences, the peak of the mixing curve coincides with the density–weighted mean temperature, hence the mode of supersaturation is the maximum supersaturation. As the temperature difference increases, the peak of the mixing curve shifts to lower

ΔT (K)	$\overline{T}$ (K)	σ_T (K)	Mean (%)	Mode (%)	Skewness
8	283.09	0.2492	3.201	3.22	-2.70
10	283.05	0.3993	4.985	5.04	-2.47
14	282.94	0.5012	9.842	9.91	-1.51
18	282.86	0.6041	16.437	16.53	-1.14

Table 5.1
Mean, mode and skewness of supersaturation for different temperature differences. These results are obtained from the LES simulations starting with a mean temperature of 283.16 K. Note the decrease in supersaturation skewness as ΔT increases.

temperature. This leftward shift of the mixing curve arises from the non-linear nature of the Clausius–Clapeyron equation. Hence the density–weighted mean temperature in the fluid moves from the maximum to the relatively linear region of the mixing curve. Furthermore, the region of the mixing curve sampled by the *bulk* increases, due to the increased variance of temperature and water vapor as a result of increase in Rayleigh number. Though density effects (Non-Boussinesq effects) can counter-act these effects by reducing the positive skewness of the mixing curve and reducing the mean temperature, these effects are negligible for our conditions (refer to Table 5.1). Please note that all of the mixing line is not populated because only the bulk is sampled, the rest of the mixing line can be sampled from the boundary layer regions near the top and bottom walls.

Figure 5.3(a) plots q_v versus T, comparing the Gaussian mixing model (red dotted line) and LES results (blue). Notice that they lie on a straight line joining the points corresponding to the state of the top and bottom plates. Figure 5.3 (b) compares the supersaturation PDFs obtained from the LES and the GMM. The deviation of

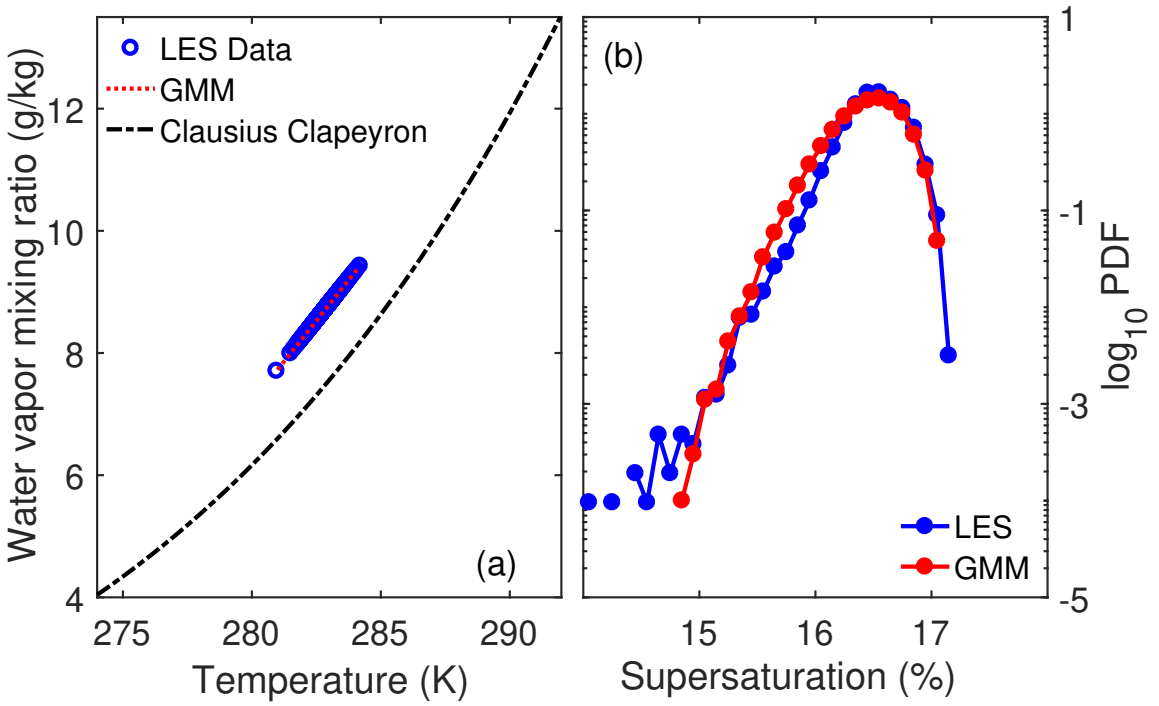

Figure 5.3: (a) Water vapor mixing ratio versus temperature, showing the Clausius–Clapeyron line (black dashed line), LES data (blue filled circles) and GMM data (red dotted line). (b) Comparison of supersaturation PDF of LES data (blue) and GMM data (red), notice LES data has a longer negatively skewed tail compared to GMM results. Plots are generated with $\Delta T = 18$ K and $T_m = 283.16$ K. LES assumes the same turbulent diffusivities for temperature and water vapor, and for comparison the GMM also assumes the same diffusivities for temperature and water vapor in the calculation of standard deviations of these scalars.

the the model from the LES results is probably due to the approximation of scalar fluctuations to be Gaussian. The skewness of the temperature data from the LES reveals a slight positive skewness of the order of 0.1, compared to 0.0 for a perfect Gaussian distribution. The density effects drive the mean *bulk* temperature to slightly less than the average of top and bottom plate temperatures, hence more positive fluctuations arise to reduce this difference.

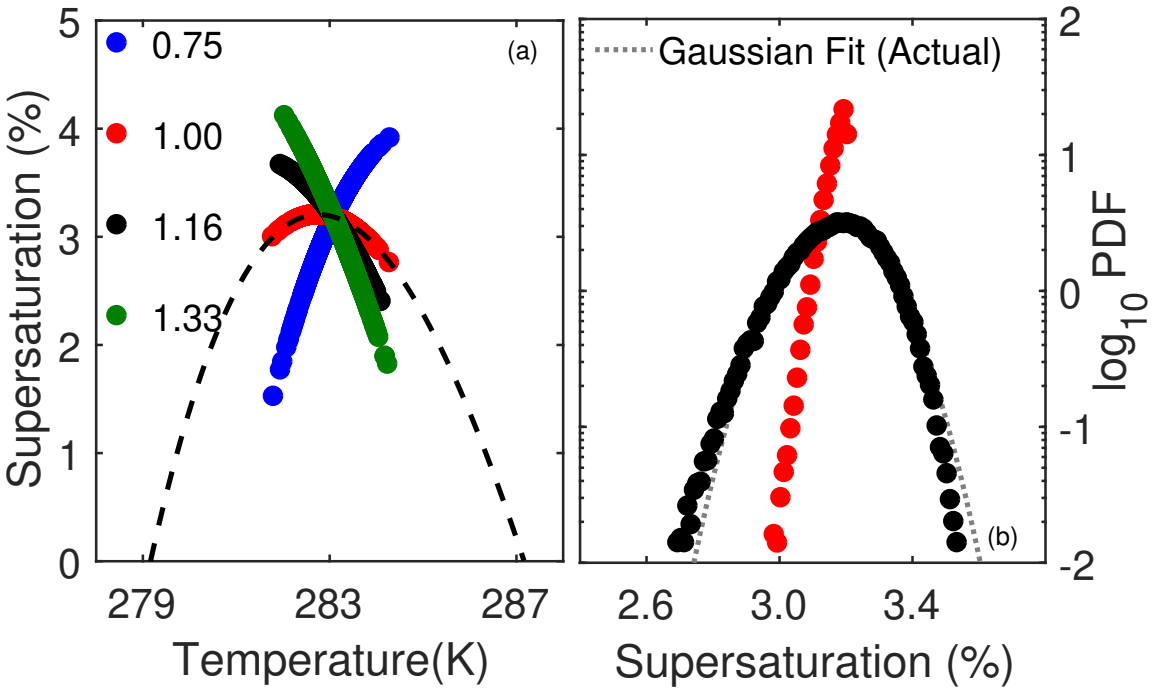

Figure 5.4: Supersaturation versus temperature and supersaturation PDFs illustrating the effect of differential diffusivity in the mixing process, by varying the ratio of ν_v/α shown in different colors. Panel (a) shows the distribution of these points about the mixing curve (dashed black curve). Panel (b) compares the PDF generated with real physical diffusivities (black) compared to a case with same diffusivities (red). The differential diffusivity results in a deviation from theoretical mixing processes and this deviation results in the reduction of negative skewness. Though differential diffusivity reduces the skewness of the supersaturation PDF and increases the left–right symmetry, the supersaturation PDF is still negatively skewed. Results are obtained from the GMM for $\Delta T = 8$ K.

Figure 5.4(a) illustrates the effect of differential diffusivities on supersaturation fluctuations. The case $\nu_v = \alpha = Le^{-1} = 1$, shown in red is the diffusivity formulation ubiquitous across LES and most DNS. As discussed earlier, this result in a negatively skewed distribution of the supersaturation PDF. The physical diffusivities follow $Le^{-1} = 1.16$, and the role of differential diffusivity is explored with Le^{-1} of 0.75 and 1.33. An interesting observation is that except for when $Le^{-1} = 1$, the mixing process no

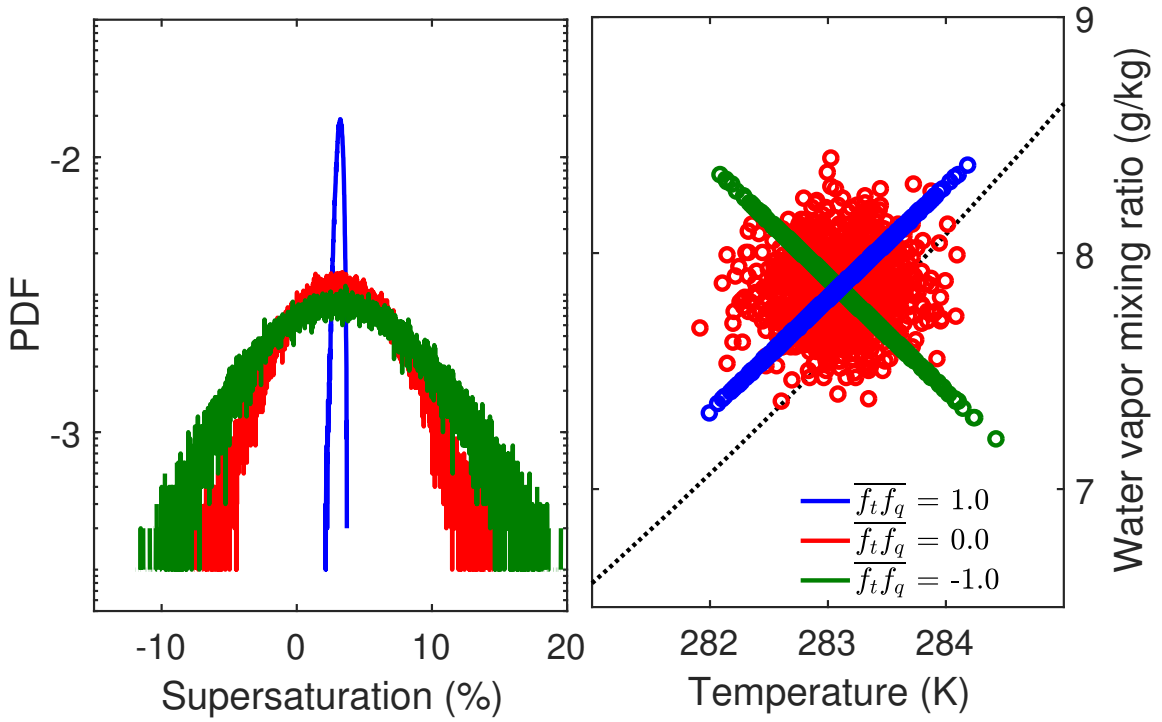

Figure 5.5: Panel (a) shows the saturation ratio PDF and panel (b) the mixing ratio versus temperature for different correlation coefficients ($\overline{f_T f_q}$) shown in different colors. Results are plotted assuming equal scalar diffusivities with $\Delta T = 8$ K. The mean temperature and the variance of scalars are the same across the different cases.

longer follows an isobaric mixing line (black dotted line). From the earlier arguments based on the density–weighted mean temperature, it is easy to see that the differential diffusivities do reduce the negative skewness of supersaturation as illustrated in Fig. 5.4(b). However, note that the PDF is still non-Gaussian and negatively skewed with $Le^{-1} = 1.16$. A detailed treatment of differential diffusivity and its role in the supersaturation PDF pertaining to RBC can be found in [3].

In all the cases discussed above, the forcings of temperature and water vapor, f_T and f_q respectively, have a perfect correlation. In Fig. 5.5 (a) we can see a broad symmetric

supersaturation PDF for uncorrelated and anti-correlated forcings of temperature and water vapor. We recall that for a cloud–free RBC system, as described in Sec. 5.3, the minimum saturation ratio that is allowed is 100%. However, for lower correlation coefficients, saturation ratios are as low as 90 % as show in the figure. Any decrease in forcing correlation from a perfect correlation coefficient of 1 (shown in blue) results in a change in the average slope of the distribution of points (panel a) and an increased spread of the distribution of points around the average slope. From Fig. 5.5(b), it is observed that the spread reaches a maximum when the scalar forcings are perfectly uncorrelated (shown in red) and as they become anti-correlated the spread starts to reduce and falls on a line for correlation coefficient of -1 (shown in green). During this process, the points fall below the limit imposed by the Clausius–Clapeyron line resulting in subsaturated conditions.

Figure 5.6 illustrates the effect of cloud droplet growth on the supersaturation generated by mixing. The blue dots represent the mixing line in the absence of cloud droplets and red dots represent the mixing in the presence of cloud droplets at the high Damköhler (Da) number limit [24]. The high Da case is similar to the bulk microphysics limit for which the mixing leads to points collapsing onto the Clausius–Clapeyron line. In Fig. 5.6 the straight, cloud-free mixing line approaches the Clausius–Clapeyron curve as the Damköhler number increases. The slight deviation the from Clausius–Clapeyron curve can either be the result of a numerical artifact or a physical process and cannot be resolved using the current LES model.

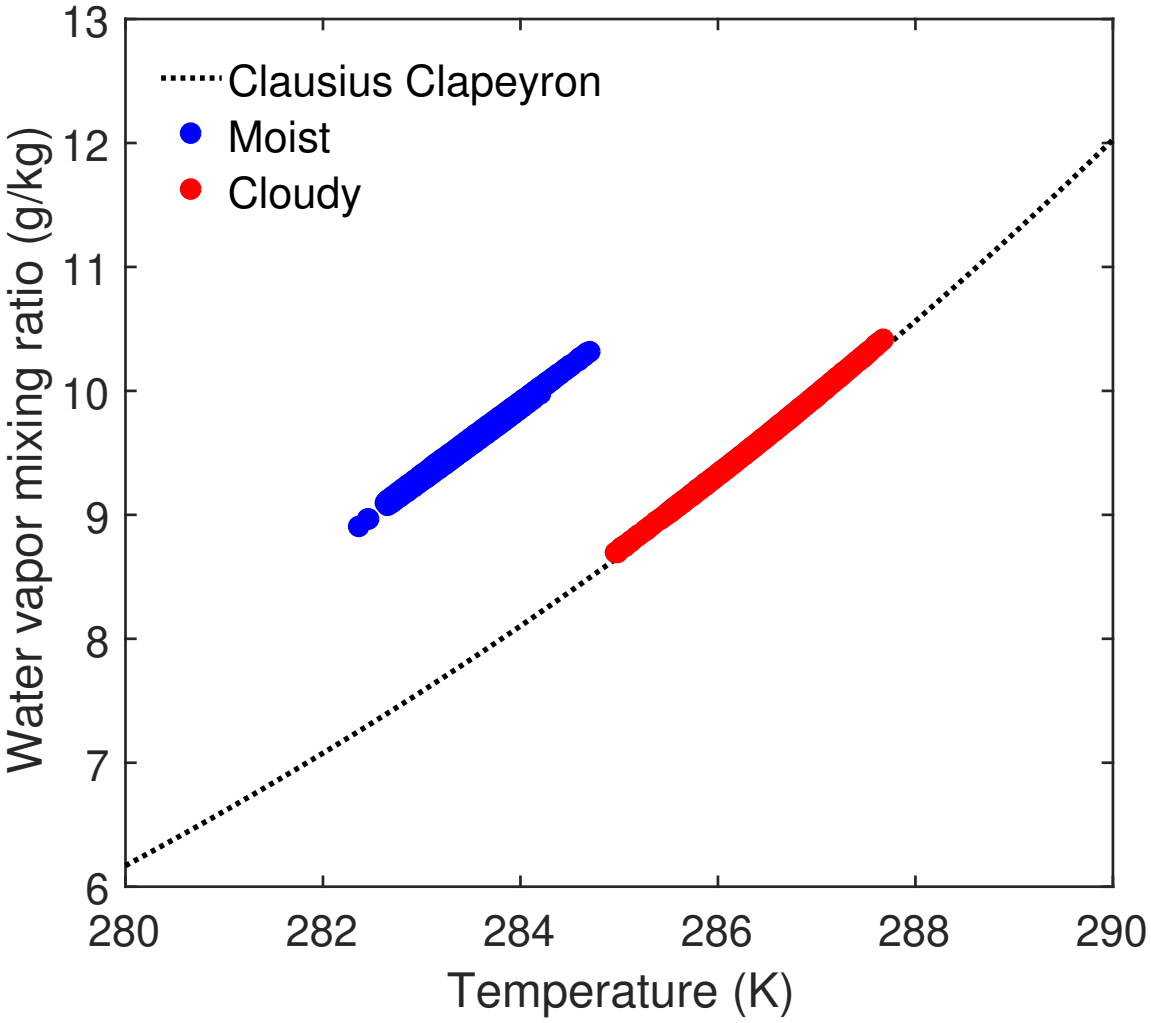

Figure 5.6: Mixing ratio versus temperature for cloud–free (blue) and cloudy (red) conditions simulated using LES for a ΔT = 20 K with T_m = 283.16 K, with equal diffusivities for temperature and water vapor. On reaching a steady state cloudy condition, the water vapor mixing ratio moves closer to the Clausius–Clapeyron line.

This transition requires careful investigation and will be explored in a future study.

5.5 Discussion and Concluding Remarks

The comparison and verification of the previously demonstrated numerical results with experiments is the focus of ongoing research. It depends on making measurements of the distribution of supersaturation in a turbulent flow, which is a significant experimental challenge. Very few direct measurements are available from the field [82, 117]. Progress toward in situ measurement of supersaturation in cloud–free Rayleigh-Bénard convection is discussed in [81]. Efforts for simultaneous remote measurement of temperature and water vapor concentration at sufficiently high precision for obtaining reliable supersaturation estimates are also being made [131].

In the current study, we use LES and a Gaussian mixing model to explore the isobaric mixing processes in an idealized turbulent cloud–free Rayleigh-Bénard convection system. In the idealized system we observe the supersaturation PDF to be non-Gaussian and negatively skewed, as shown in Fig. 5.1. Further, we observe the PDF to be more negatively skewed for smaller temperature differences than at higher temperature differences.

To understand the supersaturation PDF and how it may be generalized to other contexts, we explore the co-variance term $\overline{q_v' T'}$. We identify differential diffusivity,

condensation/evaporation processes and the correlation coefficient between any forcing of temperature and water vapor as possible causes of any change in the magnitude of the co-variance $\overline{q_v' T'}$. For example, using the GMM we notice that the supersaturation PDF tends to be less skewed when differential diffusivity is accounted for.

A detailed understanding of the effect of condensation/evaporation on $\overline{q_v' T'}$ would require a dedicated study over a range of microphysical conditions. However, for a high Dämkohler number [24] case, we observe that the mixing line falls on the Clausius–Clapeyron curve, assuming the same diffusivity for temperature and water vapor. In [125] it is observed that the supersaturation PDF tends to become narrower in the interior of the cloud, consistent with the high Dämkohler number predictions from [24]. Such a narrowing of the supersaturation PDF can be observed in the current study also — however the detailed source of destruction of the width of the supersaturation PDF would require a cloud droplet resolved study.

A key point emerging out of the current study is the importance of correlation coefficient between external forcings of temperature and water vapor, $\overline{f_T f_q}$. Figure 5.7 shows saturation ratio PDFs for several values of $\overline{f_T f_q}$ in panel a, and the corresponding mixing diagrams in panel b. The temperature difference is chosen to be 8 K (corresponding to Fig 9 from [3]), so that for cloud–free RBC with saturated boundary conditions any point in the bulk of the chamber cannot be subsaturated. However,

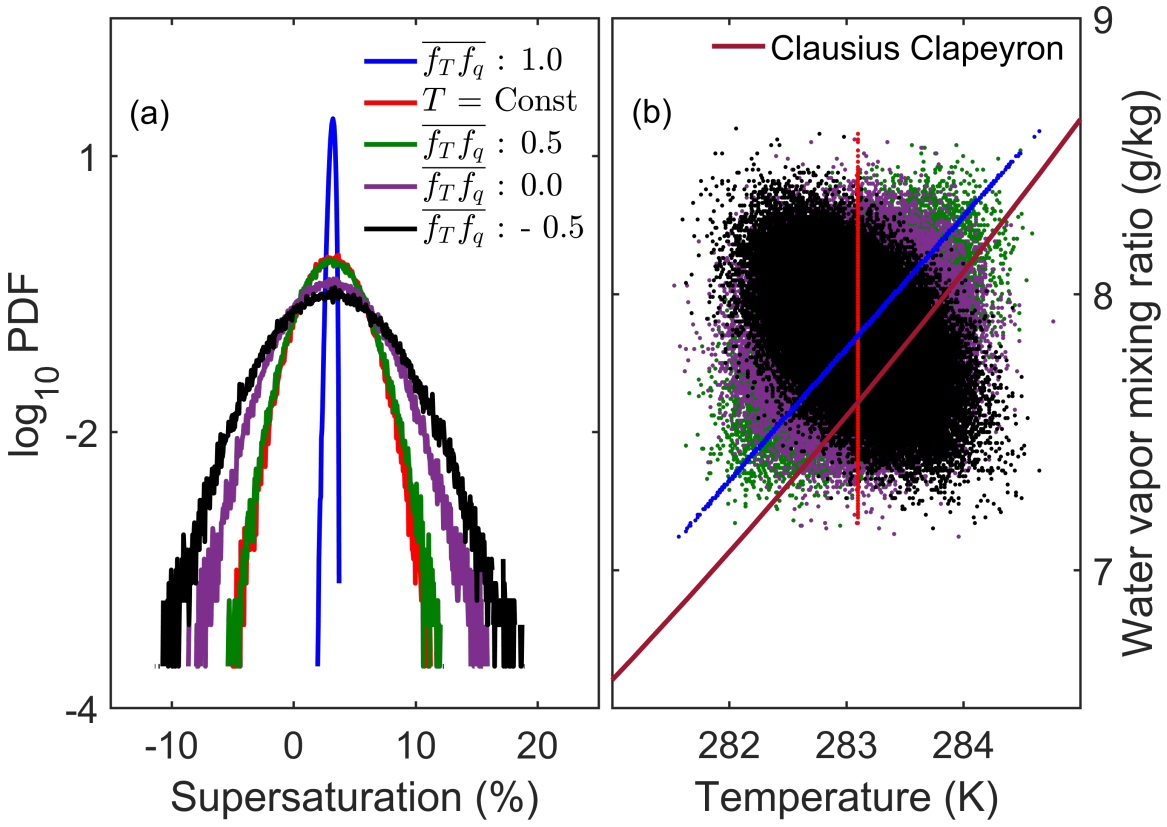

Figure 5.7: (a) Saturation ratio PDF and (b) mixing ratio for different correlation coefficients ($\overline{f_T f_q}$) from studies by [1, 2] and [3] shown in different colors. Results are plotted assuming same scalar diffusivities with $\Delta T = 8$ K. This temperature difference is chosen to match the supersaturation PDF shown in Fig 9 of [3]. Supersaturation fluctuations introduced by keeping temperature constant and fluctuating water vapor mixing ratio (red) [2].

by varying the correlation coefficient of $\overline{f_T f_q}$, such nonphysical sub-saturation fluctuations can be seen to exist. For an 8-K temperature difference, correlation coefficients of 0.5 (green), 0.0 (purple), -0.5 (black) are cases identical to those specified in [1]; with supersaturation fluctuations induced by water vapor alone (red) as in [2]; and with correlation coefficient of 1.0 (blue) from cloud–free One-dimensional Turbulence model (ODT) as in [3].

It should be noted that even though cloud–free RBC requires the forcings of temperature and water vapor to follow a relation of the form $\sigma_T \sim \sigma_{q_v} \Delta T / \Delta q_v$, that is not necessarily the case in all atmospheric contexts. For example, in the case of cloud-top entrainment [114], even though entrained air from above a capping inversion is at higher temperature, it is drier than the cloud air itself. Forcing terms for the air from a capping inversion region would have a correlation coefficient closer to -1, resulting in a more symmetric PDF for supersaturation fluctuations. In contrast, for lateral entrainment from subsiding shells into a cumulus cloud, the temperature and water vapor is more likely to be positively correlated[132].

For LES studies of the convection-cloud chamber [21] such as in [41], the boundary fluxes are modeled using Monin-Obukhov similarity theory, resulting in a perfectly correlated forcing from the boundaries. However, in the sub-grid scale model the temperature and water vapor fields are diffused with the same turbulent diffusivity. Therefore any positive supersaturations arising due to differential diffusivity are not captured, thus impeding the cloud droplet growth. Therefore the droplet size distributions obtained from such simulations should be at least somewhat narrower than what would arise from experiments or from a DNS accounting for differential diffusivity. In DNS studies that do not account for differential diffusivity effects, such as the cloud parcel studies by [2] that have only water vapor forcing (refer to the red points in Fig.5.7), a broader size distribution of cloud droplets is obtained than warranted by a physically consistent supersaturation field.

Atmospheric models [70, 133] typically use two separate prognostic variables to capture temperature and water vapor. Subsequently, the diagnostic variable – mean supersaturation – is calculated from temperature and water vapor in individual grid boxes ignoring any sub-grid scale variability that is important for cloud droplet activation [23] and growth [24]. The calculated supersaturation interacts with the microphysics scheme to produce cloud droplet numbers and the corresponding masses or higher moments depending on the scheme's complexity. Often, DNS studies [123, 124, 134] intended to understand the cloud droplet growth in a turbulent environment and treat supersaturation as a prognostic scalar disregarding the non-linear behavior of the Clausius–Clapeyron equation. The treatment of supersaturation as a scalar is suitable in regimes where the Clausius–Clapeyron equation can be linearly approximated. However, in systems such as Rayleigh-Bénard convection, this is no longer true since the production of mixing supersaturation relies inherently on the non-linear behavior of the Clausius–Clapeyron equation. Furthermore, there may be scenarios in which differential diffusivity needs to be accounted for, which would lead to the decorrelation of $\overline{Q_v' T'}$. Ignoring such processes may result in over-estimating the effect of turbulence on droplet growth. Finally, the correlation between temperature and water vapor depends on the processes that produce these fluxes. Hence careful evaluation of the correlation of temperature and water vapor is needed to accurately capture the extend of supersaturation fluctuations, as demonstrated earlier.

In the larger context, the concerns about subgrid-scale variability of temperature, water vapor and subsequent microphysics interactions highlighted by [133, 135] remains an open challenge even today, even in spite of LES studies with increasing resolution. One approach for addressing the subgrid-scale fluctuations considered by [125] is the use of a Linear Eddy Model, although this may be computationally expensive in full implementation. However, the GMM described here may provide a computationally inexpensive but efficient alternative to incorporate physically consistent subgrid-scale variability. A second part of the puzzle, involving supersaturation–cloud particle interactions still needs to be addressed. Re-examination of lateral entrainment studies with the consideration of negatively skewed supersaturation–microphysics interactions in the context of droplet activation and growth can help in answering the latter part of the puzzle.

Definitions of symbols in Chapter 5

q_v : Water vapor mixing ratio

$q_{sat}(T)$: Saturation vapor mixing ratio at temperature T

$q_v/q_{sat}(T)$: Saturation ratio

U : Velocity vector of the fluid

$\dot{q}_l$: Rate of condensation/evaporation of water vapor

L_v : Latent heat of vaporization of water

C_p : Specific heat of air at constant pressure

$f_T,\ f_q$: External forces on T and q_v

$\rho_{t/b}$: Density of air at top (t) and bottom (b).

$T_{t/b}$: Temperature at top (t) and bottom (b).

$q_{vt/b}$: Water vapor mixing ratio at top (t) and bottom (b).

ν_v : Water vapor diffusivity

α : Thermal diffusivity

Le : Lewis number $(\alpha\,/\,\nu_v)$

ΔT : Temperature difference between top and bottom plate

Δq_v : Water vapor mixing ratio difference between top and bottom plate

σ_T : Standard deviation of temperature T

σ_{q_v} : Standard deviation of water vapor mixing ratio q_v

Sc : Schmidt number $(\nu \,/\, \nu_v)$

Pr : Prandtl number $(\nu \,/\, \alpha)$

Le : Lewis number $(\alpha \,/\, \nu_v)$

ν : Momentum diffusivity

ν_v : Water vapor diffusivity

α : Thermal diffusivity

C_1 : Proportionality constant for Eqs. 5.16 and 5.17

z : Vertical location in the chamber, assumed to be $0.5H$

H : Height of the chamber

Ra_m : Moist Rayleigh number $\left(\dfrac{g\,\beta\,\Delta T\,H^3}{\nu\,\alpha} + \dfrac{g\,\epsilon\,\Delta q_v\,H^3}{\nu\,\alpha} \right)$

g : Acceleration due to gravity

β : Thermal expansion coefficient $\left(1/\overline{T}\right)$

ε : Ratio of gas constants of air and water vapor(≈ 0.622)

Chapter 6

An Uber Pi Chamber

"The problem with life was that there was a constant lack of experience: you learned from the past, yes, but the future held new and unexpected things in store."

- Terry Pratchett, Pyramids

6.1 Introduction

The results in Chapters 3, 4 and 5 pertain to a cloud chamber of size $2m \times 2m \times 1m$, which is the same as the MTU Pi Chamber. The unanswered question is, how do the conclusions based on the observations from the cloud chamber ($\sim \mathcal{O}(1)m$) translate

into explaining the atmospheric cloud processes ($\sim \mathcal{O}(1000)m$). Similarly, recent discussions at a workshop held at the Foothills Laboratory of NCAR emphasize the importance of building a large-scale facility.

Apart from the new experimental approaches and improved instrumentation, the advancement of computational models validated against the experiments emerged to be a resonating point in the workshop. Therefore, as a first step, we scale the cloud chamber simulations discussed in Chapter 3 to study a chamber of larger height with the same aspect ratio as the Pi chamber in order to avoid any effects of aspect ratio. In the current study, we investigate how the fluctuations of temperature and water vapor change with height, how do the microphysical properties vary with height, and finally, if there is a height dependence on the collision-coalescence.

6.2 Methodology

In Table 6.1, the physical dimensions of four cloud chambers with heights 1 m, 2 m, 4 m, and 8 m are shown. The grid size for each chamber is 3.125 cm, and the time step is 0.02 seconds, the same as the Pi cloud chamber discussed in Chapter 3. The grid size and time steps are maintained to ensure there is no grid dependence for the scalar and momentum fluxes from the top and bottom boundaries. We evaluate the capability of LES to represent the temperature scaling for an RBC system discussed

H	Physical Dimensions	Grid Boxes
1	2 m x 2 m x 1 m	64 x 64 x 32
2	4 m x 4 m x 2 m	128 x 128 x 64
4	8 m x 8 m x 4 m	256 x 256 x 128
8	16 m x 16 m x 8 m	512 x 512 x 256

Table 6.1
Heights, physical dimensions and the corresponding grid box numbers used to generate Figure 6.1.

in Chapter 2.

To study the effect of height on both condensational and collision-coalescence growth of cloud microphysics, we use a double moment spectral bin microphysics scheme described by Chen and Lamb[105], unlike Chapter 2. The bin microphysics coded by Dr. Fan Yang of Brookhaven National Laboratory has a more refined grid spacing and reduced numerical diffusion than the HUJISBM. Chambers of heights 4 m and 8 m are not explored for cloudy conditions due to the computational expense associated with bin microphysics.

In all the simulations, the temperature difference between the top and the bottom plate is 14 K. All the walls are assumed to be saturated. However, the lateral walls are assumed to be adiabatic for scalars temperature and water vapor.

6.3 Results

6.3.1 Scaling of the scalar variance with height

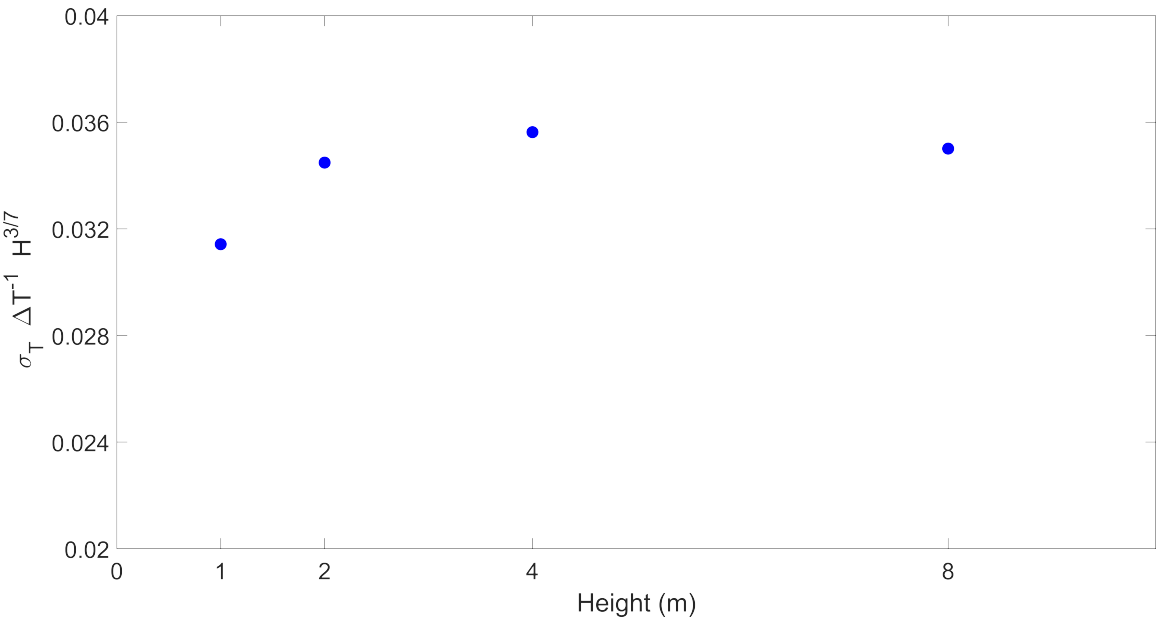

Figure 6.1: Compensated temperature fluctuations are plotted against the height of the chamber. The temperature difference between the top and the bottom plate is 14 K and the mean temperature is 283.16K.

Figure 6.1 shows standard deviation of temperature σ_T vs. H, with σ_T compensated by the scaling demonstrated in Section 2.1 of Chapter 2. The fluctuation of temperature scaled by temperature difference ΔT and height H is expected to be a constant. For each chamber, the temperature is obtained by excluding the boundary data points ($\sim$ 25% of total grid points in each direction). Further, we notice the fluctuations reach a constant when we sample sufficiently large volumes over a sufficiently long

period. The lack of collapse in the first data point might be due to the absence of sufficient averaging.

6.3.2 Microphysics with height

We compare cloud chambers of heights 1 m and 2 m, with collision-coalescence physics turned on and off. Further to make fair comparisons, we ensure the number of cloud droplets per unit volume is the same for both chambers. Firstly, we run cases of different CCN injection rates for a cloud chamber of height 1 m. Then, we fit a relation between the CCN injection rate and the cloud droplet number for a given chamber and temperature difference. Figure 6.2 demonstrates a linear fit obtained for the cloud chamber of height 1 m by plotting the cloud droplet number density obtained from LES with Chen and Lamb[105] microphysics against the aerosol injection rate for a temperature difference of 14 K. The linear fit is used to adjust the injection rate of CCN for a cloud chamber of height 1 m at 14 K temperature difference to match the cloud droplet numbers from chambers of height 2 m or 4 m.

The cloud chamber of size 2 m is run for two different aerosol injections corresponding to two different cloud droplet numbers. The cloud droplet numbers are matched for chambers of heights 1 m and 2 m using the parameterizations shown in Figure 6.2.

Droplet size distribution PDF of cloud droplets are shown in Figure 6.4. Cases with

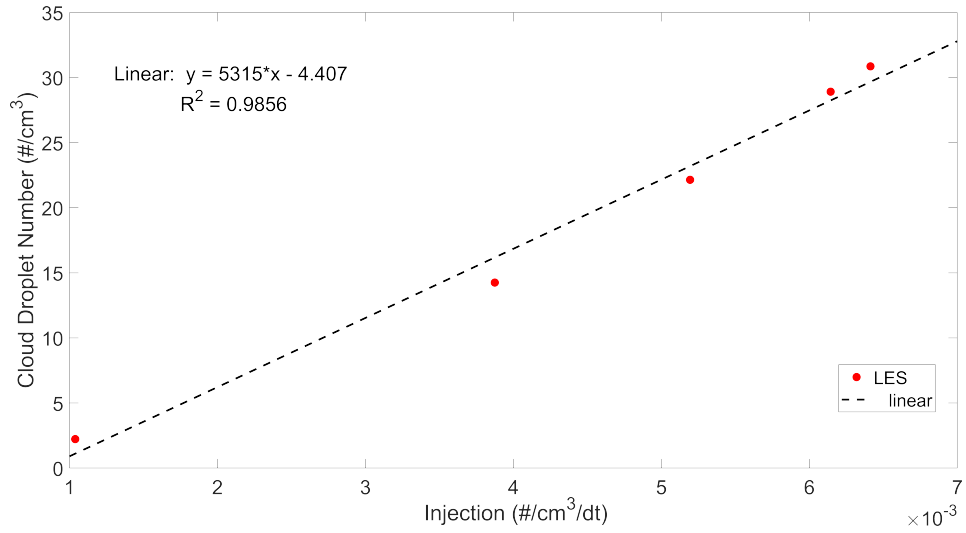

(a) Low cloud droplet number

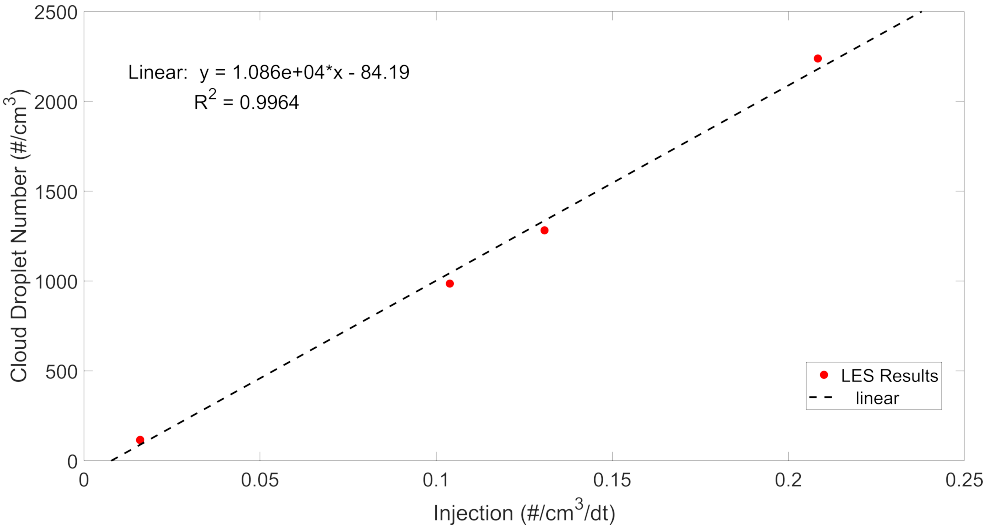

(b) High cloud droplet number

Figure 6.2: Linear fit of aerosol injection rate vs. cloud droplet number for cloud chamber with height of 1 m. The temperature difference between the top and the bottom plate is 14 K and the mean temperature is at 283.16 K.

collision-coalescence physics turned on and off are compared for chambers of sizes 1 m and 2 m. We notice that regardless of the height of the chamber, the cloud droplet size PDF with the collision physics turned off (blue and green dashed lines)

remains identical. Further, we notice that the liquid water content per unit volume and the precipitation flux remain identical for the same aerosol injection conditions for chambers of different heights. We know the supersaturation fluctuations for a larger chamber for the same imposed temperature difference. In the numerical simulations, the mean supersaturations are identical for chambers of different heights, and the supersaturation fluctuations are narrower for the larger chamber (refer to Chapter 2). Therefore, the relative magnitudes of the mean and fluctuating components of supersaturation in the condensational droplet growth regime need to be explored. Additionally, the relative roles of the turbulent transport of cloud droplets to the gravitational settling is an integral part of understanding the precipitation observed. These two puzzle pieces need to be solved to better comment on the surprisingly identical droplet size distributions shown in Figure 6.4. When the collision physics are turned on, we observe the droplet size distributions to be broader than the cases with collision physics turned off. Due to the effect of variability from the last two bins, we cannot conclude if the collision rates are dependent on the height of the chamber.

In Figure 6.3, the comparison of droplet size distributions for chambers of sizes 1 m, 2 m, and 4 m are shown with the collision physics turned off. The number of cloud droplets are respectively 450 cm^{-3}, 472 cm^{-3}, and 476 cm^{-3}. Similar cloud droplet numbers were obtained by fitting an injection rate vs. cloud droplet number graph for chambers of sizes 1 m and 2 m. The CCN injection rates for 1 m and 2 m were

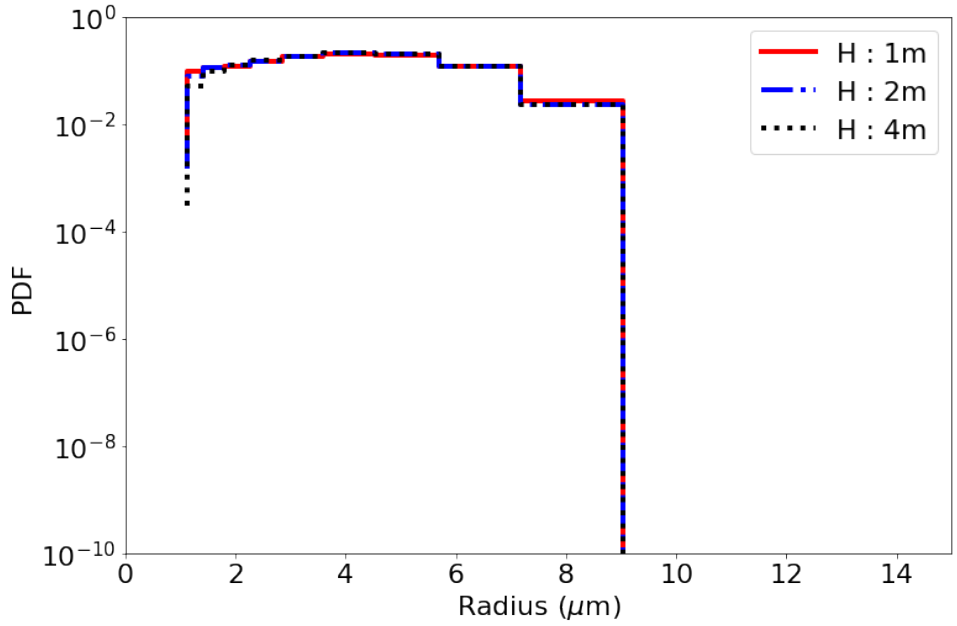

Figure 6.3: Cloud droplet numbers are matched for the cloud chambers of height 1 m, 2 m, and 4 m for a temperature difference of 14 K and mean of 283.16 K.

respectively 5.05 times and 1.68 times the CCN injection rate of a cloud chamber of height 4 m. We notice that, for the chambers of different heights (1 m, 2 m, and 4 m), for similar cloud droplet numbers, for the same boundary conditions, we have identical droplet size distributions. However, we could not make a comparison for the 4 m case with collisions turned on because it requires extensive computational power. This therefore remains an ongoing work.

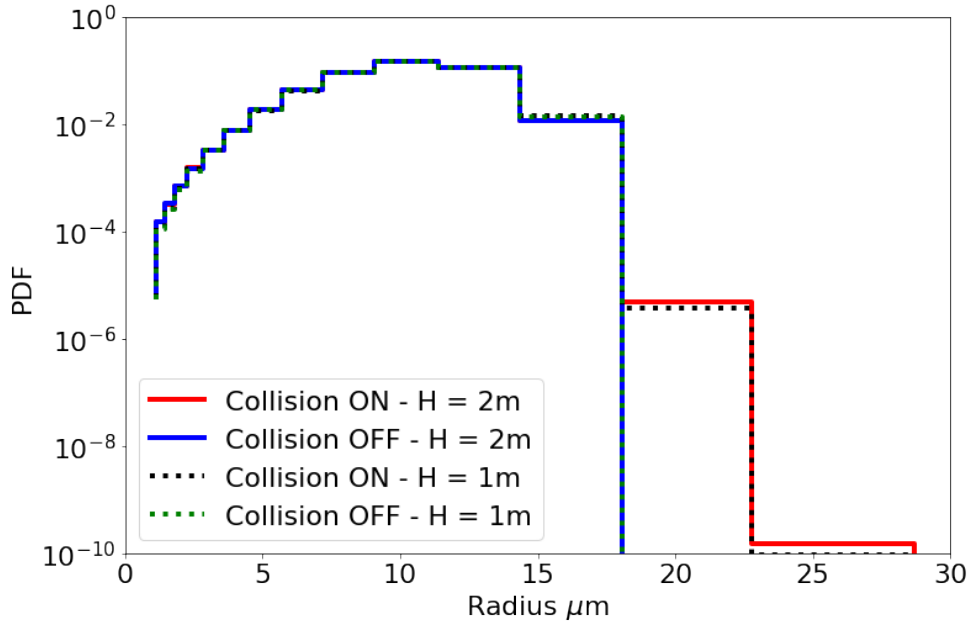

(a) Low cloud droplet number : $38/cm^3$

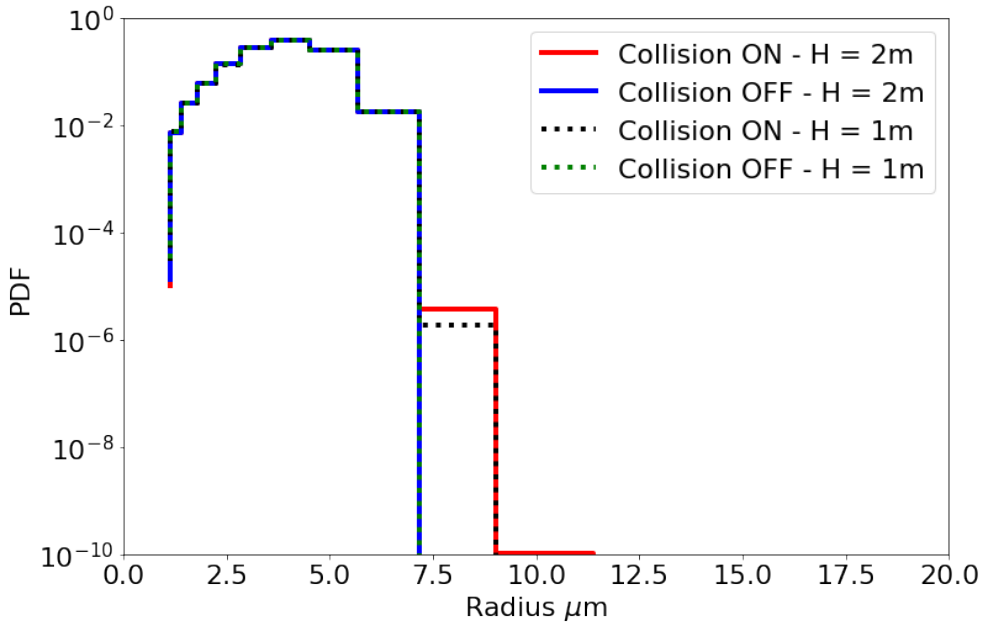

(b) High cloud droplet number : $2000/cm^3$

Figure 6.4: Cloud droplet numbers are matched for the cloud chambers of height 1 m and 2 m for a temperature difference of 14 K and mean of 283.16 K. The liquid water content is 0.11 g/kg and 0.37 g/kg respectively for low and high number concentration cases. The mean radii are respectively 7.5 and 3.04 μm.

6.4 Point vs Dispersed Injection of Aerosols

In the Michigan Tech Pi Chamber, we inject aerosols at a single point in the volume of the chamber. We explore the impact of the location of the aerosol injection on the cloud droplet size distribution. Figure 6.5, illustrates that point injection produces cloud droplet size distributions that are broader than the dispersed injection cases. There will be spatial variability in the droplet number for the low cloud droplets number case since the droplets are transported only via advection, diffusion, and gravitational settling. Furthermore, the smaller size droplets tend to be concentrated in a small region around the point injection region compared to the dispersed injection case. However, for high cloud droplet number cases, the point vs. dispersed injection does not differ since unactivated aerosols are present abundantly. In the high cloud droplet number case, the point injection tends to produce numerical instability at the grid box of the injection in HUJISBM, producing non-physical negative supersaturations.

The studies presented in the current chapter are a pioneering first step towards building a larger cloud chamber. The results from these studies can serve as a first-order approximation and guidance towards the engineering and the cloud microphysics challenges faced in building a larger chamber.

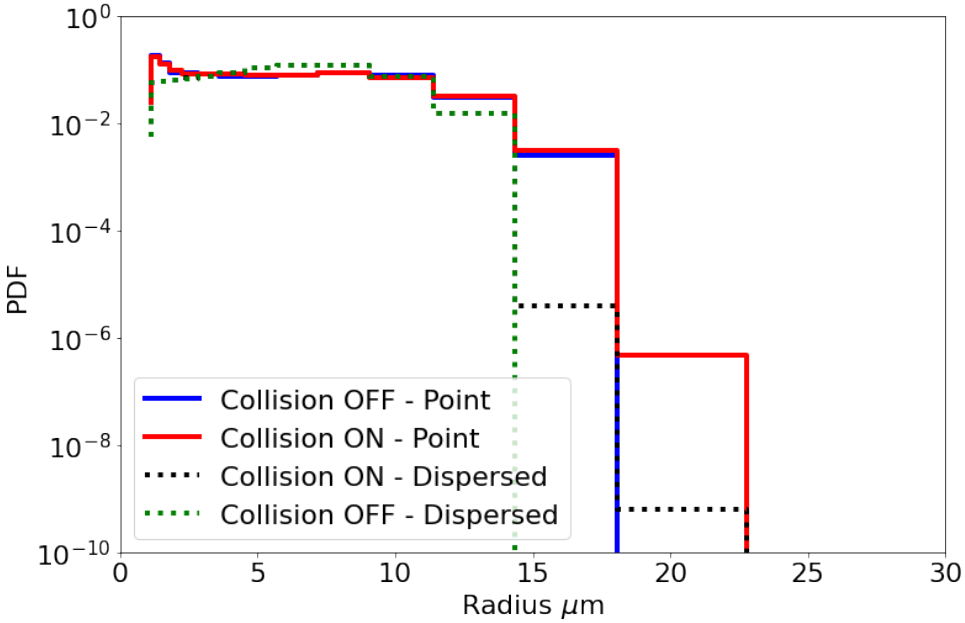

(a) Low cloud droplet number cases

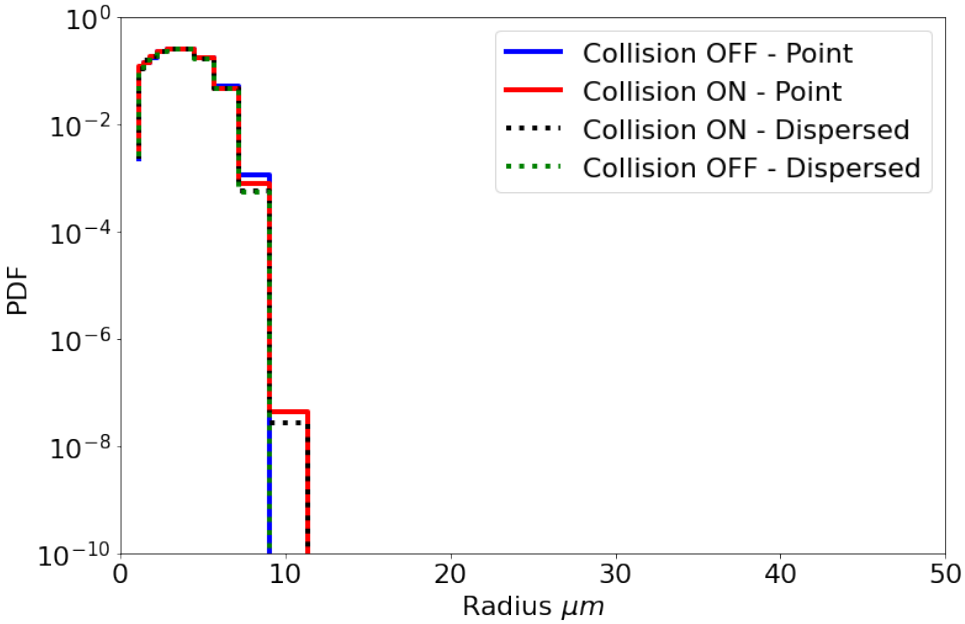

(b) High cloud droplet number cases

Figure 6.5: Cloud droplet size distributions for point and dispersed injection in a cloud chamber of height 1 m. The temperature difference is 14 K and the mean temperature is 283.16K.

Chapter 7

Conclusion

"We can only see a short distance ahead, but we can see plenty there that needs to be done."

- Alan Turing

The models and results discussed in Chapters 3, 4, and 5 are appropriate under the given assumptions. However, in this Chapter, we discuss some of the limitations and, consequently, how to improve their physics and computational efficiency.

7.1 Limitations of the SAM model

7.1.1 Sidewalls

Modifying SAM to emulate Pi Cloud Chamber requires adding sidewalls to account for momentum flux, heat flux, and water vapor flux to and from the sidewalls to the bulk. The sidewalls can either be adiabatic to heat or water vapor but not to both because of the non–linear relationship of the Clausius Clapeyron equation. Therefore, there is a continuous flux of temperature, water vapor, or both from sidewalls to the bulk for a physical cloud system. We use the Monin-Obukhov similarity theory in the unstable configuration for the four lateral sidewalls to emulate scalar fluxes in the current model.

The flux transfer from the walls depends on the interaction between bulk and wall surface. The nature of interaction depends on the flow conditions close to the wall. A chamber with a box configuration tends to lock the large-scale convection along the corners, causing two faces to have partial updrafts and the other two with partial downdrafts. Therefore, the nature of convection – free/ mixed convection depends on Richardson's number and needs to be investigated.

The amount of water vapor flux depends on the level of saturation of the walls.

Though, one can assume saturated conditions at the sidewalls or reduce the saturation value of sidewalls to attain the required bulk supersaturation as in [41]. Experimentally measuring the great unmeasurable – supersaturation can yield some clues to the saturation level in the sidewalls[81].

The sidewall–bulk interactions can serve as a proxy to study entrainment-microphysics interaction in a laboratory under controlled turbulence.

7.1.2 Boundary layers

Apart from the boundary layer associated with sidewalls, modeling of the bottom boundary layer is an area that requires attention. In the context of Rayleigh Bénard convection, the definition of boundary layer remains controversial - we adopt Howard[136] approach. The thickness of the boundary layer depends on the Nusselt number, which depends on the imposed temperature difference between the top and bottom walls. In the current simulations, the boundary layer - bulk interactions are again approximated by Monin Obukhov Similarity theory. Even if the scalar fluxes are computed accurately, the microphysics-dynamics interactions are not well resolved – the competition between the terminal velocity of the droplets and the vertical velocity of the fluids determine the rate at which the droplets settle.

Since the boundary layer tends to be the order of grid size of the current model,

we do not capture any velocity profile that might exist within the bottom grid. For large droplets, the settling might be captured accurately owing to larger settling velocities. However, for smaller droplets, the rate of settling of the droplets might be accelerated or impeded compared to the actual conditions in the current model affecting the droplet size distributions.

There are several approaches to study the settling problem; a straightforward approach would be to generate statistics for inertial point particles Rayleigh-Bénard convection using DNS as in [52] of different sizes. From the presentations associated with ICMW 2020, we have realized this model has been extended to study the Pi-Chamber with periodic lateral wall approximations with droplet growth accounted for. Since the maximum true resolution achievable by the model is limited to $Ra \sim \mathcal{O}(10^6)$, this model can provide some guidance regarding the rates of settling of the droplets.

Another approach is to model the boundary layer profile using the one-dimensional turbulence (ODT) in conjunction with the discussed LES model [137, 138]. Such an approach would replace the current precipitation model with the newly developed ODT - droplet settling interactions. Though LCM - linear eddy mixing - LES, interactions have been studied using [125], the aforementioned droplet settling model is not relevant for their study and hence absent from the model.

7.2 Advances in Microphysics

7.2.1 Lagrangian Cloud Modeling

Lagrangian cloud modeling does provide an advantage for the modeling of cloud droplets at the expense of computational power in atmospheric systems. However, studies [42] have demonstrated that there is no significant advantage of using LCM over a well-resolved bin model in the context of the cloud chamber. Introducing sub-grid scale fluctuations with LCM [125] can reach an entirely different conclusion. A missed opportunity in the context of LCM/super-droplet studies is the effect of multiplicity and statistical averaging in terms of cloud droplets, and they need to be validated against reliable experimental measurements such as cloud chamber. The emerging body of literature treating super-droplets as the panacea for all maladies is yet to explore and acknowledge the method's physical and computational limitations.

The experimental inter-comparisons with LES-LCM (SAM-LCM, CM1-LCM, Baby EULAG) models can provide much-needed test and validation of the super-droplet method. Questions of scientific interest such as the effect of the cloud droplet number–supersaturation interaction[23] can be studied with such models.

7.2.2 Machine Learning

In recent years, machine learning has been used to represent the sub-grid scale model for climate models [139]. The accuracy of such statistical models depends on the training dataset, which is generated from CCSM-CRM setup [48]. The numerical-experimental synergy with the cloud chamber provides two different opportunities in the context of machine learning models.

Firstly, the cloud chamber has generated stationary and independent datasets from the last six years of operation. This enormous dataset can serve as a training dataset for various machine learning models based on the experiments. The trained model can interpolate into the new dynamics and microphysics conditions. Further, a machine learning model can flag anomalies in the measurements from Pi Chamber based on past expectations

A second opportunity would be to use the 3D results from the numerical simulations[140] of Cloud Chamber in ICMW 2020 as a training data set to develop machine—learning dataset. This model can generate a 3D picture of vertical velocity, temperature, water vapor, number of cloud particles, and their location in the chamber.

The results generated using the models discussed above apply only to the experiments

and simulations in the cloud chamber. However, a larger philosophical question is to evaluate the physical or computational benefit one would derive from applying ML techniques, or are we jumping on to the ML bandwagon[141]?

7.3 Lotka–Volterra Models

In the current thesis, we have explored the behavior of the cloud-chamber using numerical models by solving the differential equations for dynamics and microphysics at each grid box. The average behavior of the system is obtained by the spatial and temporal averaging of independent samples from the bulk. As the number of grid points increases, the computational power and time required to solve these equations increase.

Hence, another approach would be to use bulk models with a system of equations as described in 2. Here, we use equations to describe other physical systems to describe the cloud chamber.

Lotka–Volterra equations used to describe the populations of predator–prey has been used to describe non–linear systems [142].

The cloud chamber system can be modeled as a predator – prey model. The cloud–chamber can be modeled as follows,

1. The water vapor gets preyed on by liquid water.

2. The liquid water gets removed by Stokes' settling.

3. The water vapor gets replenished from the surface.

$$\frac{\partial q_v}{\partial t} = \frac{q_v - q_{v0}}{\tau_t} - \frac{\dot{q_L}}{\tau_c} \tag{7.1}$$

$$\frac{\partial q_L}{\partial t} = \frac{\dot{q_L}}{\tau_c} - \frac{q_L}{\tau_s} \tag{7.2}$$

The Eq. 7.1 is the evolution of water vapor, the first term in the RHS represents the water vapor replenishment from the surfaces, and the second term the conversion of water vapor to liquid water. The second term in the RHS of Eq. 7.2 is the removal of liquid water at a time scale given by Stokes' settling.

The rate of conversion of water vapor to liquid, supersaturation, time scales τ_c and τ_s depend on the number of droplets, n and mean radius $\overline{r}$. The values of n and $\overline{r}$ depend on the microphysics, therefore we need to add another equation

$$\frac{\partial n}{\partial t} = \dot{n}_{act} - \frac{n}{\tau_s} \tag{7.3}$$

The first term on the RHS of Eq. 7.3 has the activation of droplets and the second

term captures the droplet removal by settling.

The rate of conversion of water vapor requires solving for supersaturation (s) and therefore requires solving for temperature (T).

$$\frac{\partial T}{\partial t} = \frac{T - T_0}{\tau_t} + \frac{L}{C_p}\frac{\dot{q_L}}{\tau_c} \tag{7.4}$$

Therefore Eqs. 7.1, 7.2, 7.3 and 7.4 is a well-constrained system of 4 equations with 4 unknowns. The flux replenishment time scale (τ_t) and activation rate ($\dot{n}_{act}$) for simplicity can be considered as the adjustable parameters. Can we identify oscillatory solutions (corresponding to second fixed point) as in Lotka-Voltera equations? Can these be observable in experiments or in LES-Microphysics model?[143]

Epilogue

Rabbi Loew found the Golem to be unruly and results to be frustrating. He disabled the unruly Golem by removing e from *emet*("Truth") to *met* (Dead). Inspired by the Rabbi, the modern-day masters should not feel any qualms in disabling the frequently unruly *Golem* and look towards the whiteboard and nature for inspiration.

References

[1] Paoli, R.; Shariff, K. *Journal of the Atmospheric Sciences* **2009**, *66*(3), 723–740.

[2] Saito, I.; Gotoh, T.; Watanabe, T. *Journal of the Meteorological Society of Japan, Ser. II* **2019**.

[3] Chandrakar, K. K.; Cantrell, W.; Krueger, S.; Shaw, R. A.; Wunsch, S. *Journal of Fluid Mechanics* **2020**, *884*.

[4] Harari, Y. N. *Sapiens: A Brief History of Humankind;* Random House, 2014.

[5] Diamond, J. M.; Ordunio, D. *Guns, Germs, and Steel;* (W. W. Norton), 1999.

[6] Giesche, A.; Staubwasser, M.; Petrie, C. A.; Hodell, D. A. *Climate of the Past* **2019**, *15*(1), 73–90.

[7] Cullen, H. M.; Demenocal, P. B.; Hemming, S.; Hemming, G.; Brown, F. H.; Guilderson, T.; Sirocko, F. *Geology* **2000**, *28*(4), 379–382.

[8] Hsiang, S. M.; Burke, M.; Miguel, E. *Science* **2013**, *341*(6151).

[9] Carleton, T. A.; Hsiang, S. M. *Science* **2016**, *353*(6304).

[10] Abel, G. J.; Brottrager, M.; Cuaresma, J. C.; Muttarak, R. *Global Environmental Change* **2019**, *54*, 239–249.

[11] Carleton, T. A. *Proceedings of the National Academy of Sciences* **2017**, *114*(33), 8746–8751.

[12] Rainmaking (ritual). Wikipedia contributors. **2021**.

[13] Megh malhar. Wikipedia contributors. **2021**.

[14] Cloud seeding. Wikipedia contributors. **2021**.

[15] Morrison, H.; van Lier-Walqui, M.; Fridlind, A. M.; Grabowski, W. W.; Harrington, J. Y.; Hoose, C.; Korolev, A.; Kumjian, M. R.; Milbrandt, J. o. t. A. S. A.; Pawlowska, H.; others. *Journal of Advances in Modeling Earth Systems* **2020**, *12*(8), e2019MS001689.

[16] Randall, D. A. *General Circulation Model Development: Past, Present, and Future;* Elsevier, 2000.

[17] Fan, J.; Wang, Y.; Rosenfeld, D.; Liu, X. *Journal of the Atmospheric Sciences* **2016**, *73*(11), 4221–4252.

[18] Bhandari, J.; China, S.; Chandrakar, K. K.; Kinney, G.; Cantrell, W.; Shaw, R. A.; Mazzoleni, L. R.; Girotto, G.; Sharma, N.; Gorkowski, K.; others. *Scientific Reports* **2019**, *9*(1), 1–12.

[19] Siebesma, A. P.; Bony, S.; Jakob, C.; Stevens, B. *Clouds and Climate: Climate Science's Greatest Challenge;* Cambridge University Press, 2020.

[20] Heintzenberg, J.; Charlson, R. J.; Brenguier, J.-L.; Haywood, J.; Nakajima, T.; Stevens, B. In *Ernst Strüngmann Forum (2008: Frankfurt, Germany)*. MIT press, 2009.

[21] Chang, K.; Bench, J.; Brege, M.; Cantrell, W.; Chandrakar, K.; Ciochetto, D.; Mazzoleni, C.; Mazzoleni, L.; Niedermeier, D.; Shaw, R. *Bulletin of the American Meteorological Society* **2016**, *97*(12), 2343–2358.

[22] Shawon, A. S. M.; Prabhakaran, P.; Kinney, G.; Shaw, R. A.; Cantrell, W. *Journal of Geophysical Research: Atmospheres* **2021**, *126*(5), e2020JD033799.

[23] Prabhakaran, P.; Shawon, A. S. M.; Kinney, G.; Thomas, S.; Cantrell, W.; Shaw, R. A. *Proceedings of the National Academy of Sciences* **2020**, *117*(29), 16831–16838.

[24] Chandrakar, K. K.; Cantrell, W.; Chang, K.; Ciochetto, D.; Niedermeier, D.; Ovchinnikov, M.; Shaw, R. A.; Yang, F. *Proceedings of the National Academy of Sciences* **2016**, *113*(50), 14243–14248.

[25] Chandrakar, K.; Cantrell, W.; Ciochetto, D.; Karki, S.; Kinney, G.; Shaw, R. *Geophysical Research Letters* **2017**, *44*(9), 4359–4367.

[26] Desai, N.; Chandrakar, K.; Kinney, G.; Cantrell, W.; Shaw, R. *Geophysical Research Letters* **2019**, *46*(15), 9154–9162.

[27] Desai, N.; Chandrakar, K.; Chang, K.; Cantrell, W.; Shaw, R. *Journal of the Atmospheric Sciences* **2018**, *75*(1), 189–201.

[28] Prabhakaran, P.; Kinney, G.; Cantrell, W.; Shaw, R. A.; Bodenschatz, E. *Geophysical Research Letters* **2020**, *47*(10), e2020GL088055.

[29] Chandrakar, K.; Cantrell, W.; Kostinski, A.; Shaw, R. *Geophysical Research Letters* **2018**, *45*(19), 10–738.

[30] Packard, C. D.; Larsen, M. L.; Cantrell, W. H.; Shaw, R. A. *Journal of Quantitative Spectroscopy and Radiative Transfer* **2019**, *236*, 106601.

[31] Packard, C. D.; Larsen, M. L.; Thomas, S.; Cantrell, W. H.; Shaw, R. A. *Atmosphere* **2020**, *11*(8), 837.

[32] Lohse, D.; Xia, K.-Q. *Annual Review of Fluid Mechanics* **2010**, *42*.

[33] Chillà, F.; Schumacher, J. *The European Physical Journal E volume* **2012**, *35*(7), 58.

[34] Deardorff, J. W.; others. *Journal of the Atmospheric Sciences* **1970**, *27*(8), 1211–1213.

[35] Niemela, J.; Skrbek, L.; Sreenivasan, K.; Donnelly, R. *Nature* **2000**, *404*(6780), 837–840.

[36] Kulmala, M.; Rannik, Ü.; Zapadinsky, E. L.; Clement, C. F. *Journal of Aerosol Science* **1997**, *28*(8), 1395–1409.

[37] Iyer, K. P.; Scheel, J. D.; Schumacher, J.; Sreenivasan, K. R. *Proceedings of the National Academy of Sciences* **2020**, *117*(14), 7594–7598.

[38] Lamb, D.; Verlinde, J. *Physics and Chemistry of Clouds;* Cambridge University Press, 2011.

[39] Yau, M. K.; Rogers, R. R. *A Short Course in Cloud Physics;* Elsevier, 1996.

[40] Chandrakar, K. K.; Saito, I.; Yang, F.; Cantrell, W.; Gotoh, T.; Shaw, R. A. *Quarterly Journal of the Royal Meteorological Society* **2020**, *146*(726), 483–504.

[41] Thomas, S.; Ovchinnikov, M.; Yang, F.; van der Voort, D.; Cantrell, W.; Krueger, S. K.; Shaw, R. A. *Journal of Advances in Modeling Earth Systems* **2019**, *11*(7), 1981–1994.

[42] Grabowski, W. W. *Journal of the Atmospheric Sciences* **2020**, *77*(3), 1151–1165.

[43] Chandrakar, K. K.; Cantrell, W.; Shaw, R. A. *Journal of the Atmospheric Sciences* **2018**, *75*(9), 3191–3209.

[44] Krueger, S. K. *Atmospheric Chemistry and Physics* **2020**, *20*(13), 7895–7909.

[45] Liu, Y.; Hallett, J. *Journal of the Atmospheric Sciences* **1998**, *55*(4), 527–536.

[46] Wyngaard, J. In *Buoyant Convection in Geophysical Flows;* Springer, 1998; pages 239–251.

[47] Chen, S.; Krueger, S. *International Cloud Modeling Workshop* **2020**.

[48] Khairoutdinov, M. F.; Randall, D. A. *Geophysical Research Letters* **2001**, *28*(18), 3617–3620.

[49] Riechelmann, T.; Noh, Y.; Raasch, S. *New Journal of Physics* **2012**, *14*(6), 065008.

[50] Bryan, G. H. *Technical Note. UCAR: Boulder, CO. http://www2. mmm. ucar. edu/people/bryan/cm1/cm1 equations. pdf (accessed 23 October 2016)* **2016**.

[51] Shima, S.-i.; Kusano, K.; Kawano, A.; Sugiyama, T.; Kawahara, S. *Quarterly Journal of the Royal Meteorological Society* **2009**, *135*(642), 1307–1320.

[52] Park, H. J.; O'Keefe, K.; Richter, D. H. *Physical Review Fluids* **2018**, *3*(3), 034307.

[53] Deardorff, J. W. *Boundary Layer Meteorology* **1980**, *18*(4), 495–527.

[54] Moeng, C.-H. *Journal of the Atmospheric Sciences* **1986**, *43*(23), 2886–2900.

[55] Kogan, Y.; Khairoutdinov, M.; Lilly, D.; Kogan, Z.; Liu, Q. *Journal of the Atmospheric Sciences* **1995**, *52*(16), 2923–2940.

[56] Stevens, B.; Cotton, W. R.; Feingold, G.; Moeng, C.-H. *Journal of the Atmospheric Sciences* **1998**, *55*(24), 3616–3638.

[57] Khairoutdinov, M.; Kogan, Y. *Monthly Weather Review* **2000**, *128*(1), 229–243.

[58] Xue, H.; Feingold, G. *Journal of the Atmospheric Sciences* **2006**, *63*(6), 1605–1622.

[59] Khairoutdinov, M. F.; Krueger, S. K.; Moeng, C.-H.; Bogenschutz, P. A.; Randall, D. A. *Journal of Advances in Modeling Earth Systems* **2009**, *1*(4).

[60] Ovchinnikov, M.; Ackerman, A. S.; Avramov, A.; Cheng, A.; Fan, J.; Fridlind, A. M.; Ghan, S.; Harrington, J.; Hoose, C.; Korolev, A.; others. *Journal of Advances in Modeling Earth Systems* **2014**, *6*(1), 223–248.

[61] Siebesma, A. P.; Bretherton, C. S.; Brown, A.; Chlond, A.; Cuxart, J.; Duynkerke, P. G.; Jiang, H.; Khairoutdinov, M.; Lewellen, D.; Moeng, C.-H.; others. *Journal of the Atmospheric Sciences* **2003**, *60*(10), 1201–1219.

[62] Khairoutdinov, M. F.; Kogan, Y. L. *Journal of the Atmospheric Sciences* **1999**, *56*(13), 2115–2131.

[63] Neggers, R.; Duynkerke, P.; Rodts, S. *Quarterly Journal of the Royal Meteorological Society* **2003**, *129*(593), 2671–2696.

[64] Stevens, B.; Moeng, C.-H.; Ackerman, A. S.; Bretherton, C. S.; Chlond, A.; de Roode, S.; Edwards, J.; Golaz, J.-C.; Jiang, H.; Khairoutdinov, M.; others. *Monthly Weather Review* **2005**, *133*(6), 1443–1462.

[65] Khain, A.; Ovtchinnikov, M.; Pinsky, M.; Pokrovsky, A.; Krugliak, H. *Atmospheric Research* **2000**, *55*(3-4), 159–224.

[66] Morrison, H.; Witte, M.; Bryan, G. H.; Harrington, J. Y.; Lebo, Z. J. *Journal of the Atmospheric Sciences* **2018**, *75*(11), 4005–4030.

[67] Wyngaard, J. *Boundary-Layer Modeling: History, Philosophy, and Sociology;* Elsevier, 1998.

[68] Götzfried, P.; Kumar, B.; Shaw, R. A.; Schumacher, J. *Journal of Fluid Mechanics* **2017**, *814*, 452–483.

[69] Kumar, B.; Götzfried, P.; Suresh, N.; Schumacher, J.; Shaw, R. A. *Journal of Advances in Modeling Earth Systems* **2018**, *10*(11), 2777–2785.

[70] Khairoutdinov, M. F.; Randall, D. A. *Journal of the Atmospheric Sciences* **2003**, *60*(4), 607–625.

[71] Smolarkiewicz, P. K.; Grabowski, W. W. *Journal of Computational Physics* **1990**, *86*(2), 355–375.

[72] McDermott, R.; Vanella, M.; Henderson, B. In *APS Meeting Abstracts*, 2017.

[73] Khain, A.; Pokrovsky, A.; Pinsky, M.; Seifert, A.; Phillips, V. *Journal of the Atmospheric Sciences* **2004**, *61*(24), 2963–2982.

[74] Fan, J.; Ovtchinnikov, M.; Comstock, J. M.; McFarlane, S. A.; Khain, A. *Journal of Geophysical Research* **2009**, *114*(D4).

[75] Monin, A.; Yaglom, A. M. *Statistical Fluid Mechanics, volume II: Mechanics of Turbulence*, Vol. 2; Courier Corporation, 2013.

[76] Andrejczuk, M.; Grabowski, W. W.; Malinowski, S. P.; Smolarkiewicz, P. K. *Journal of the Atmospheric Sciences* **2004**, *61*(14), 1726–1739.

[77] Pedersen, J. G.; Malinowski, S. P.; Grabowski, W. W. *Journal of Advances in Modeling Earth Systems* **2016**, *8*(2), 885–903.

[78] Pressel, K. G.; Mishra, S.; Schneider, T.; Kaul, C. M.; Tan, Z. *Journal of Advances in Modeling Earth Systems* **2017**, *9*(2), 1342–1365.

[79] Bohren, C. F.; Albrecht, B. A. *Atmospheric Thermodynamics;* Oxford University Press, 1998.

[80] Bertens, A.; van der Voort, D.; Bocanegra Evans, H.; van de Water, W. *Experiments in Fluids* **2015**, *56*, 89–1/9.

[81] Anderson, J. C.; Thomas, S.; Prabhakaran, P.; Shaw, R. A.; Cantrell, W. *Atmospheric Measurement Techniques Discussions* **2021**, *2021*, 1–19.

[82] Siebert, H.; Shaw, R. A. *Journal of the Atmospheric Sciences* **2017**, *74*(4), 975–988.

[83] Fedorovich, E.; Thäter, J. *Journal of Turbulence* **2001**, *2*(1), 007–007.

[84] Fedorovich, E.; Nieuwstadt, F.; Kaiser, R. *Journal of the Atmospheric Sciences* **2001**, *58*(1), 70–86.

[85] Fedorovich, E.; Nieuwstadt, F.; Kaiser, R. *Journal of the Atmospheric Sciences* **2001**, *58*(6), 546–560.

[86] Stevens, B.; Lenschow, D. H. *Bulletin of the American Meteorological Society* **2001**, *82*(2), 283–294.

[87] Yang, F.; Kollias, P.; Shaw, R. A.; Vogelmann, A. M. *Atmospheric Chemistry and Physics* **2018**, *18*(10), 7313–7328.

[88] Ovchinnikov, M.; Easter, R. C. *Journal of Geophysical Research: Atmospheres* **2010**, *115*(D14).

[89] Lebo, Z.; Seinfeld, J. *Atmospheric Chemistry and Physics* **2011**, *11*(23), 12297–12316.

[90] Grabowski, W. W.; Morrison, H.; Shima, S.-i.; Abade, G. C.; Dziekan, P.; Pawlowska, H. *Bulletin of the American Meteorological Society* **2018**, *100*(4), 655–672.

[91] Andrejczuk, M.; Reisner, J.; Henson, B.; Dubey, M.; Jeffery, C. *Journal of Geophysical Research: Atmospheres* **2008**, *113*(D19).

[92] Sölch, I.; Kärcher, B. *Quarterly Journal of the Royal Meteorological Society* **2010**, *136*(653), 2074–2093.

[93] Zhang, L.; Chong, K. L.; Xia, K.-Q. *Journal of Fluid Mechanics* **2019**, *874*, 1041–1056.

[94] Niedermeier, D.; Chang, K.; Cantrell, W.; Chandrakar, K. K.; Ciochetto, D.; Shaw, R. A. *Physical Review of Fluids* **2018**, *3*(8), 083501.

[95] Krishnamurti, R. *Journal of the Atmospheric Sciences* **1975**, *32*(7), 1353–1363.

[96] Bretherton, C. S. *Journal of the Atmospheric Sciences* **1987**, *44*(14), 1809–1827.

[97] Moeng, C.-H.; Rotunno, R. *Journal of the Atmospheric Sciences* **1990**, *47*(9), 1149–1162.

[98] Pauluis, O.; Schumacher, J. *Proceedings of the National Academy of Sciences* **2011**, *108*(31), 12623–12628.

[99] Vallis, G. K.; Parker, D. J.; Tobias, S. M. *Journal of Fluid Mechanics* **2019**, *862*, 162–199.

[100] Emanuel, K. A. *Atmospheric Convection;* Oxford University Press, 1994.

[101] Kumar, B.; Schumacher, J.; Shaw, R. A. *Theoretical and Computational Fluid Dynamics* **2013**, *27*(3), 361–376.

[102] Kostinski, A. *Environmental Research Letters* **2009**, *4*(1), 015005.

[103] Freire, L.; Chamecki, M.; Gillies, J. *Boundary-Layer Meteorology* **2016**, *160*(2), 249–267.

[104] Richter, D.; Chamecki, M. *Boundary-Layer Meteorology* **2018**, *167*(2), 235–256.

[105] Chen, J.-P.; Lamb, D. *Journal of the Atmospheric Sciences* **1994**, *51*(18), 2613–2630.

[106] Prabhakaran, P.; Weiss, S.; Krekhov, A.; Pumir, A.; Bodenschatz, E. *Physical Review Letters* **2017**, *119*(12), 128701.

[107] Zhong, J.-Q.; Funfschilling, D.; Ahlers, G. *Physical Review Letters* **2009**, *102*(12), 124501.

[108] Molemaker, M. J.; de Arellano, J. V.-G. *Journal of the Atmospheric Sciences* **1998**, *55*(4), 568–579.

[109] Helling, C. *Annual Review of Earth and Planetary Sciences* **2019**, *47*, 583–606.

[110] Yano, J.-I.; Ambaum, M. H. *Quarterly Journal of the Royal Meteorological Society* **2017**, *143*(708), 2727–2734.

[111] Riehl, H. *Geophysica* **1958**, *6*, 503–537.

[112] Yanai, M.; Esbensen, S.; Chu, J.-H. *Journal of the Atmospheric Sciences* **1973**, *30*(4), 611–627.

[113] Yamaguchi, T.; Randall, D. A. *Journal of the Atmospheric Sciences* **2012**, *69*(3), 1118–1136.

[114] Mellado, J. P. *Annual Review of Fluid Mechanics* **2017**, *49*, 145–169.

[115] Thomas, S.; Prabhakaran, P.; Cantrell, W.; Shaw, R. A. *Journal of the Atmospheric Sciences* **2021**, *DOI : 10.1175/JAS-D-20-0388.1.*

[116] Cooper, W. A. *Journal of the Atmospheric Sciences* **1989**, *46*(10), 1301–1311.

[117] Gerber, H. *Journal of the Atmospheric Sciences* **1991**, *48*(24), 2569–2588.

[118] Ditas, F.; Shaw, R.; Siebert, H.; Simmel, M.; Wehner, B.; Wiedensohler, A.; Krämer, M. *Atmospheric Chemistry & Physics* **2012**, *12*(5).

[119] Yang, F.; McGraw, R.; Luke, E. P.; Zhang, D.; Kollias, P.; Vogelmann, A. M. *Atmospheric Measurement Techniques* **2019**, *12*(11), 5817–5828.

[120] Kulmala, M.; Laaksonen, A.; Charlson, R. J.; Korhonen, P. *Nature* **1997**, *388*(6640), 336–337.

[121] Vaillancourt, P.; Yau, M.; Bartello, P.; Grabowski, W. W. *Journal of the Atmospheric Sciences* **2002**, *59*(24), 3421–3435.

[122] Abade, G. C.; Grabowski, W. W.; Pawlowska, H. *Journal of the Atmospheric Sciences* **2018**, *75*(10), 3365–3379.

[123] Sardina, G.; Poulain, S.; Brandt, L.; Caballero, R. *Journal of the Atmospheric Sciences* **2018**, *75*(2), 451–467.

[124] Li, X.-Y.; Svensson, G.; Brandenburg, A.; Haugen, N. E. *Atmospheric Chemistry and Physics* **2019**, *19*(1), 639–648.

[125] Hoffmann, F.; Yamaguchi, T.; Feingold, G. *Journal of the Atmospheric Sciences* **2019**, *76*(1), 113–133.

[126] Korolev, A. V.; Mazin, I. P. *Journal of the Atmospheric Sciences* **2003**, *60*(24), 2957–2974.

[127] Korolev, A. V.; Isaac, G. A. *Journal of the Atmospheric Sciences* **2000**, *57*(10), 1675–1685.

[128] Pinsky, M.; Khain, A. *Journal of the Atmospheric Sciences* **2018**, *75*(6), 2049–2064.

[129] Wyngaard, J. C. *Turbulence in the Atmosphere;* Cambridge University Press, 2010.

[130] Sreenivasan, K. R. *Proceedings of the National Academy of Sciences* **2019**, *116*(37), 18175–18183.

[131] Capek, T.; Borysow, J.; Mazzoleni, C.; Moraldi, M. *Remote Sensing* **2020**, *12*(24), 4129.

[132] Katzwinkel, J.; Siebert, H.; Heus, T.; Shaw, R. A. *Journal of the Atmospheric Sciences* **2014**, *71*(8), 2810–2822.

[133] Clark, T. L. *Journal of the Atmospheric Sciences* **1973**, *30*(5), 857–878.

[134] Siewert, C.; Bec, J.; Krstulovic, G. *Journal of Fluid Mechanics* **2017**, *810*, 254–280.

[135] Sommeria, G.; Deardorff, J. *Journal of the Atmospheric Sciences* **1977**, *34*(2), 344–355.

[136] Howard, L. N. In *Applied mechanics;* Springer, 1966; pages 1109–1115.

[137] Freire, L. S.; Chamecki, M. *Agricultural and Forest Meteorology* **2018**, *250*, 9–23.

[138] Schmidt, R. C.; Kerstein, A. R.; Wunsch, S.; Nilsen, V. *Journal of Computational Physics* **2003**, *186*(1), 317–355.

[139] Rasp, S.; Pritchard, M. S.; Gentine, P. *Proceedings of the National Academy of Sciences* **2018**, *115*(39), 9684–9689.

[140] Silva, S. J.; Ma, P.-L.; Hardin, J. C.; Rothenberg, D. *Geoscientific Model Development Discussions* **2020**, *2020*, 1–19.

[141] Shannon, C. E. *IRE Transactions on Information Theory* **1956**, *2*(1), 3.

[142] Hernández-Bermejo, B.; Fairén, V. *Mathematical BioSciences* **1997**, *140*(1), 1–32.

[143] Koren, I.; Feingold, G. *Proceedings of the National Academy of Sciences* **2011**, *108*(30), 12227–12232.